ANALYTICAL MECHANICS MODELING OF RESIDUAL STRESS IN METAL ADDITIVE MANUFACTURING

A Dissertation
Presented to
The Academic Faculty

by

Elham Mirkoohi

In Partial Fulfillment
of the Requirements for the Degree
Doctor of Philosophy in the
George W. Woodruff School of Mechanical Engineering

Georgia Institute of Technology
May 2020

ANALYTICAL MECHANICS MODELING OF RESIDUAL STRESS IN METAL ADDITIVE MANUFACTURING

Approved by:

Dr. Steven Y. Liang, Advisor
School of Mechanical Engineering
Georgia Institute of Technology

Dr. Christopher J. Saldana
School of Mechanical Engineering
Georgia Institute of Technology

Dr. Shreyes N. Melkote
School of Mechanical Engineering
Georgia Institute of Technology

Dr. Hamid Garmestani
School of Materials Science and Engineering
Georgia Institute of Technology

Dr. Thomas Kurfess
School of Mechanical Engineering
Georgia Institute of Technology

Date Approved: March 1, 2020

ACKNOWLEDGEMENTS

First and foremost, I would like to express my gratitude to my advisor, Professor Steven Y. Liang, for all his support, energy, guidance and encouragement throughout my Ph.D. program at Georgia Tech in the past several years. I owe a great appreciation to him for all I have learned from him on both personal and professional levels. I have learned from him how to conduct scientific research, think intuitively, supervise students, and teach.

I also would like to thank my committee members Dr. Hamid Garmestani, Dr. Shreyes Melkote, Dr. Thomas Kurfess, and Dr. Christopher Saldana for all their support, guidance, and feedback.

I need to give a special thanks to Boeing Company Research Program which in collaboration with Georgia Tech, provided the opportunity and funding necessary to carry this research.

Finally, I would like to express my deepest gratitude and appreciation to my parents whose support and encouragement was invaluable over the course of my life.

TABLE OF CONTENTS

LIST OF TABLES

LIST OF FIGURES

LIST OF SYMBOLS AND ABBREVIATIONS

AM	Additive Manufacturing
LPBF	Laser Powder Bed Fusion
PF	Powder Feed
DMD	Direct Metal Deposition
FEA	Finite Element Method
J-C Model	Johnson Cook Constitutive Model
XRD	X-ray Diffraction
C	Specific Heat
ρ	Density
T	Temperature
t	Time
V	Scan Speed
h	Enthalpy
$\nabla.$	Divergence Operator
∇	Gradient Operator
$\dot{q}$	Volumetric Heat Source
k	Thermal Conductivity
D	Thermal Diffusivity
δ	Dirac Delta Function
P	Laser Power
η	Absorptivity
R	Radial Distance from Heat Source

T_0	Initial Temperature
L_f	Latent Heat of Fusion
f	Liquid Fraction
T_s	Solidus Temperature
T_L	Liquidus Temperature
q	Heat Flux
$\varepsilon_{xx}, \varepsilon_{zz}$	Thermal Strain
E	Elastic Modulus
ν	Poisson's Ratio
α	Thermal Expansion Coefficient
G_{xh} G_{xv} G_{zh} G_{zv} G_{xzh} G_{xzv}	Elements of Green's Function
$\sigma_{xx}, \sigma_{zz}, \sigma_{xz}$	Thermal Stress
k	Material Flow Stress
A	Yield Strength
B	Strength Coefficient
C	Strain Rate Coefficient
n	Strain Hardening Coefficient
m	Thermal Softening Coefficient
T_m	Melting Temperature
ε_{eff}^{p}	Effective Plastic Strain
$\varepsilon_{xx}^{p}, \varepsilon_{yy}^{p}, \varepsilon_{zz}^{p}, \varepsilon_{xz}^{p}$	Plastic Strain
$\dot{\varepsilon}_{eff}^{p}$	Effective Strain Rate
$\dot{\varepsilon}_{xx}^{p}, \dot{\varepsilon}_{yy}^{p}, \dot{\varepsilon}_{zz}^{p}, , \dot{\varepsilon}_{xz}^{p}$	Plastic Strain Rate

F_{yield}	Yield Strength
S_{ij}	Deviatoric Stress
α_{ij}	Backstress Tensor
$\langle x \rangle$	MacCauley Bracket
$\dot{\varepsilon}_{ij}^{P}$	Plastic Strain Rate
h	Plastic Modulus
$\sigma_{xx}^{r}, \quad \sigma_{yy}^{r}, \gamma_{xz}^{r}$	Residual stress and Strain
ψ	Blending Function
G	Shear Modulus
X_{DRx}	Recrystallized Volume Fraction
Q_{act}	Activation Energy
d_0	Initial Grain
R	Gas Constant
ε_p	Peak Strain
d_{DRx}	Recrystallized Grain Size
d	Average Grain Size

SUMMARY

In the past several years, metal additive manufacturing (AM) has become a revolutionary technology to build three-dimensional complex parts via metallic powders in a layer by layer fashion. Parts built via AM have several advantages over conventional manufacturing including, lower density induced lower energy usage, elimination of multi-step manufacturing of intricated parts, no need for specific tools, reduction in material scrap rate, and many more. Aside from these advantages, there are still some limitations that impede the applicability of the AM such as steep temperature gradient, residual stress, distortion, anisotropy, and heterogeneity in microstructure and mechanical properties.

The available knowledge and technology to-date on the description and prediction of the metal AM process have been fragmented, mostly driven by phenomenological or numerical observations and primarily limited to macroscopic analysis in nature, thus restricting the full capability potential of the AM process. To breakthrough these technology bottlenecks, novel physics-based closed-form analytical thermomechanical models flanked by computational mechanics of materials are proposed to allow rapid, explicit and closed-form solutions of the AM part mechanical attributes including temperature field, thermal stress distribution, residual stress distribution induced part failure due to crack initiation and growth, and the microstructural attributes of the additively manufactured part to be derived as explicit functions of the metal powder starting properties and AM process parameters.

The thermal signature of the AM process is predicted using a transient moving heat source approach. Due to the high-temperature gradient innate in this process, material may

experience high thermal stress which often exceeds the yield strength. The thermal stress is obtained from Green's functions of stresses due to the point body load. The modified Johnson-Cook flow stress model is used to predict the yield surface. In this flow stress model, the yield strength parameter is modified to incorporate the effect of grain size using the Hall-Patch equation. The dynamic recrystallization and the resultant grain size are predicted by utilizing the Johnson–Mehl–Avrami–Kolmogorov (JMAK) model. Moreover, a grain refinement model is used to include the effect of the rapid solidification on grain size. Then, as a result of the cyclic heating and cooling and the fact that the material is yielded, the residual stress build-up is precited from incremental plasticity and kinematic hardening behavior of the metal according to the property of volume invariance in plastic deformation in coupling with the equilibrium and compatibility conditions. The predictive modeling results have been experimentally and numerically validated in encouraging agreements.

CHAPTER 1. **INTRODUCTION**

1.1 Motivation

Metal additive manufacturing (AM) is the process of building three-dimensional components in a layer by layer fashion using computer aided design (CAD) file that contains information about the appearance of the final manufactured product [1].

Based on the powder delivery system metal AM can be divided into two main categories of laser powder bed fusion (L-PBF) system and powder feed (PF) system as demonstrated in Figure 1 and Figure 2, respectively. In L-PBF, a heat source, typically a laser beam or an electron beam, is moved across the bed of metallic powder to locally and selectively melt the powder. Upon creation of the first layer, another layer is spread onto the previous layer from an adjacent reservoir to continue the process. Selective laser melting (SLM) and electron beam melting (EBM) are the examples of the L-PBF process. Powder feed methods utilize a carrier gas stream to transport powder through a nozzle directly into a melt pool (typically generated by a coaxial laser). Direct metal deposition (DMD), electron beam direct manufacturing (EBDM) are the examples of powder feed method. Both methods construct builds in a layer-by-layer fashion, but have markedly different melting and solidification dynamics which is the source of variation in mechanical and materials' attributes of the build part.

Over the last decade, metal AM has been developed rapidly to become a revolutionary technology for the production of various components for several industries such as biomedical to fabricate medical devices that are customized for an individual physiology

and are tuned to mimic biological systems such as bones, and implants. Moreover, AM is used in aerospace, automotive, and defense to fabricate parts with lower density to decrease the energy usage. Furthermore, it is used to fabricate component to be functional in harsh environment for the energy, oil and gas industries. Due to the high capability potential of AM technologies to fabricate various components with a variety of material's system, it is of great importance to be able to rapidly and accurately predict the key thermomechanical attributes of the AM parts such as temperature distribution, thermal stress distribution, and residual stress distribution without relying on time-demanding experimentations and numerical simulations.

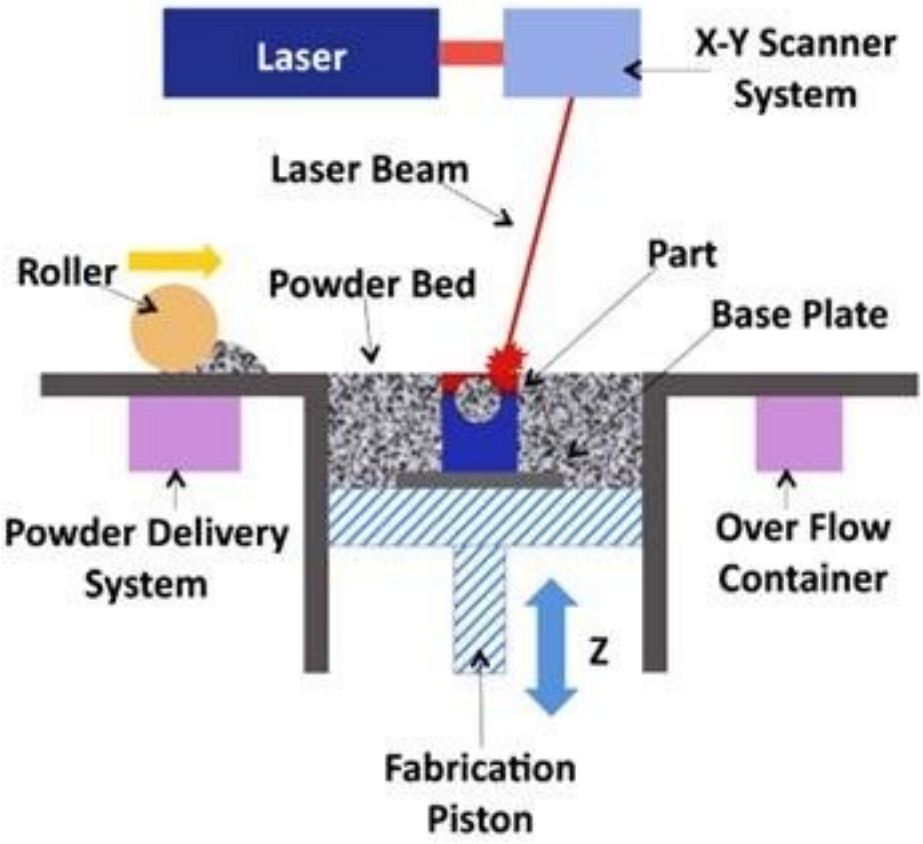

Figure 1. An illustration of laser powder bed fusion system.

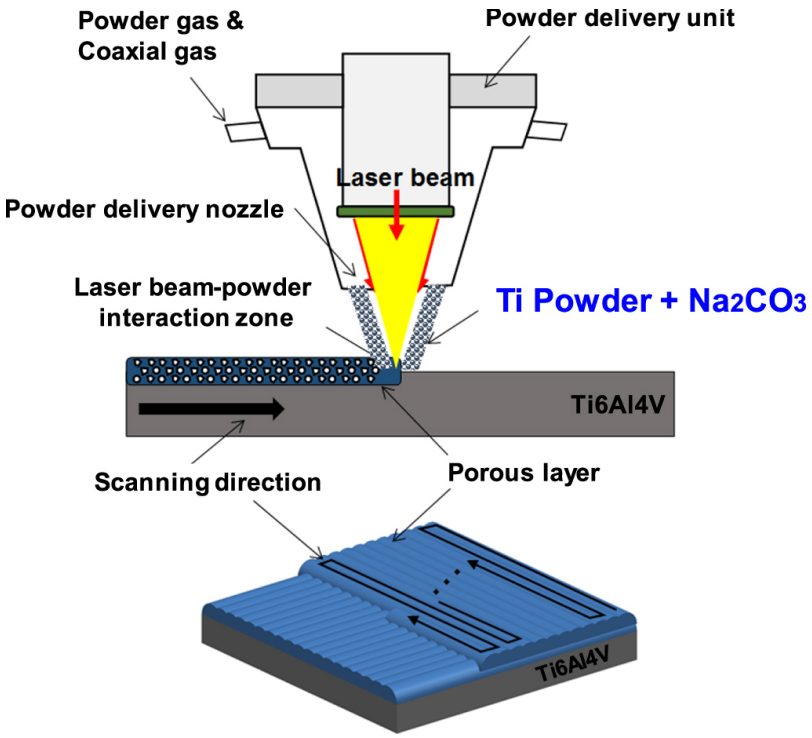

Figure 2. An illustration of powder feed system.

Additive manufacturing process has several superiorities over conventional manufacturing processes including reduction in density, fabrication of more intricate parts than has been previously possible, reduction in design and manufacturing lead time due to the single-step manufacturing, fabrication of 3D complex, nearly net shape, no need of specific tools, design flexibility, reduction in material scrap rate, and many more [2]. Use of AM parts in the industries, however, requires time-consuming flaw detection. Parts fabricated via AM processes usually suffer from high thermal stress induce delamination of layers, high tensile residual stress cause crack initiation and growth, lower fatigue life and etc., undesired distortion causes dimensional inaccuracy, and undesirable microstructure induced undesirable material properties. The main source of all the above-mentioned

concerns in an additively manufactured part is the existence of high temperature gradient and cooling rate.

Herein, a series of novel physics-based analytical models based on mechanics of material is proposed to predict the temperature field, thermal stress distribution, residual stress distribution, and grain size of the additively manufactured part to be derived as explicit function of additive manufacturing process parameters and material constitutive.

1.2 Research Goals and Objectives

The complex multi-physics aspects of the AM process occur at micro time and length scales. As a result of complex phenomena involved in this process, relying on experimentation to understand the underlying physical aspects of the AM process alone would be too time consuming, costly, and complex. Numerical models such as finite element models are used by many researchers, however, simulation of the entire process could not be achieved in a traceable amount of time. Consequently, many simplifications in modeling should be done.

So, the current roadblocks to metal AM applications are;

(1) Lack of a good prediction tool, making new process development challenging;

(2) Experimental trial-and-errors are difficult, involving lots of variables and uncertainties;

(3) Numerical simulations are time-demanding, making process optimization hard.

Analytical models, validated by physical experiments provide a means of both effectively understanding and optimizing the process by allowing for in-situ analysis as well as efficient optimization of process parameters. Thus, in this line of research, novel physics-based closed form analytical models are proposed to predict the key mechanical attributes of the AM parts including temperature field, thermal stress/strain distributions, residual stress distribution, and microstructure of the additively manufactured part.

A rather important aspect of a component performance is residual stress. Residual stress is the most challenging problem in metal additive manufacturing (AM) since the build-up of high tensile residual stress may influence the fatigue life, corrosion resistance, crack initiation, and failure of the additively manufactured components. While tensile residual stress is inherent in all the AM processes, fast and accurate prediction of stress state within the part is extremely valuable and would result in optimization of the process parameters in achieving a desired residual stress and control of the process.

The objective of this research are four folds; (1) Prediction and validation of temperature field during metal AM based on analytical description; (2) Prediction and validation of thermal stress during metal AM based on analytical description; (3) Prediction and validation of residual stress during metal AM based on analytical description; (4) Prediction and validation of microstructural evolution (grain size) during metal AM.

1.3 Research Plan

The research aims to achieve the objectives offered previously through analytical modeling of the AM process. To that aim, the process will be characterized from a physics-based

approach with a focus on temperature field, thermal stress, and residual stress modeling. A flowchart of the methodology is shown in Figure 3.

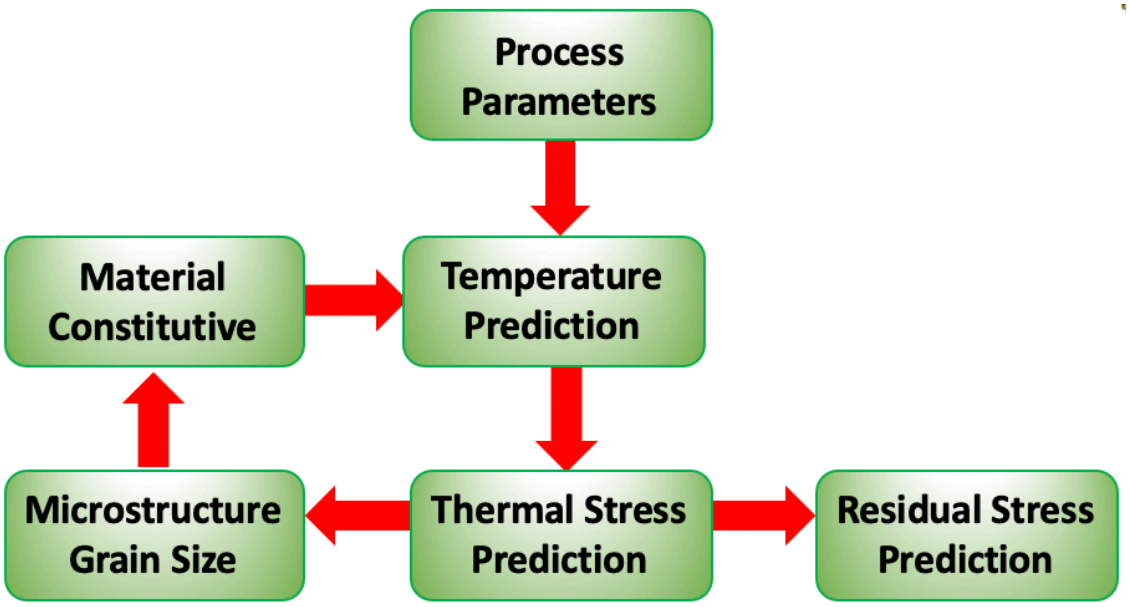

Figure 3. Block diagram of research plan.

As the flowchart shows, the AM process parameters including laser power, scan speed, scan strategy of hatching space, layer thickness, number of scans, and scan pattern, and also temperature dependent material properties are given as an input to predict the temperature field, thermal stress distribution, residual stress distribution, and grain size of the additively manufactured part. The temperature field is predicted using a moving heat source approach. The predicted temperature gradient is used as an input to predict the thermal stress distribution. The high thermal stress induced by high temperature gradient may exceed the yield strength of the material. As a result of the repeated heating and

cooling and the fact that the material is yielded the residual stress is predicted from incremental plasticity and kinematic hardening behavior of the metal in coupling with equilibrium and compatibility conditions.

The most important part of the metal AM process modeling and prediction is the prediction of the temperature field. The temperature field will be validated for various process conditions. In the prediction of temperature field, the process parameters of laser power and scan speed, temperature dependent material properties, energy needed for solid state phase change, and also the scan strategy of hatching space, layer thickness, number of scans, and scan pattern will be considered.

Non-uniform heating and high temperature gradient induce thermal stress in the additively manufactured part. The thermal stress is predicted using Greens' function of stresses due to the point body load. The thermal stress distribution will be then validated using finite element simulations.

A rather important aspect of a component performance is residual stress. The high thermal stress induced by steep temperature gradient may exceed the yield strength of the material; thus, as a result of cyclic heating and cooling and the fact that the material is yielded, the residual stress is predicted using incremental plasticity and kinematic hardening behavior of the metal in coupling with equilibrium and compatibility conditions. The residual stress will be validated for different material systems such as Ti-6Al-4V, and IN718for both powder bed fusion systems and powder feed systems via X-ray diffraction (XRD).

Moreover, in metal AM, the material will experience repetitive and rapid heating and cooling process. The grain size of build part will be obtained from nucleation and growth

rate based on recrystallized volume fraction during heating cycle and grain refinement based on transformation kinetics during rapid cooling. The grain size of the additively manufactured part has an impact on the yield strength of the material which then influences the residual stress. Lat but not least, the effect of dynamic recrystallization on residual stress will be discussed.

The goal of this work is to establish a predictive model for metal additive manufacturing induced residual stress. The proposed coupled thermomechanical analytical model is much faster than finite element methods (FEM) by more than 100 times; as it involves no iteration, nor meshing. It is also more accurate than FEM's; since it relies on materials mechanics, but not numeric. Moreover, it offers microstructure affected manufacturing which FEM does not deliver. Last, it is able to reverse calculate the process parameters and properties for process planning, which FEM cannot deliver.

1.4 Overview of Thesis

The dissertation is arranged to discuss the step by step prediction of residual stress. In the following chapter, a review of the present and past literature on metal additive manufacturing process induced residual stress will be provided. The literature review will provide insight into the research questions that the dissertation seeks to answer.

The following chapter after literature review will discuss the analytical models proposed to predict the temperature field, thermal stress distribution, residual stress distribution, and grain size of the additively manufactured part.

Then the discussion and validation of each model will be provided to encouraging the agreement. At the end, the conclusion and recommendation will finalize the dissertation.

CHAPTER 2. LITERATURE REVIEW

This chapter focuses on previous research efforts on modelling of temperature profile, thermal stress and residual stress using experimental findings, finite element modelling, analytical modelling, and various combinations of those efforts.

2.1 Literature Review on Metal Additive Manufacturing Induced Temperature Field

The most important part of the metal AM process modeling and prediction is the prediction of the temperature induced by laser since the non-uniform temperature will cause the thermal stress to appear in the structure. As a result of thermal stress in the build material, the tensile residual stress on the surface accelerates the crack propagation and growth [3, 4]. Significant research has been carried out to predict the temperature profile during metal additive manufacturing process. Fergani *et al.* introduced an analytical model to predict the temperature in the direct metal deposition process. They predicted the temperature using a moving point heat source analysis. In this work, the effect of material temperature sensitivity is ignored [5]. Yap *et al.* proposed an analytical model to predict the energy input required to process different metallic materials for selective laser melting (SLM) process. The model held many assumptions, such as a semi-circular cross-section for melt tracks, temperature-independent specific heat, no heat loss to the surroundings and absorptance of material to laser irradiation based on bulk material properties. The melting, solidification, and solid-state phase change is also not considered in their model. The simplified model is able to predict the required energy input within an order of magnitude and provide researchers with a useful model to estimate the optimal SLM parameters [6].

Prediction of the temperature precisely in metal AM is the pillar for predicting the thermal stress, residual stress, and part distortion. The non-uniform heating during AM processes may lead to the thermal stress. The large thermal gradient and cooling rate during the metal AM processes can generate complex microstructures in the build material [7]. Kelly *et al.* predicted the temperature in the AM processes in order to predict the microstructure evolution in the build part. In their work, the melting/solidification phase change is not considered [8]. Hoadley and Rappaz introduced a 2D quasi-stationary model to predict the temperature in the laser cladding process. Their research focused on the influence of the laser speed and power on the layer thickness [9]. Toyserkani *et al.* developed a 3D model to solve the heat problem using a coupled multi-physics system. They have used thermal analysis in order to predict the melt pool shape [10]. Cao and Ayalew developed a control-oriented multiple input multiple output modeling of the laser-aided powder deposition processes. The objective of their work is to control the height and the temperature of a layer. Their investigation described the essential role of temperature modeling to control the quality of the final part [11]. Hitzler *et al.* investigated the influence of scan strategy on material characteristics, such as strength, hardness, and young's modulus by modeling the temperature field [12, 13]. Rashid *et al.* worked on the effect of scan strategy on density and metallurgical properties of a build part during the selective laser melting (SLM) process. Their results showed that parts which are made using a single scan have higher levels of hardness than parts that are made by scanning each layer twice [14].

Roberts *et.al* employed the finite element analysis to model the three-dimensional temperature field during laser melting of metallic powders in additive layer manufacturing. They have considered heat loss from the surface due to convection and radiation. Although,

they have also considered the temperature dependent material properties, they have not considered the layering aspect of metal AM [15]. Qi *et al* developed a self-consistent three-dimensional model for a coaxial laser powder cladding process. The heat transfer, phase change, and fluid flow in the molten pool are simulated with a control volume finite difference method. They concluded that the numerical model predicts higher melt pool size (about 22%) compared to experimental values [16]. Lee *et al.* conducted a numerical transport simulation to simulate multilayer single-track laser additive manufacturing deposition of IN718. The simulation accurately predicted melt pool peak temperature and deposit geometry. The peak temperature prediction error is less than 2.5% and build geometry prediction error is less than 12% in both height and width [17]. Kumar *et al.* developed a finite element model to investigate the influence of scan strategy on melt pool size [18]. Manvatkar *et al.* developed a three-dimensional heat transfer and material flow model to numerically simulate the temperature and velocity fields during additive manufacturing of SS316 [19]. Cheng *et al.* developed a transient thermal analysis to predict the melt pool size, numerically. They have concluded that for a given power, as the scanning speed increases, the melt pool depth decreases [20]. Pinkerton *et al.* proposed a numerical model in order to predict the melt pool geometry. The model considers the pool boundaries orthogonal to the direction of motion as arcs of a circle reflecting the dominance of surface tension forces and accounts for elongation of the pool with increasing traverse speed [21]. Mukherji *et al.* [22] used FEM to predict the temperature in laser-assisted AM. They used a three-dimensional transient heat transfer and fluid flow to calculate the temperature field. They have concluded that prediction of temperature field in AM has a substantial influence on residual stress and distortion prediction. Cheng *et al.* [23]

developed a 3D thermal model using FEM to predict the temperature in electron beam additive manufacturing (EBAM) processing. The predicted melt pool geometry is compared to experimental results. The average error obtained between the predicted melt pool and experimental values is around 32%. Michaleris [24] used a quiet element method and an inactive element method to predict the temperature profile in metal AM. They have concluded that the inactive element method reduces the number of degrees of freedom at the initial stage, but it substantially decreases the computational efficiency compared to the quiet element method.

Mirkoohi *et al.* [25] proposed a two-dimensional analytical model to predict the surface temperature and melt pool geometry by considering the effects of temperature-dependent material properties, liquid/solidification phase change, and also the effect of layer addition. In another work, they have introduced five different heat source models to predict the temperature field. They have investigated the limitations and advantages of each heat source model under different process conditions [26, 27]. Ribeiro *et al.* used an analytical model to predict the temperature field for a moving heat source. In this model, the boundary conditions are considered.

Carcel *et. al* predicted the temperature in metal AM experimentally. A pyrometer is used to predict the temperature. They have concluded that the cooling rate decreases with the number of layers, the cooling rate is significantly faster as the interval time between layers increases, and the maximum temperature increases for subsequent layers [28]. Cheng *et.al* used thermal imaging technology to capture the transient thermal response in the SLM process. Using an infrared (IR) camera they have measured the melt pool size for different process conditions [29].

Due to the complexity of the additive manufacturing processes of powder bed and powder feed systems, not only is it time-consuming to do the experiments in order to capture the physical aspects of the metal AM processes, but also it is expensive. In the past few decades, the numerical simulations appear to be the only effective way to achieve an understanding of metal additive manufacturing processes [30, 31]. However, the numerical methods have low computational efficiency and cannot capture all the physical aspects of the metal AM processes. On the other hand, physics-based analytical models provide a means of both effectively understanding and optimizing the process parameters due to the high computational efficiency. The analytical solutions have the potential to predict the key AM attributes in ways significantly faster than finite element method (FEM) simulations, by two or more orders of magnitudes [32]. Efficient and accurate predictions are therefore enabled, and the optimization of metal additive manufacturing processes which would be too complicated to cope with by the majority of other studies, that have resorted to empirical and FEM attempts. It also reduces, if not completely eliminates, the need for a costly and lengthy trial and error developmental curve for new material and components [33]. A complete build analysis with high accuracy becomes computationally tractable using the analytical model.

2.2 Literature Review on Metal Additive Manufacturing Induced Thermal Stress

Due to the repeated heating and cooling, localized heating, and relatively low thermal conduction in metal AM processes, material experience steep temperature gradient. The resulting thermal expansion and contraction mismatch induced by steep temperature

gradient and cyclic heating and cooling cause the stresses to appear in the build part. As a result of the existence of the thermal stress, the residual stress, part distortion, crack initiation and growth due to the tensile residual stress could diminish the final part performance [34, 35]. The final performance of the build part highly depends on the process parameters such as laser power, scan speed, layer thickness, and hatching space [36]. Consequently, having a model to accurately and rapidly predicts the stress state within the part is highly valuable since it enables the control and optimization of the AM process parameters in achieving the desired part performance.

Although there are significant works on literature studying various aspects of AM such as residual stress, fatigue, and microstructure evolution, there is limited attention on thermal stress prediction which is the source of all the above-mentioned problems. Dain *et al.* investigated the elastic thermal stress in the two thin elastic plates in the form of infinite half-planes that are joined together using FEM. They have concluded that the welding procedure has a substantial influence on the formation of thermal stresses [37]. Shibib investigated the thermal stress in final-length end-pumped laser rods using numerical analysis. They have investigated the effect of length of the rod and radius of the rod on thermal stress [38]. Yilbas *et al.* investigated the thermal stress in the laser heating of the sheet metal numerically. They concluded that the scan speed has a substantial influence on the temperature distribution and thermal stress [39].

2.3 Literature Review on Metal Additive Manufacturing Induced Residual Stress

Different types of research have been done to predict the built-up of residual stress in an additively manufactured part [40]. The research in this domain can be classified into three main categories including experimentation, numerical modeling, analytical modeling, and combination of these methods.

Experimental procedures to measure the residual stress in the components could be categorized into destructive and non-destructive methods. The non-destructive methods can be classified into X-ray diffraction- which is cable of near surface residual stress measurements- and neutron diffraction- which is capable of volumetric residual stress measurements. Other non-destructive methods include ultra-sonics as explained by Noronha and Wert [41], electrical resistivity as explained by Chung [42] magnetic behavior as explained by Krause et al. [43] and piezo-spectroscopy in thin films as explained by Ager III and Drory [44]; these are material and geometry specific. Destructive methods such as hole drilling, sectioning, crack compliance, digital image correlation, and electronic speckle pattern interferometry (ESPI) essentially create a free surface in the part and correlate resultant deformation to residual stress as stated by Prime [45]. Strantza *et al.* measured the residual strains within the Ti-6Al-4V parts built via laser powder bed fusion (L-PBF) process. They have used X-ray diffraction to determine the strain pattern within the built part [46]. Wu *et al.* [47] measured the residual stress using the digital image correlation in conjunction with build plate removal and sectioning. The results are compared to the nondestructive volumetric neutron diffraction technique. They have concluded that the residual stress is reduced by decreasing the island size, increasing the applied energy per length, and increasing island to wall rotation to 45 degrees. Staub *et al*. [48] measured the residual stress using the X-ray technique in the L-PBF of SS316L. They

have concluded that the higher aspect ratio (width/depth) of the melt pool geometry could result in higher residual stress. Wang *et al.* [49] used X-ray method to measure the residual stress from electron beam additive manufacturing (EBAM) process as well as the selective laser melting (SLM) for Ti-6Al-4V and IN718 parts. They have summarized that the residual stress of Ti-6Al-4V parts that are made using EBAM is more compressive compared to that made with IN-718. Also, the residual stress in Ti-6Al-4V parts have a lower absolute value compared to that in IN718 parts.

Numerical modeling is used by many researchers to predict the residual stress build-up during the AM process. Zhao *et al.* developed a numerical model to simulated heat transfer and residual stress distribution in direct metal laser sintering. They indicated that based on the simulations, the melting and solidification happens at about 1ms. Moreover, the obtained horizontal normal residual stresses are the dominant stress component compared to vertical normal stress and shear stress [50]. Hajializade *et al.* proposed a thermomechanical numerical model to predict the residual stress in the additively manufactured part using coarsening approach [51]. Zekovic *et al.* developed a thermo-mechanical finite element model to predict the residual stress in the straight wall as well as a cylindrical wall. The results postulate that the residual stress in the cylindrical wall is more uniformly distributed and has a lower magnitude compared to straight wall [52]. Aggarangsi and Beuth [4] used a finite element method (FEM) to simulate the residual stress. In their modeling, they defined a temperature gradient from the melt pool and correlated it to the maximum residual stress. They have shown that localized preheating could reduce the maximum residual stress in the additively manufactured 304 stainless steel. Panda and Sahoo [53] used FEM to predict the residual stress in the direct metal

deposition (DMD) of AlSi10Mg. They have predicted temperature distribution using transient temperature and coupled the results to a structural model to predict the residual stress. In their modeling, the thermal and mechanical material properties are considered constant. Also, the effects of scan strategies are not considered in this modeling. Chen *et al.* [54] used FEM to simulate the residual stress in additively manufactured parts using inherent strain method. They have utilized the temperature results obtained from thermocouples to calibrate the process parameters. Then, they have used Goldak's heat source model to obtain the thermal gradients and the inherent strains. Ganeriwala *et al*. [40] also used FEM to simulate the stress state in laser powder bed fusion of Ti-6Al-4V. They have used lumping approach to speed up the computations. They indicated that the stress is higher near the boundaries for the island scan strategies. Ding and Shin [55] proposed a 3D thermo-elastoplastic finite element model to simulated the residual stress. They have validated the results using neutron diffraction strain scanner. Ahmad *et al.* [56] predicted the residual stress in the SLM of Ti-6Al-4V and IN718 using inherent-strain-based method. They have used contour method to experimentally validate the numerical model. They have concluded that in both material systems the residual stress is highly tensile near the surface and along the edges, and compressive at the center region of the samples. They also concluded that the high tensile residual stress is observed along the build direction. Li *et al.* [57] gave an overview of residual stress in metal AM. They expressed that the residual stress formation in metal AM is mostly caused by steep temperature gradient and high cooling rate. They also indicated that the magnitude and behavior of the residual stress could be mitigated through in-process methods such as preheating, process planning, and feedback control and post-process methods such as machining and heat treatment. Fergani

et al. [58] presented a model for the prediction of stress. In their modeling, properties are considered constant. Also, the effect of scan strategy is not considered in their modeling. Moreover, the stress in the build direction is considered to be elastic.

Although experimental measurements of stresses within the part play a crucial role in the understanding of this phenomenon, experimental measurement of the entire part is challenging and expensive. Finite element modeling (FEM) is also used by many researchers [59]; however, the simulation of the entire process could not be achieved in a traceable amount of time. Consequently, many simplifications in modeling should be undertaken. Moreover, the inverse analysis to optimize the process parameters to achieve the desired part performance cannot be achieved via FEM in a reasonable amount of time [35, 60, 61]. In contrast, analytical models validated by physical experiments provide a means to effectively understand, control and optimize the process parameters by allowing for in-situ analysis.

CHAPTER 3. MODELING OF RESIDUAL STRESS IN METAL ADDITIVE MANUFACTURING

This chapter describes in detail the residual stress model for metal additive manufacturing process. First, the temperature field is predicted using a moving heat source approach. Different heat source models based on heat source geometry are explained. Second, the modelling of thermal stress is presented. Third, the modelling of residual stress is presented. Forth, the modelling of the microstructure evolution of grain size is presented. Last, modelling of microstructure affected residual stress formation is explained.

3.1 Temperature Field Modeling

The most important part of the metal AM process modeling and prediction is the prediction of the temperature field induced by a laser since the non-uniform temperature field causes the thermal stress to appear in the structure. As a result of thermal stress in the build material, the tensile residual stress on the surface accelerates the crack propagation and growth [3, 4].

The complex three-dimensional parts can be manufactured using AM process by locally melting the desired portion of the powders, layer by layer [62].The necessary heat for melting the powders is provided by a laser. The laser-matter interaction is a crucial part in the modeling of the AM process. Various heat source modeling approaches exist in the literature to simulate the temperature field during AM process. Each of models has its own limitations, such as ignoring the temperature sensitivity thermal material properties, ignoring the multi-layer aspect of metal AM, ignoring the solid-state phase change, and so

forth. In this work, four different analytical heat source modeling approaches are introduced including steady state and transient moving point heat source approach, transient semi-elliptical moving point heat source approach, transient double elliptical moving heat source approach, and transient uniform moving heat source approach. The explanation of the mathematical formulation is explained in sections 3.1.1 through 3.1.4.

The temperature field is predicted using both steady-state moving heat source approach and transient moving heat source approach in a semi-infinite medium. As shown in Figure 4, the laser moves along the scan direction (x-axis) and deposits its energy to melt the metallic powders. The heat loss due to convection and radiation is not considered in this modeling.

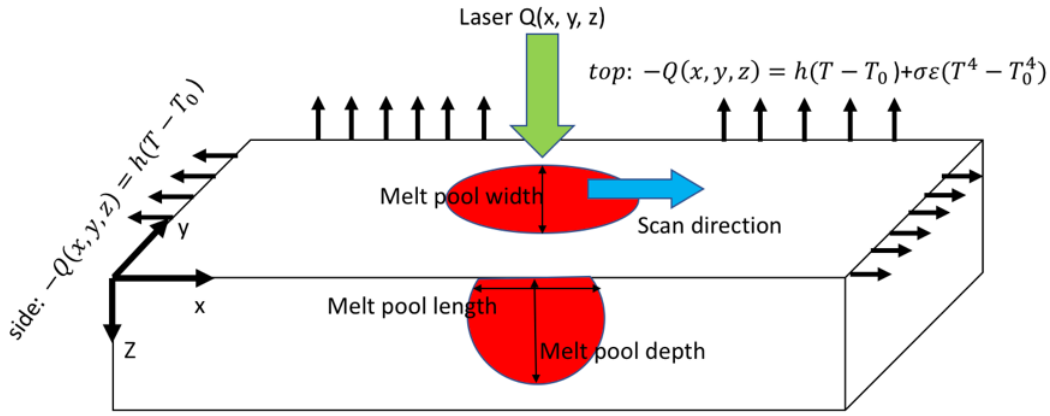

Figure 4. Illustration of the heat transfer model in laser bed metal additive manufacturing process.

Heat conduction in a homogeneous solid is governed by the linear partial differential equation

$$\frac{\partial u\rho}{\partial t} + \frac{\partial \rho hV}{\partial x} = \nabla.(k\nabla T) + \dot{q} \tag{3.1}$$

where u represents the internal energy, h is the enthalpy, ρ is the density, k is the conductivity, $\dot{q}$ is a volumetric heat source, T is the temperature and V is the speed of either the heat source or the medium.

The x direction corresponds to the constant speed of a moving heat source. Also, y is directed inside the processed material, and z, the direction perpendicular to x in the plane of the processed material surface. The first term in Equation (3.1) on the left-hand side represents the change of internal energy and the second is a convective term. On the right-hand side, there is the conductive term and a heat source or sink. For $V = 0$, this equation becomes the heat conduction equation, given that $du = C\,dT$, with C being the heat capacity

$$C\frac{\partial \rho T}{\partial t} + \frac{\partial \rho hV}{\partial x} = \nabla.(k\nabla T) + \dot{q} \tag{3.2}$$

The steady state equation with constant velocity V, can be simplified using the continuity equation

$$C\frac{\partial \rho}{\partial t} + \frac{\partial \rho V}{\partial x} = 0 \tag{3.3}$$

Resulting in

$$\rho C(T)V\frac{\partial T}{\partial x}+\frac{\partial \rho hV}{\partial x}=\nabla.(k(T)\nabla T)+\dot{q} \tag{3.4}$$

given that $du = dh = CdT$.

The convection-diffusion equation becomes the differential equation of heat conduction which can be expressed as

$$\frac{\partial^2 T}{\partial x^2}+\frac{\partial^2 T}{\partial y^2}+\frac{\partial^2 T}{\partial z^2}+\frac{1}{k}Q(x,y,z,t)=\frac{1}{D}\frac{\partial T}{\partial t} \tag{3.5}$$

where T $\equiv T(x,y,z,t)$. k is thermal conductivity, and D is the thermal diffusivity. The heat source Q is related to the equivalent volumetric source $Q(x,y,z,t)$ ($\mathrm{W/m^3}$) by the delta function notation as

$$Q(x,y,z,t)=\ Q\ \delta(x-Vt)\delta(y-y_0)\delta(z-z_0) \tag{3.6}$$

where δ denotes the Dirac delta function.

In order to consider the moving heat source, it is assumed that the coordinate system transfers from the x, y, z fixed coordinate system to ζ, y, z coordinate moving by using the transformation

$$\zeta = x - Vt \tag{3.7}$$

Using the abovementioned transformation, the heat conduction equation for the moving coordinate system can be written as

$$\frac{\partial^2 T}{\partial \zeta^2} + \frac{\partial^2 T}{\partial y^2} + \frac{\partial^2 T}{\partial z^2} + \frac{1}{k} Q\delta(\zeta)\delta(y)\delta(z) = \frac{1}{D}\left(\frac{\partial T}{\partial t} - V\frac{\partial T}{\partial \zeta}\right) \tag{3.8}$$

3.1.1 Moving Point Heat Source Approach

Equation (3.8) can be solved by the assumption of the quasi-stationary condition by setting $\frac{\partial T}{\partial t} = 0$ [63]. Using the separation of variables, the closed form solution of the temperature field can be obtained as

$$T_{steady} = \frac{P\eta}{4\pi kR} \exp \frac{-V(R-x)}{2D} + T_0 \tag{3. 9}$$

where P is the laser power, η represents the absorption coefficient, k is thermal conductivity and assumed to be temperature dependent, V is scan speed. T_0 is the initial temperature.

R is the radial distance from the heat source which can be calculated as

$$\mathrm{R}=\sqrt{x^2+y^2+z^2} \tag{3.10}$$

D is thermal diffusivity and can be obtained from

$$D(T)=\frac{k(T)}{\rho C_p^m(T)} \tag{3.11}$$

where ρ is material density and $C_p^m(T)$ is the modified heat capacity. The melting/solidification phase transformation take place during AM process, and it has a profound effect on melt pool geometry. This is considered using modified heat capacity.

$$C_p^m = C_p(T)+L_f\frac{\partial f}{\partial T_n} \tag{3.12}$$

In which $C_p(T)$ is temperature dependent specific heat, L_f is latent heat of fusion, and f is liquid fraction which can be calculated from

$$f=\begin{cases}0, & T<T_s\\ \frac{T-T_s}{T_L-T_s}, & T_s<T<T_L\\ 1, & T>T_L\end{cases} \tag{3.13}$$

where, T_s is solidus temperature and T_L is liquidus temperature.

The transient point heat source solution is developed by Carslaw and Jaeger [64] using the differential equation of heat conduction (Equation 3.8) as the following

$$T_{total} = \frac{P\eta}{8\rho C_p^m (\pi D t)^{3/2}} \int_0^t \frac{exp\left(-\frac{\left((x-x') - V(t-t')\right)^2 + (y-y')^2 + (z-z')^2}{4D(t-t')}\right)}{(t-t')^{3/2}} dt' + T_0 \quad (3.14)$$

Equation (3.14) gives the temperature field at position *(x,y,z)* at time *t* due to an instantaneous unit heat source applied at position (x', y', z') at time t'.

where P is the laser power, η represents the absorption coefficient, ρ is density, C_p^m is the modified heat capacity to account for solid state phase change as explained in Equation (3.12) and (3.13). V is scan speed, D is thermal diffusivity, and T_0 is the initial temperature.

It should be noted that the medium is segmented into small regions to calculate the temperature. Thus, the total temperature (T_{total}) is the summation of calculated temperature in each segment which approaches the steady state solution.

Total temperature in a closed form solution can be obtained as

$$T_{total} = \frac{P\eta}{8\rho C_p^m (\pi D t)^{3/2}} \times \frac{N \times exp\left(-\frac{\left((x-x') - V(t-t')\right)^2 + (y-y')^2 + (z-z')^2}{4D(t-t')}\right)}{(t-t')^{3/2}} \Delta t' + T_0 \quad (3.15)$$

where N is the number of segments.

3.1.2 Semi-Elliptical Moving Heat Source Approach

Three-dimensional (3D) semi-ellipsoidal heat transfer model is used to predict the temperature field and melt pool geometry in metal AM processes. The proposed model can be used to predict the temperature in laser-based metal additive manufacturing configurations of either direct metal deposition or selective laser melting.

The 3D ellipsoidal heat source model is introduced by Goldak et al. [65] where the heat flux can be calculated as

$$q(x,y,z) = \frac{6\sqrt{3}\,\eta P}{abc\pi\sqrt{\pi}} exp\left(-\frac{3x^2}{c^2} - \frac{3y^2}{a^2} - \frac{3z^2}{b^2}\right) \quad (3.16)$$

where P is the laser power,η is laser absorptivity, a, b, and c are the heat source geometry parameters, as shown in Figure 5.

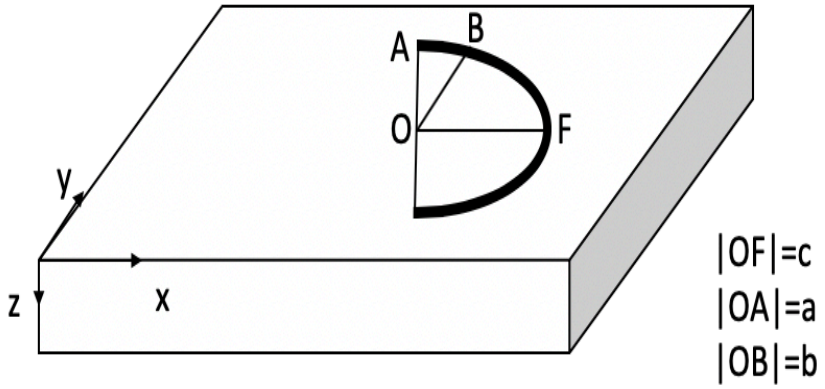

Figure 5. Illustration of the semi-elliptical heat source geometry.

The solution of temperature for ellipsoidal moving heat source from t'=0 to t for a semi-infinite body in a dimensionless form is given as *[66]*

$$\frac{\theta}{n} = \frac{1}{\sqrt{2\pi}} \int_0^{\frac{v^2 t}{2k}} \frac{d\tau}{\sqrt{\tau + u_a^2}\sqrt{\tau + u_b^2}} \left(\frac{A_1}{\sqrt{\tau + u_c^2}}\right) \tag{3.17}$$

where

$$A_1 = exp\left(-\frac{(\xi + \tau)^2}{2(\tau + u_c^2)} - \frac{\psi^2}{2(\tau + u_a^2)} - \frac{\lambda^2}{2(\tau + u_b^2)}\right) \tag{3.18}$$

The dimensionless parameters are defined as

$$\xi = \frac{Vx}{2D}, \psi = \frac{Vy}{2D}, \lambda = \frac{Vz}{2D}$$

(3.19)

where V is scan speed, and D is thermal diffusivity which can be obtained from Equation (3.11).

$$\tau = \frac{V^2(t - t')}{2D}$$

(3.20)

$$u_a = Va2\sqrt{6}\,D,\ u_b = Vb2\sqrt{6}\,D,\ u_c = Vc2\sqrt{6}\,D$$

(3.21)

$$n = \frac{P\eta V}{4\pi D^2 \rho C(T_m - T_0)}$$

(3.22)

$$T_{total} = \frac{P\eta V}{4\pi D^2 \rho C} \times \frac{1}{\sqrt{2\pi}} \int_0^{\frac{V^2 t}{2k}} \frac{d\tau}{\sqrt{\tau + u_a^2}\sqrt{\tau + u_b^2}} \left(\frac{A_1}{\sqrt{\tau + u_c^2}}\right) + T_0$$

(3.23)

3.1.3 Double Elliptical Moving Heat Source Approach

The 3D double ellipsoidal heat source model is developed by Goldak et al. [65] as following

$$q(x,y,z,t) = \frac{6P\eta\sqrt{3}}{\pi\sqrt{\pi}\,ab} \begin{Bmatrix} \frac{f_f}{c_f} exp - 3\frac{(x-Vt)^2}{{c_f}^2} - 3\frac{y^2}{a^2} - 3\frac{z^2}{b^2} & for\ x > Vt \\ \frac{f_r}{c_r} exp - 3\frac{(x-Vt)^2}{{c_r}^2} - 3\frac{y^2}{a^2} - 3\frac{z^2}{b^2} & for\ x < Vt \end{Bmatrix} \tag{3.24}$$

where P is laser power energy, η is laser absorptivity, V is the scan speed, and $a, b, c_r,$ and c_f are the respective radii of the sides, rear and front of the ellipsoid as shown in Figure 6.

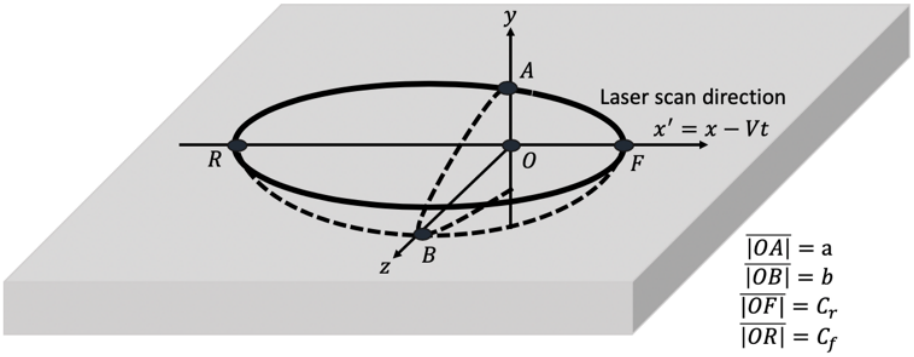

Figure 6. Illustration of the double elliptical heat source geometry.

f_r and f_f are the portion of the heat deposited, respectively, in the front and rear ellipsoid (with $f_r + f_f = 2$). In order to fit the results to experimental data, calibration of the double-

ellipsoidal heat source model requires adjustment of six parameters including η, a, b, c_r, c_f, and f_r. Some researchers tried to reduce this number by applying a constraint to the model as [66-68]

$$\frac{f_f}{c_f} = \frac{f_r}{c_r} \tag{3.25}$$

This constraint guarantees the continuity of the function q across the $x = Vt$ plane at any time, t, to yield

$$f_f = \frac{\alpha c_f}{c_f + c_r} \tag{3.26}$$

$\alpha = 3$ correlates to the choice of $f_f = 0.6$ as suggested by Goldak et al. [65], should be used as a default value when enough experimental data are not available. It should be noted that the temperature field induced by double double-ellipsoidal heat source, q, is always continuous. In other words, it is independent of the value of α.

Green function approach is used to solve the differential equation of heat conduction using Equation (3.8), to derive the temperature field for the case of double elliptical heat source as

$$T_{total}(x,y,z,t)$$

$$= T_0$$

$$+ \frac{3P\eta\sqrt{3}}{\pi\sqrt{\pi}\,\rho C} \times \int_0^t \frac{\exp\left[-3\dfrac{y^2}{12D(t-t')+a^2} - 3\dfrac{z^2}{12D(t-t')+b^2}\right]}{\sqrt{12D(t-t')+a^2} \times \sqrt{12D(t-t')+b^2}}$$

$$\times \left[f_r A_r (1-B_r) + f_f A_f \left(1+B_f\right)\right] dt'$$

(3.27)

where

$$A_i = A(x,t,t';c_i) = \frac{\exp\left[-3\dfrac{(x-Vt)^2}{12D(t-t')+{c_i}^2}\right]}{\sqrt{12D(t-t')+{c_i}^2}}$$

(3.28)

$$B_i = B(x,t,t';c_i) = erf\frac{c_i(x-Vt)}{2\sqrt{12D(t-t')+{c_i}^2}\sqrt{D(t-t')}}$$

(3.29)

Equation gives the temperature field at position (x,y,z) at time t due to an instantaneous unit heat source applied at position (x', y', z') at time t'. The index i denotes front, f, or rear, r.

3.1.4 Uniform Moving Heat Source Approach

The heat flux $q(x,y,z)$ at any point (x,y,z) for a uniform heat source is given as [64]

$$q(x,y,z) = \frac{P\eta}{4\,abc}\begin{Bmatrix} -a < x < a \\ -b < y < b \\ 0 < z < c \end{Bmatrix}$$

(3.30)

where P is the laser power,η is laser absorptivity, a, b, and c are the heat source geometry parameters.

As for the other types of the heat sources, the solution of the temperature field is based on an instantaneous point source in a fixed coordinate

$$T_{total} = T_0 - \frac{P\eta}{2^5\rho C\ abc}\int_0^t Erfh(x + V(t-t'), a, t') \times Erfh(y, b, t') \times Erfh(z, c, t')dt'$$

(3.31)

with Fo_s the Fourier number based on s and $t - t'$ as length and time respectively,

$$Erfh(x, s, t') \triangleq Erf\left(\frac{x-s}{\sqrt{4D(t-t')}}\right) - Erf\left(\frac{x+s}{\sqrt{4D(t-t')}}\right)$$

$$= Erf(\frac{\sqrt{Fo_s}}{2}\left(\frac{x}{s} - 1\right) - Erf(\frac{\sqrt{Fo_s}}{2}(\frac{x}{s} + 1)) \triangleq Erf(\frac{x}{s}, Fo_s)$$

(3.32)

The closed-form solution of temperature can be obtained by solving the three-dimensional equation of heat conduction for a steady state condition which is shown in equation (3.9).

3.2 Thermal Stress Modeling

Non-uniform heating induced by fast irradiation of the laser and low conduction, re-melting and re-solidification, and different thermal expansion coefficient induced by steep temperature gradient throughout the part are the main sources of thermal stress.

Considering the plain strain condition ($\varepsilon_{yy} = 0$), the normal strain along the scan direction can be obtained as;

$$\varepsilon_{xx} = \frac{1}{E(T)}(1 - \nu(T)^2)\sigma_{xx} + \alpha T(1 + \nu(T)) \tag{3.33}$$

where the elastic modulus E(T), Poisson's ratio $\nu(T)$, and coefficient of thermal expansion $\alpha(T)$ are temperature dependent. σ_{xx} is the normal stress along the scan direction. The acquired temperature field could then be used to calculate the thermal stress by combining the stress components including; (1) stresses due to body forces $F_x = -\frac{\alpha(T)E(T)}{1-2\nu(T)}\frac{\partial T}{\partial x}$, $F_z = -\frac{\alpha(T)E(T)}{1-2\nu(T)}\frac{\partial T}{\partial z}$ along the scan direction and build direction which can be obtained from;

$$\{\sigma\} = \int_0^\infty \int_{-\infty}^\infty (G(x, z, x', z')\, B\, dx' dz' \tag{3.34}$$

$$\text{Where } \{\sigma\} = \{\sigma_{xx}\, \sigma_{zz}\, \sigma_{xz}\}^T \tag{3.35}$$

$$G = \begin{pmatrix} G_{xh} & G_{xv} \\ G_{zh} & G_{zv} \\ G_{xzh} & G_{xzv} \end{pmatrix} \tag{3.36}$$

$$B = \begin{Bmatrix} -\frac{\alpha(T)E(T)}{1-2\nu(T)}\frac{\partial T}{\partial x} \\ -\frac{\alpha(T)E(T)}{1-2\nu(T)}\frac{\partial T}{\partial z} \end{Bmatrix} \tag{3.37}$$

As described by Saif *et al.* [69], "the elements of G represents the stresses in half plane due to an applied unit body force at (x', z'). For instance, $G_{xh}(x, z, x', z')$ is equal to the $\sigma_{xx}(x, z)$ due to the unit load action along the scan direction applied at (x', z'), whereas $G_{xv}(x, z, x', z')$ is equal to the $\sigma_{xx}(x, z)$ due to the unit load action in the transverse direction applied at (x', z')". The elements of G are explained in Appendix.

(2) stress due to normal stress tension $N = \frac{\alpha(T)E(T)T}{1-2\nu(T)}$ on the boundary (*z=0*). The normal stress σ_{xx} due to the tension can be obtained from

$$\sigma_{xx} = \frac{2}{\pi}\int_{-\infty}^{\infty} \frac{[(s-x)T - zN](s-x)^2}{((s-x)^2+z^2)^2}\, ds \tag{3.38}$$

By putting temperature (*T=0*) and normal tension $N = \frac{\alpha(T)E(T)T}{1-2\nu(T)}$, the integral reduces to

$$\sigma_{xx}(x, z = 0) = \frac{\alpha(T)E(T)T}{1-2\nu(T)} \tag{3.39}$$

(3) hydrostatic stress can be obtained as $-\frac{\alpha(T)E(T)T}{1-2\nu(T)}$ as explained in the work of Cowper [70].

Accordingly, the stress due to the non-uniform heating in the build part is calculated by the combination of the different sources of stresses due to the body forces, normal stress tension, and hydrostatic stress as described by Saif *et al.* [69]:

$$\begin{aligned}\sigma_{xx}(x,z) = -\frac{\alpha(T)E(T)}{1-2\nu(T)}\int_0^\infty\int_{-\infty}^\infty (G_{xh}\frac{\partial T}{\partial x}(x',z') \\ + G_{xv}\frac{\partial T}{\partial z}(x',z'))dx'dz' \\ + \frac{2z}{\pi}\int_{-\infty}^\infty \frac{p(s)(s-x)^2}{((s-x)^2+z^2)^2}ds - \frac{\alpha(T)E(T)T(x,z)}{1-2\nu(T)}\end{aligned} \tag{3.40}$$

$$\begin{aligned}\sigma_{zz}(x,z) = -\frac{\alpha(T)E(T)}{1-2\nu(T)}\int_0^\infty\int_{-\infty}^\infty (G_{zh}\frac{\partial T}{\partial x}(x',z') \\ + G_{zv}\frac{\partial T}{\partial z}(x',z'))dx'dz' \\ + \frac{2z^3}{\pi}\int_{-\infty}^\infty \frac{p(s)}{((s-x)^2+z^2)^2}ds - \frac{\alpha(T)E(T)T(x,z)}{1-2\nu(T)}\end{aligned}$$

$$\sigma_{xz}(x,z) = -\frac{\alpha(T)E(T)}{1-2\nu(T)}\int_0^{\infty}\int_{-\infty}^{\infty}\Big(G_{xzh}\frac{\partial T}{\partial x}(x',z') + G_{xzv}\frac{\partial T}{\partial z}(x',z')\Big)dx'dz' + \frac{2z^2}{\pi}\int_{-\infty}^{\infty}\frac{p(s)(s-x)}{((s-x)^2+z^2)^2}ds$$

$$\sigma_{zz}(x,z) = \nu(T)(\sigma_{xx}+\sigma_{zz}) - \alpha(T)E(T)T(x,z) \tag{3.41}$$

where, α is the coefficient of the thermal expansion, E represents the elastic modulus, $\frac{\partial T}{\partial x}$ is the temperature gradient and $p(s)$ is expressped by:

$$p(s) = \frac{\alpha(T)E(T)T(x,z=0)}{1-2\nu(T)} \tag{3.42}$$

The closed-form solution of thermal stress can be derived as;

$$\sigma_{xx}(i,j) = -\frac{\alpha E(T)}{1-2\nu}\left(G_{xh}T_x + G_{xv}T_z\right)\left(|x_i - x_{i-1}|\left|z_j - z_{j-1}\right|\right) + \frac{\frac{2z}{\pi}(p(s)(s-x)^2}{((s-x)^2+z^2)^2}|x_i - x_{i-1}| - \frac{\alpha ET}{1-2\nu}$$

(3.43)

where $T_x = \frac{T(i,j)-\mathrm{T(i-1,j)}}{|x_i - x_{i-1}|}$, $T_z = \frac{T(i,j)-\mathrm{T(i,j-1)}}{|z_j - z_{j-1}|}$ and i, j represent a location in the 2D medium at which the stress is calculated. The closed-form solutions of σ_{zz} and σ_{xz} can be derived using the same method.

3.3 Residual Stress Modeling

At elevated temperatures, the yield strength of the materials approaches zero. Accordingly, the AM part experiences a high magnitude of plastic deformation due to heating cycles and cooling cycles. If the stress passes the yield strength, upon unloading (cooling in this situation) some amount of stress remains in the body which is known as residual stress. The residual stress is inherent in all the AM parts and can be reduced or eliminated with proper control and optimization of process parameters or post-processing techniques such as pitting, and heat treatment since it has an elastic nature.

Both the in-plane and out of plane residual stress distributions are obtained from incremental plasticity and kinematic hardening behavior of metal according to the conservation of volume in plastic deformation in coupling with equilibrium and compatibility conditions. McDowell *et al.* [71] proposed an algorithm to predict the residual stress in rolling. This algorithm has several advantages including high computational efficiency, rapid and accurate prediction of residual stress; however, this algorithm has several limitations; First, the stress along the build direction (σ_{zz}) is assumed to be elastic. In AM processes, the stress along the build direction has a high magnitude.

Thus, the stress along the build direction should be solved along with σ_{xx}, and σ_{yy}. In this case, there are two equations with three unknowns, which cannot be solved using McDowell model. Second, this algorithm does not consider the conservation of volume in plastic deformation. Qi *et al.* [72] explained that these limitations may reduce the precision of the predicted residual stress. Thus the modified algorithm is proposed to eliminated the abovementioned limitations.

To determine the yield surface, the Johnson-Cook method is used to model the flow stress as;

$$k = \frac{1}{\sqrt{3}}(A + B{\varepsilon_{eff}^{p}}^{n})(1 + Cln\left(\frac{\dot{\varepsilon}_{eff}^{p}}{\dot{\varepsilon}_0}\right))(1 - \left[\frac{T - T_0}{T_m - T_0}\right]^m) \tag{3.44}$$

where k is material yield stress, ε_{eff}^{p} represents the effective plastic strain, $\dot{\varepsilon}_{eff}^{p}$ is the effective plastic strain rate, T is the temperature of material, T_m is the melting point of material, and T_0 is the initial temperature.

The effective plastic strain and strain rate are defined as

$$\varepsilon_{eff}^{p} = \frac{\sqrt{2}}{3}\sqrt{(\varepsilon_{xx}^{p} - \varepsilon_{yy}^{p})^2 + (\varepsilon_{yy}^{p} - \varepsilon_{zz}^{p})^2 + (\varepsilon_{zz}^{p} - \varepsilon_{xx}^{p})^2 + 6(\varepsilon_{xz}^{p})^2} \tag{3.45}$$

$$\dot{\varepsilon}^{p}_{eff} = \sqrt{\frac{2}{3}} \sqrt{(\dot{\varepsilon}^{p}_{xx})^2 + (\dot{\varepsilon}^{p}_{yy})^2 + (\dot{\varepsilon}^{p}_{zz})^2 + (\dot{\varepsilon}^{p}_{xz})^2}$$

(3.46)

The yielding criterion is obtained for an isotropic material. Kinematic hardening is considered by employing backstress tensor (α_{ij})

$$F_{yield} = \frac{3}{2}\left(S_{ij} - \alpha_{ij}\right)\left(S_{ij} - \alpha_{ij}\right) - k^2 = 0$$

(3.47)

$$\begin{cases} F_{yield} < 0 \; elastic \; deformation \\ F_{yield} > 0 \; plastic \; deformation \end{cases}$$

where $S_{ij} = \sigma_{ij} - (\sigma_{kk}/3)\delta_{ij}$ is the deviatoric stress, k is the material yield threshold which is determined using material flow stress model.

$\dot{\alpha_{ij}} = \langle \dot{S_{kl}} n_{kl} \rangle n_{ij}$ shows the back stress tensor rate in linear kinematic hardening, where $< >$ is MacCauley bracket and is expressed as $\langle x \rangle = 0.5(x + |x|)$, and $n_{ij} = \frac{S_{ij} - \alpha_{ij}}{\sqrt{2}\, k}$ which is the components of unit normal in plastic strain rate direction, and k is the material flow stress threshold.

If $F_{yield} < 0$, material is in elastic region and the stresses can be obtained from the Hook's Law.

If $F_{yield} > 0$, the total plastic strains can be obtained by calculating the plastic strains incrementally during cyclic heating and cooling. The plastic strain rate is determined by Khan and Huang [73] as

$$\dot{\varepsilon}_{ij}^{P} = \frac{1}{h} \langle \dot{S_{kl}} n_{kl} \rangle n_{ij} \tag{3.48}$$

where h is the plastic modulus. In the elastic-plastic case where the $F_{yield} \geq 0$, the strain rate along the scan direction and transverse direction can be calculated using modified McDowell algorithm. In the elastoplastic loading the total strain is a combination of elastic part and plastic part as

$$\dot{\varepsilon}_{xx} = \dot{\varepsilon}_{xx}{}^{e} + \dot{\varepsilon}_{xx}{}^{p}$$

$$\dot{\varepsilon}_{yy} = \dot{\varepsilon}_{yy}{}^{e} + \dot{\varepsilon}_{yy}{}^{p}$$

$$\dot{\varepsilon}_{zz} = \dot{\varepsilon}_{zz}{}^{e} + \dot{\varepsilon}_{zz}{}^{p} \tag{3.49}$$

According to the conservation of volume in plastic deformation;

$$\dot{\varepsilon}_{xx}{}^{p} + \dot{\varepsilon}_{yy}{}^{p} + \dot{\varepsilon}_{zz}{}^{p} = 0 \tag{3.50}$$

Based on plain strain assumption

$$\dot{\varepsilon}_{yy}{}^{e} = \dot{\varepsilon}_{yy}{}^{p} = 0 \tag{3.51}$$

Then,

$$\dot{\varepsilon}_{xx}{}^{p} + \dot{\varepsilon}_{zz}{}^{p} = 0 \tag{3.52}$$

Taking plastic flow rule (Equation (3.48)) into Equation (3.52);

$$\frac{1}{h}\langle \dot{S_{kl}} n_{kl} \rangle (n_{xx} + n_{zz}) = 0 \tag{3.53}$$

Based on plastic loading condition;

$$\langle \dot{S_{kl}} n_{kl} \rangle > 0 \tag{3.54}$$

Therefore;

$$(n_{xx} + n_{zz}) = 0 \tag{3.55}$$

Taking $n_{ij} = \frac{S_{ij} - \alpha_{ij}}{\sqrt{2}\, k}$, and $S_{ij} = \sigma_{ij} - ({}^{\sigma_{kk}}/_{3})\delta_{ij}$ into Equation (3.53);

$$\sigma_{yy} = \frac{1}{2}(\sigma_{xx} + \sigma_{zz}) \tag{3.56}$$

The incremental form of Equation (3.56) can be written as;

$$\dot{\sigma}_{yy} = \frac{1}{2}(\dot{\sigma}_{xx} + \dot{\sigma}_{zz}) \tag{3.57}$$

Then, by solving three equations with three unknowns, (σ_{xx}, σ_{yy}, σ_{zz}) can be obtained as

$$\begin{cases} \frac{1}{E}\left[\dot{\sigma}_{xx} - \upsilon\left(\dot{\sigma}_{yy} - \dot{\sigma}_{zz}\right)\right] + \alpha\Delta T + \frac{1}{h}\left(\dot{\sigma}_{xx}n_{xx} + \dot{\sigma}_{yy}n_{yy} + \dot{\sigma}_{zz}n_{zz} + 2\dot{\sigma}^{*}_{xz}n_{xz}\right)n_{xx} = \\ \psi\left(\frac{1}{E}\left[\dot{\sigma}^{*}_{xx} - \upsilon\left(\dot{\sigma}_{yy} - \dot{\sigma}^{*}_{zz}\right)\right] + \alpha\Delta T + \frac{1}{h}(\dot{\sigma}^{*}_{xx}n_{xx} + \dot{\sigma}_{yy}n_{yy} + \dot{\sigma}^{*}_{zz}n_{zz} + 2\dot{\sigma}^{*}_{xz}n_{xz})n_{xx}\right) \\ \frac{1}{E}\left[\dot{\sigma}_{yy} - \upsilon(\dot{\sigma}_{xx} - \dot{\sigma}_{zz})\right] + \alpha\Delta T + \frac{1}{h}\left(\dot{\sigma}_{xx}n_{xx} + \dot{\sigma}_{yy}n_{yy} + \dot{\sigma}_{zz}n_{zz} + 2\dot{\sigma}^{*}_{xz}n_{xz}\right)n_{yy} = 0 \\ \dot{\sigma}_{yy} = \frac{1}{2}(\dot{\sigma}_{xx} + \dot{\sigma}_{zz}) \end{cases} \tag{3.58}$$

where, $\dot{\sigma}^{*}_{xx}, \dot{\sigma}^{*}_{zz}, \dot{\sigma}^{*}_{xz}$ are the elastic thermal stresses calculated from Equation (3.40). ψ is the hybrid function which depends on the modulus ratio (h/G) as;

$$\psi = 1 - \exp\left(-\xi\frac{3h}{2G}\right) \tag{3.59}$$

where $\xi = 0.15$ is the algorithm constant, h is the plastic modulus, and $G = E/(2(1 + \upsilon))$is the elastic shear modulus. ψ approaches zero as h approaches zero (perfect plasticity), and ψ approaches unity as h approaches infinity (initial yielding). ψ is always between unity and zero.

Three systems of equations are solved simultaneously for $\dot{\sigma}_{xx}$, $\dot{\sigma}_{yy}$, and $\dot{\sigma}_{zz}$ for each elastic-plastic increment of strain.

After laser has scanned one layer, elastic stresses are relaxed to meet the boundary condition prescribed by Merwin and Johnson [74] as

$$\varepsilon_{xx}^{r}=0,\quad \sigma_{xx}^{r}=f_1(z),\quad \varepsilon_{yy}^{r}=0,\quad \sigma_{yy}^{r}=f_2(z),\quad \varepsilon_{zz}^{r}=f_3(z),\quad \sigma_{zz}^{r}=0,$$

$$\gamma_{xz}^{r}=f_4(z),\ \sigma_{xz}^{r}=0 \tag{3.60}$$

Finally, only stresses and strains parallel to the surface ($\sigma_{xx}^{r},\quad \sigma_{yy}^{r},\gamma_{xz}^{r}$) remain non-zero. The only non-zero strain is ε_{zz}^{r}, resulting from surface compression. Accordingly, the non-zero components $\varepsilon_{xx}^{r},\sigma_{zz}^{r},$ and σ_{xz}^{r} at the end of each pass should incrementally relaxed to zero as;

$$\Delta\sigma_{zz}=-\frac{\sigma_{zz}^{r}}{M},\Delta\sigma_{xz}=-\frac{\sigma_{xz}^{r}}{M},\Delta\varepsilon_{xx}=-\frac{\varepsilon_{xx}^{r}}{M} \tag{3.61}$$

where M is the number of increments (e.g.100-1000) for relaxation procedure.

Using Equation (3.56), for the case of purely elastic relaxation increment ($F_{yield}\leq 0$), the relaxation process is described by general Hook's law as

$$\begin{cases}\Delta\sigma_{xx}=\frac{E\Delta\varepsilon_{xx}+(1+\upsilon)(\Delta\sigma_{zz}\upsilon-E\alpha\Delta T)}{(1-\upsilon^2)}\\ \Delta\sigma_{yy}=\frac{\upsilon E\Delta\varepsilon_{xx}+(1+\upsilon)(\Delta\sigma_{zz}\upsilon-E\alpha\Delta T)}{(1-\upsilon^2)}\end{cases} \tag{3.62}$$

$\Delta's$ replace the time derivative.

For the elastic-plastic case ($F_{yield}>0$), the released stresses calculated as

$$\begin{cases} \Delta\sigma_{xx} = \dfrac{D - \left(\frac{1}{E} + \frac{1}{h} n_{xx} n_{yy}\right) \Delta\sigma_{yy} - \alpha\Delta\mathrm{T}}{-\frac{\upsilon}{E} + \frac{1}{h} n_{xx} n_{yy}} \\ \Delta\sigma_{yy} = \dfrac{(-\frac{\upsilon}{E} + \frac{1}{h} n_{xx} n_{yy})(C - \alpha\Delta\mathrm{T}) - (\frac{1}{E} + \frac{1}{h} n_{xx} n_{xx})(D - \alpha\Delta\mathrm{T})}{\left[(-\frac{\upsilon}{E} + \frac{1}{h} n_{xx} n_{yy})^2 - (\frac{1}{E} + \frac{1}{h} n_{xx} n_{xx})(\frac{1}{E} + \frac{1}{h} n_{yy} n_{yy})\right]} \end{cases}$$

(3.63a, b)

$$\text{where} \begin{cases} C = \Delta\varepsilon_{xx} + \left(\frac{\upsilon}{E} - \frac{1}{h} n_{xx} n_{zz}\right) \Delta{\sigma_{zz}}^{*} - \frac{2}{h} \Delta{\sigma_{xz}}^{*} n_{xz} n_{xx} \\ D = \left(\frac{\upsilon}{E} - \frac{1}{h} n_{yy} n_{zz}\right) \Delta{\sigma_{zz}}^{*} - \frac{2}{h} \Delta{\sigma_{xz}}^{*} n_{xz} n_{yy} \end{cases}$$

(3.64)

The residual stresses in the scan direction and build direction are then calculated as the remaining stresses after relaxation. Residual stress and stress relaxation algorithm are shown in Figure 7.

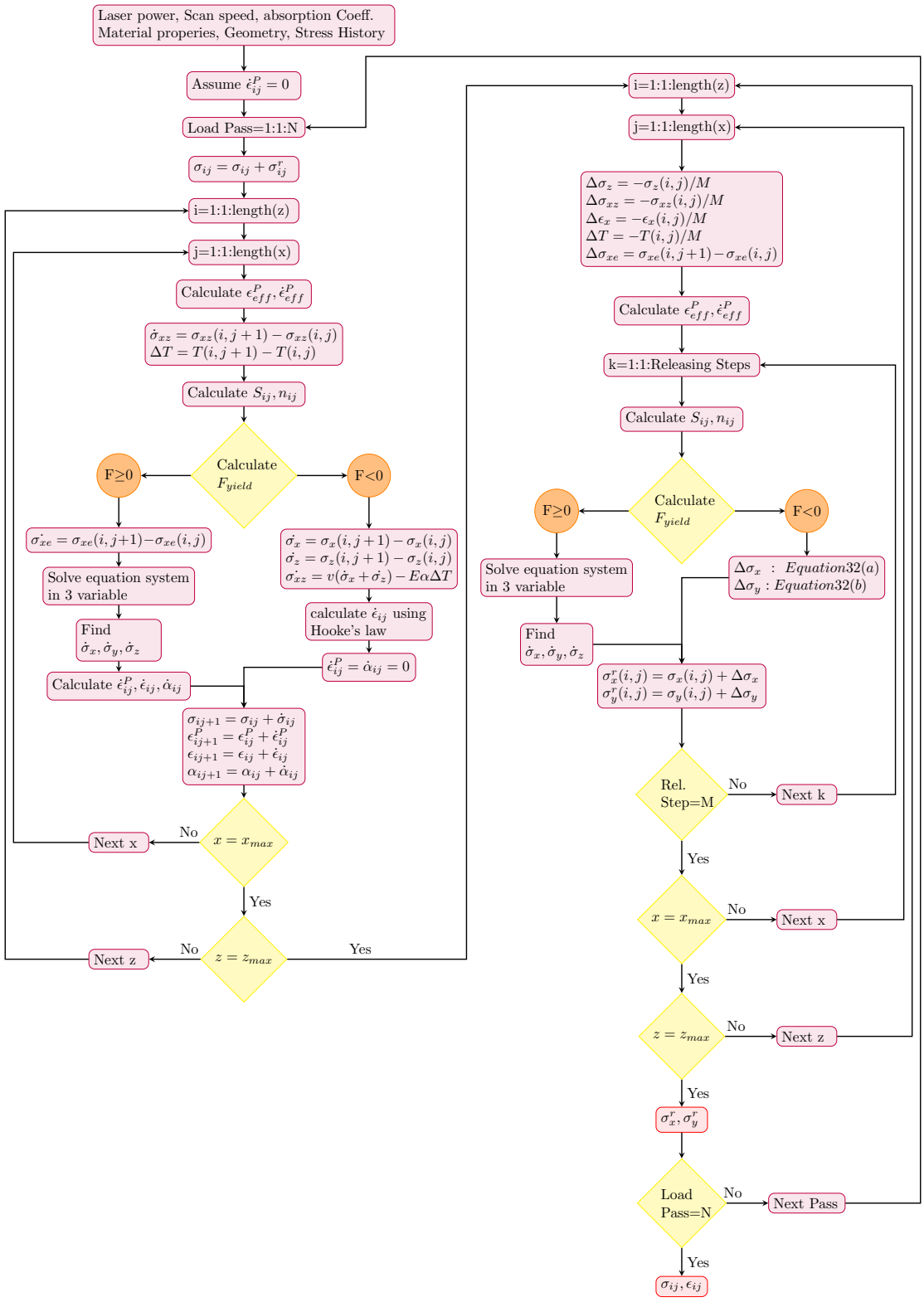

Figure 7. Residual stress and relaxation algorithms.

3.4 Grain Size Modeling

During AM process, new grains are formed during the continuous cooling. The number of the newly formed grains (n), during cooling process from $T(t_1)$ to $T(t_2)$ can be computed by the sum of the product of nucleation rate per unit volume $I(T)$, the fraction transformed $1 - X(T_i)$, a time interval Δt_i, and a temperature difference ΔT_i, as

$$n = \sum_{i=1}^{k} I(T_i)\left(1 - X(T_i)\right)\Delta t_i = \sum_{i=1}^{k} \frac{I(T_i)\left(1-X(T_i)\right)\Delta T_i}{\frac{\Delta T_i}{\Delta t_i}} \tag{3.65}$$

During continuous cooling, the time for which the specimen is at each temperature and the difference between the successive temperatures, can be considered to approach zero. The numbers of newly formed grains will then be given by integrating over the range of temperature from $T(t_1)$ to $T(t_2)$

$$n(T) = \int_{T(t_1)}^{T(t_2)} \frac{I(T)\left(1-X(T)\right)dT}{-\frac{dT}{dt}} \tag{3.66}$$

where $-\frac{dT}{dt} = Q(T)$ represents the cooling rate.

In the case of homogeneous nucleation, the volume fraction occupied by all the nodules nucleated during cooling can be calculated as

$$X(T) = 1 - \exp\left[\frac{-4\pi}{3}\int_{T}^{T_e}\frac{I_s(T_a)}{Q(T_a)}\left\{\int_{T}^{T_a}\frac{G(T)}{Q(T)}dT\right\}^3 dT_a\right] \tag{3.67}$$

where T_a is a temperature at time t_a, $I_s(T_a)$ is the nucleation rate per unit volume, and $G(T)$ is the growth rate. When the parent phase completely transformed to a new phase the nominal diameter of the grain size can be obtained as [75]

$$d = \left(\frac{2}{3n}\right)^{1/3} \tag{3.68}$$

The grain size model is validated in [76].

3.5 Microstructure Affected Residual Stress Modeling

During the thermal loading, the grain size is altered at the subsurface through dynamic recrystallization (DRx) and subsequent recovery. The yield strength of the alloys is largely determined by the size of nucleated grains, and it has a substantial influence on residual stress build-up. In this work, a physics-based analytical model is proposed to predict the residual stress considering the microstructure of the additively manufactured part. The thermal signature of this process is predicted using a transient moving heat source approach as explained in section 3.1. Due to the high-temperature gradient innate in this process, material may experience high thermal stress which often exceeds the yield strength. The

thermal stress is obtained from Green's functions of stresses due to the point body load as explained in section 3.2.

The modified Johnson-Cook flow stress model is used to determine the yield surface. To include the effect of grain size on yield strength parameter (A) in the flow stress model, the Hall-Patch equation [77] is introduced as ;

$$A = A_{hp} + K_{hp} d^{-0.5} \tag{3.69}$$

where d is the average grain size obtained from dynamic recrystallization and grain refinement models as explained in previous section, A_{hp}, and K_{hp} are material constants. Then the modified J-C flow stress model could be written as

$$\sigma = (A_{hp} + K_{hp} d^{-0.5} + B{\varepsilon_{eff}^{p}}^{n})(1 + C ln\left(\frac{\dot{\varepsilon}_{eff}^{p}}{\dot{\varepsilon}_0}\right))(1 - \left[\frac{T - T_0}{T_m - T_0}\right]^m) \tag{3.70}$$

where ε_{eff}^{p} is the effective plastic strain, $\dot{\varepsilon}_{eff}^{p}$ is the effective plastic strain rate, T is the temperature of material, T_m is the melting point of material, and T_0 is the initial temperature. The terms A_{hp}, K_{hp}, B, C, n, m and $\dot{\varepsilon}_0$ are the material constant.

Then, as a result of the cyclic heating and cooling and the fact that the material is yielded, the residual stress build-up is precited from incremental plasticity and kinematic hardening behavior of the metal according to the property of volume invariance in plastic deformation in coupling with the equilibrium and compatibility conditions as explained in section 3.3.

3.6 Finite Element Modeling of Temperature Field and Thermal Stress

3.6.1 Thermal Problem Description in FEM

The governing equation for the heat transfer problem in metal AM is the time-dependent energy equation:

$$\rho(T)C_p(T)\frac{dT}{dt} = -\nabla.\, q(r,t) + Q(r,t) \tag{3.71}$$

where ρ is the material density, C_p is the specific heat capacity, T is the temperature, t is the time, Q is the heat source, r is the relative reference coordinate, and q is the heat flux vector, calculated as:

$$q = -k(T)\nabla T \tag{3.72}$$

where $k(T)$ is the thermal conductivity of the material.

The laser power is modeled as a moving heat flux boundary condition in the heat transfer problem, in which the moving laser power source is modeled as a moving round spot with radius R, and the center of the round spot moves with time on the surface of a build with a constant speed (v).

The source power intensity from the laser is modeled as a uniformly distributed volumetric heat source:

$$I = \frac{P\alpha}{\pi R^2 l} \tag{3.73}$$

with P indicating laser power, α denoting absorptivity coefficient, R is the laser spot radius, and l is the layer thickness.

The energy required for the phase change from solid to liquid (and vice versa) is also considered using latent heat of melting. The heat loss due to evaporation, convection, and radiation have been neglected in the present simulation.

3.6.2 Mechanical Problem Description in FEM for Validation

A thermal dependent, static mechanical analysis is performed to obtain the mechanical response of the build part in the AM process. The solution of the heat transfer problem is transferred from the heat transfer module as the source to the solid mechanics module as the destination. The governing equation for the stress is:

$$\nabla\sigma = 0 \tag{3.74}$$

where σ is the stress tensor. Here the mechanical response is modeled in a static manner. The inertial terms and time- dependent terms are ignored from the momentum equation. Also, the body force i.e. gravity is neglected from the present model. For a Ti-6Al-4V alloy which shows hardening behavior after the stress reaches the yield strength, an elastoplastic hardening model is used. The elastic behavior is given by the Hook's law:

$$\sigma = 2\mu\varepsilon^e + \lambda tr(\varepsilon^e)I \tag{3.75}$$

where μ and λ are Lame constants and I is unit second order tensor. The yield function is given by the von Mises criterion:

$$f(\sigma; r) = J_2(\sigma) - \sigma_0(r) \leq 0 \tag{3.76}$$

where $J_2(\sigma)$ is the second deviatoric stress invariant, $J_2(\sigma) = \sqrt{3s:s/2}$ in which s is the deviatoric stress tensor and $\sigma_0(r)$ is the isotropic hardening law given by the Swift law:

$$\sigma_0(r) = K(r + r_0)^n \tag{3.77}$$

where K is the consistency of the material, n is the isotropic hardening exponent, r is the hardening variable related to the equivalent plastic strain and r_0 is a regularization parameter, which can also be used to define the initial yield stress.

The total strain is given as:

$$\varepsilon_{total} = \varepsilon_e + \varepsilon_p + \varepsilon_T \tag{3.78}$$

where $\varepsilon_e, \varepsilon_p,$ and ε_T are the elastic strain, plastic strain, and thermal strain, respectively.

The isotropic thermal strain is obtained as:

$$\varepsilon_T = \alpha(T - T_{ref}) \tag{3.79}$$

where α is the isotropic thermal expansion, T_{ref} is the reference temperature for the thermal stress at which the thermal strain is assumed to be zero.

CHAPTER 4. **MODELING RESULTS**

In this chapter, the modelling approaches to predict the temperature field, thermal stress, residual stress, grain size, and microstructure affected residual stress which are described in chapter 3 is implemented and the obtained results are compared to experimental data for several material systems such as Ti-6Al-4V and IN 718. The predicted temperature field is compared to experimental data and FEM results for the additive manufacturing of Ti-6Al-4V. Thermal stress distributions obtained from proposed analytical model is validated via FEM results for the components manufactured via Ti-6Al-4V. At the end, the proposed residual stress model is validated for different material systems including Ti-6Al-4V manufactured via powder feed system, IN718 manufactured via powder feed system and laser powder bed fusion system.

The temperature dependent t material properties of Ti-6Al-4V and IN718 are listed in Table 1 and Table 2, respectively.

The Johnson-Cook parameters of Ti-6Al-4V, and IN718 are listed in Table 3.

Table 1. Temperature dependent material properties of Ti-6Al-4V (Temperature is in ℃).

Density [Kg/m^3]	$\boldsymbol{\rho = 4420/(1 + \alpha \times T)^3}$
Thermal conductivity [W/m℃]	$K = 1.57 + 1.6e-2 \times T - 1e-6 \times T^2$

Table 1 continued.

Specific heat [J/Kg℃]	$C = 492.4 + 0.025 \times T - 4.18e - 6 \times T^2$	
Thermal expansion [1/℃]	$\begin{cases} \alpha = 7.43e - 6 + 5.56e - 9 \times T - 2.69e - 12 \times T^2 \\ \alpha = 10.291e - 6 \end{cases}$	$T < 827$ $T > 827$
Elastic modulus [GPa]	$E = 122.7 - 0.0565 \times T$	
Poisson's ratio	$\upsilon = 0.289 + 3.2e - 5 \times T$	
Yeild strength [MPa]	$\begin{cases} \sigma_Y = 1256 - 0.8486 \times T \\ \sigma_Y = 316 - 0.16 \times T \end{cases}$	$T < 112$ $T > 11$

Table 2.Temperature dependent material properties of IN718 (Temperature is in ℃).

Density g/$\boldsymbol{cm^3}$	
$\boldsymbol{\rho = 8.19 - 39.2 \times 10^{-2} T}$	25< T ≤1170
$\boldsymbol{\rho = 7.40 - 88.0 \times 10^{-2}(T - 1200)}$	$\boldsymbol{T > 1170}$
Thermal conductivity W/m℃	
$\boldsymbol{k = 39.73 - 24.0 \times 10^{-3}\ T + 2 \times 10^{-3}\ T^{-2}}$	$\boldsymbol{25 < T < 1170}$
$\boldsymbol{k = 29.6}$	$\boldsymbol{T > 1170}$
Specific heat J/kg℃	
$\boldsymbol{C_p = 420.24 + 0.026T - 4 \times 10^{-6}\ T^2}$	$\boldsymbol{25 < T \leq 1170}$

Table 2 continued.

$C_p = 650$	$T > 1170$
Thermal expansion 1/℃	
$\alpha = -9 \times 10^{-13}\ T^2 - 7.7 \times 10^{-9} T + 1.1 \times 10^{-5}$	$25 < T \leq 1100$
$\alpha = 1.8 \times 10^{-5}$	T>1100
Elastic modulus GPa	
$E = 5.2 \times 10^{-5}\ T^2 - 0.088T + 1.6 \times 10^{2}$	$25 < T \leq 798$
$E = 3.1 \times 10^{-5}\ T^2 - 0.23T + 2.9 \times 10^{2}$	$798 < T < 2500$
Yield strength MPa	
$\sigma_Y = -9 \times 10^{-10}\ T^4 - 1.2 \times 10^{-6}\ T^3 + 0.00026\ T^2 - 0.23T + 3.2 \times 10^{2}$	25<T<2500
Poisson's ratio	
$\nu = -4.8 \times 10^{-10}\ T^3 - 8.8 \times 10^{-7}\ T^2 - 0.00031T + 0.31$	25<T<2500

Table 3. Johnson-Cook parameters.

Material	A(MPa)	B(MPa)	C	n	m	$\dot{\varepsilon}_0$
Ti-6Al-4V [78]	997.9	653.1	0.025	0.45	0.6	1
IN718 [79]	980	1370	0.02	0.164	1.03	1

4.1 Temperature Field Prediction and Validation

4.1.1 2D Temperature Field Validated via FEM and Experiments

In this section, the temperature profile, maximum temperature and surface temperature are predicted and compared to the experimental and also FEM results. A 2D moving point heat source analysis is used in order to predict the temperature distribution associated with the dynamic heat deposition. The general differential equation of heat conduction in the 2D plane is used. In order to consider the moving heat source, it is assumed that the coordinate system moves with the heat source using a transformation equation. Finally, using the separation of variables, the closed-form solution of temperature is obtained as explained in section 3.1. The material properties of Ti-6Al-4V are assumed to be temperature dependent as listed in Table 1. The energy needed for solid state phase change is also considered using modified heat capacity. For further validation of this work, finite element analysis is used. The temperature profile is modeled using a moving heat source analysis. The user defined functions (UDF) code is written in ANSYS Fluent software to run a FEA on a 2D geometry, as shown in Figure 8. The build part material is Ti-6Al-4V. The heat loss from the surface due to conduction and radiation is considered. In numerical modeling, the material properties are assumed to be temperature dependent as shown in Figure 9.

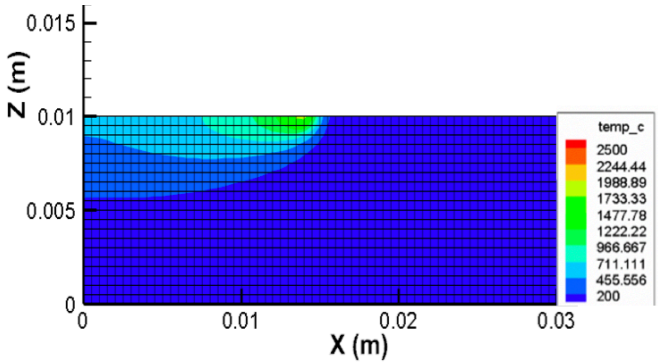

Figure 8. Representation of mesh and numerical model

The geometry of the build part is a rectangle shape of 30 mm × 10 mm. The quadratic element with the mesh size of 0.5 mm is chosen for all the simulations, as shown in Figure 8.

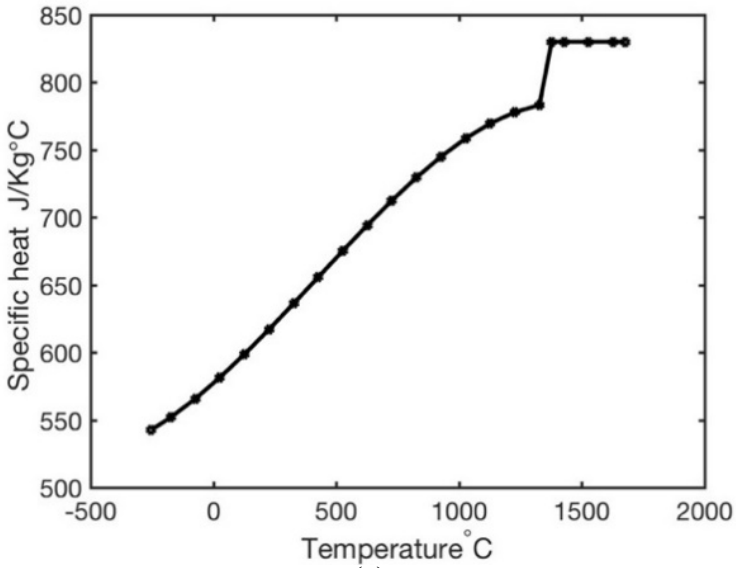

(a)

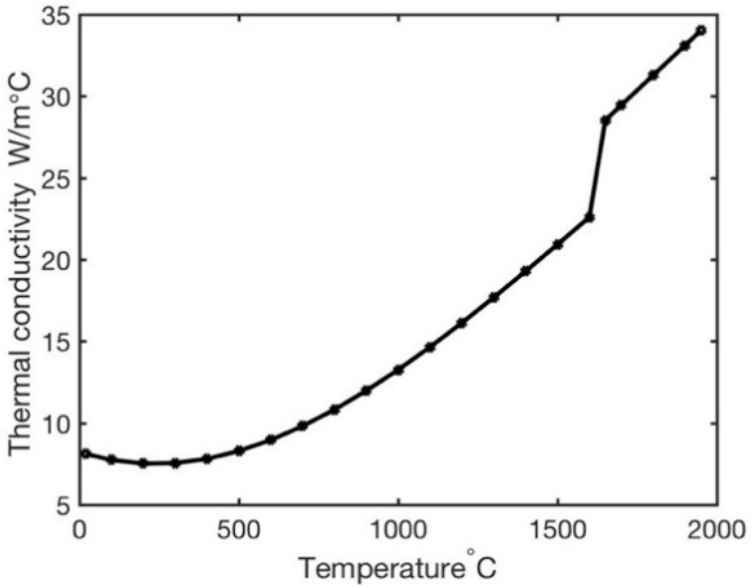

(b)

Figure 9. Material properties as a function of temperature, (a) Specific heat, (b) Thermal conductivity.

Table 4. Material parameters used for numerical modeling of temperature profile of Ti-6Al-4V.

Name	Value
Thermal radiation coefficient ($W/m^2 \cdot °C^4$)	5.67×10^{-8}
Heat transfer coefficient ($W/ m^2 \cdot °C$)	24
Material emissivity	0.9
D	[0.2–0.4]
Gaussian shape factor	2
Laser spot radius (mm)	0.7
Ambient temperature	25

To validate the proposed model, the experimental temperature data are also used from the work of Pauzet [80]. The Ti-6Al-4V samples are manufactured using the DMD machine. The dimensions of the samples are 2 mm in width, 70 mm in depth and 80 mm in length. The temperature on the build part surface is measured using the thermocouple of type K. In order to control the experimental setup, the authors used a thermal-camera and a high-speed camera to provide comparison bases for the temperature and the melt-pool size. The DMD machine has used the laser with the wavelength of 1030 nm. The scanning speed of 0.2 m/min and 0.4 m/min and the laser power of 400 W and 600 W, are studied. The initial

temperature of each layer depends on the final temperature of the previous layer, as the process is multi-layered.

Figure 10 shows the temperature profile of the build part. The temperature is predicted using both analytical model and numerical model. The laser moves along the *x*-axis from left to right. The small red spot on top shows the laser location. The layer thickness is chosen to be 80 μm. The distance of the laser from the powder is 0.4 mm. For the same power, as the velocity is increased the maximum temperature is decreased since the powder has less time to absorb the energy. Different combinations of the process parameters are presented in Figure 10, specifically scanning speed and laser power.

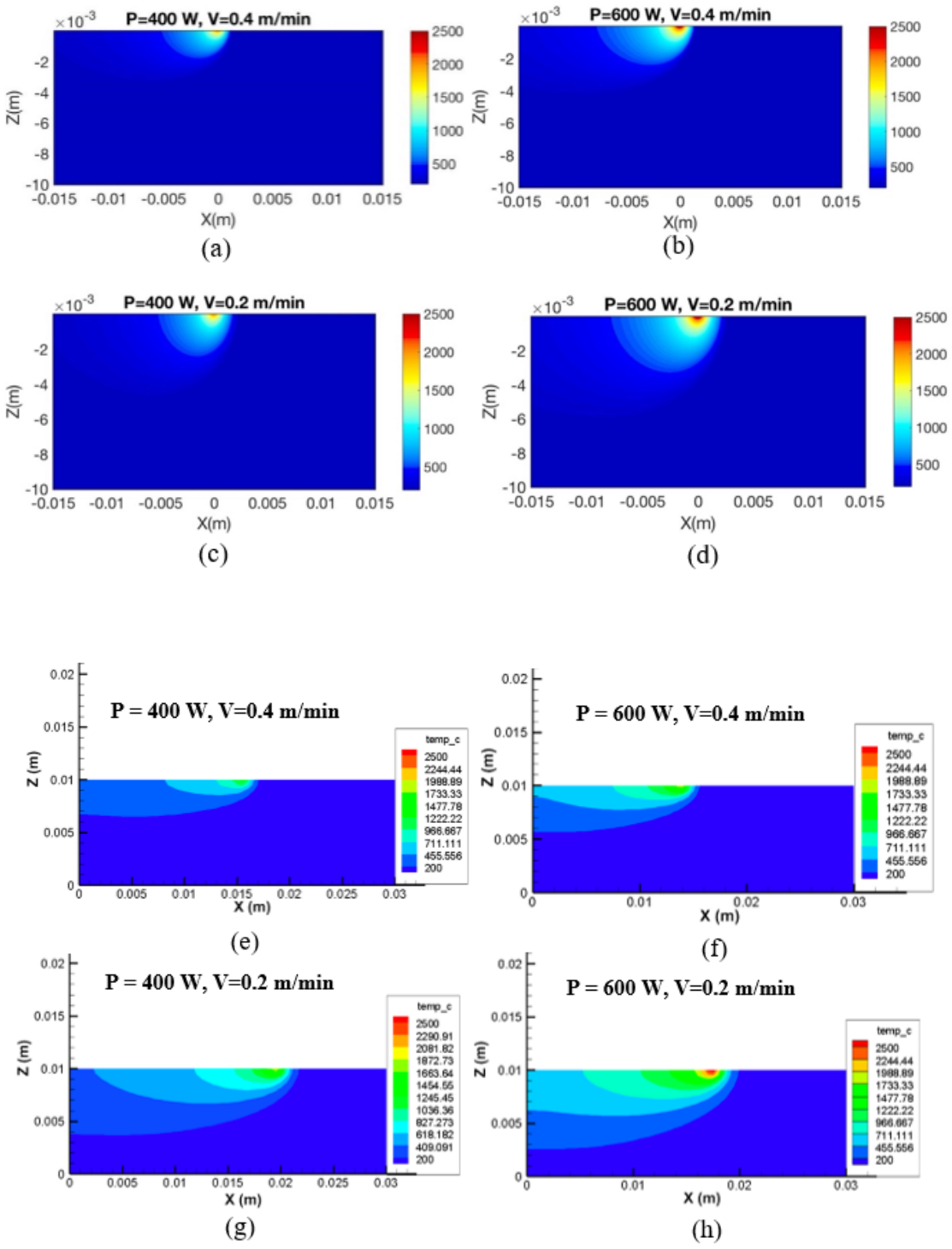

Figure 10. Predicted temperature profile using (a–d) physics-based analytical modeling; (e–h) numerical modeling.

The evolution of the surface temperature is plotted as a function of time for each case as shown in Figure 11. A study point will be chosen from the 2D geometry. When the laser is far away from the study point, the powder is at room temperature. As the laser approaches the study point, the temperature increases continuously. The maximum temperature on the curve corresponds to the moment that the laser is above the study point. After the laser passes the point, the temperature is decreased which shows that the material is cooling down. As shown in these plots, the cooling rate in the AM process is substantially high.

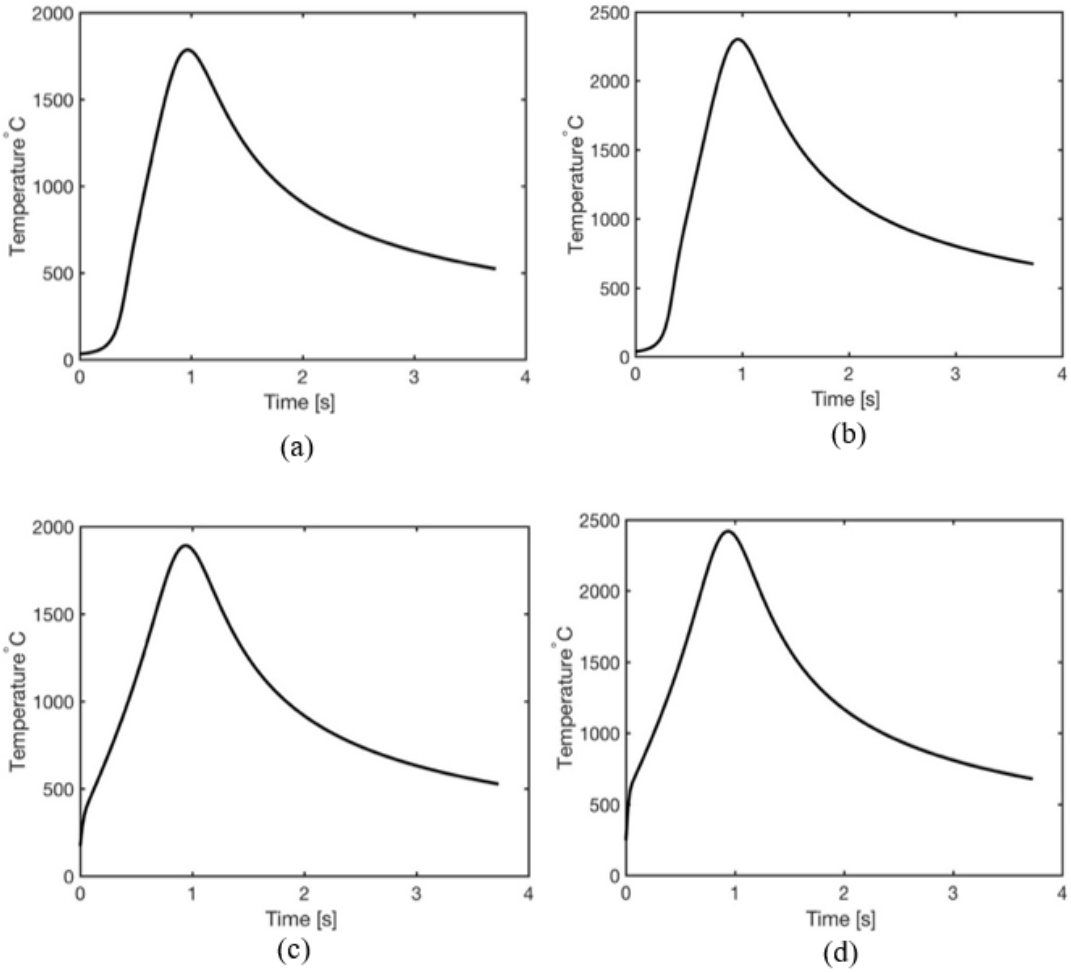

Figure 11. Evolution of surface temperature as a function of time for (a) P = 400 W, V = 0.4 m/min; (b) P = 600 W, V = 0.4 m/min; (c) P = 400 W, V = 0.2 m/min; (d) P = 600 W, V = 0.2 m/min.

In order to understand the influence of the process parameters on the maximum temperature, and surface temperature, a sensitivity study is designed to investigate both the scan speed and laser power. The short computational time associated with the analytical modeling approach allows for a better understanding of the influence of the process parameters as discussed previously. Figure 12 depicts the influence of the scan speed and laser power on temperature, as predicted by the analytical model and compared to the experimental results.

The results of the simulations from the analytical model illustrates that the maximum temperature decreases linearly as the scan speed increases since the material has less time to absorb the energy. On the other hand, for the fixed scanning speed, as the power increases the maximum temperature increases. The four experimental data are also pointed in Figure 12. The predicted temperature from the analytical model is slightly higher than the experimental values. This error is mainly because the temperature is measured using thermocouples which are a little below the surface.

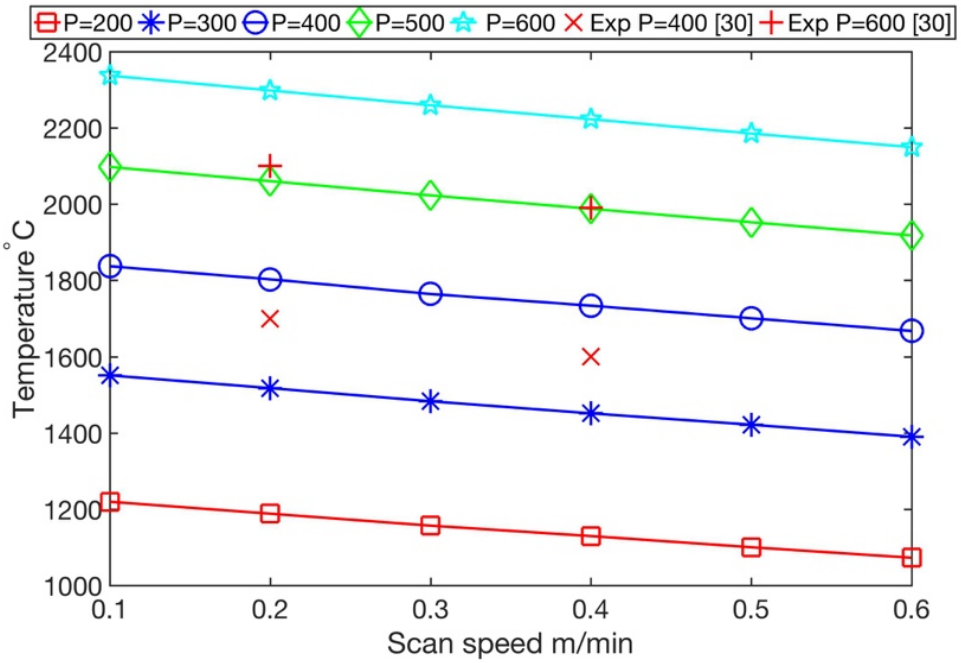

Figure 12. Effect of scan speed and laser power on peak temperature.

Figure 13 represents the influence of the laser on the surface temperature. As the power increases from 200 W to 600 W, the surface temperature increases for a fix scanning speed. On the other hand, the surface temperature will decrease as the scanning velocity increases from 0.1 m/min to 0.6 m/min for a fix laser power as shown in Figure 14.

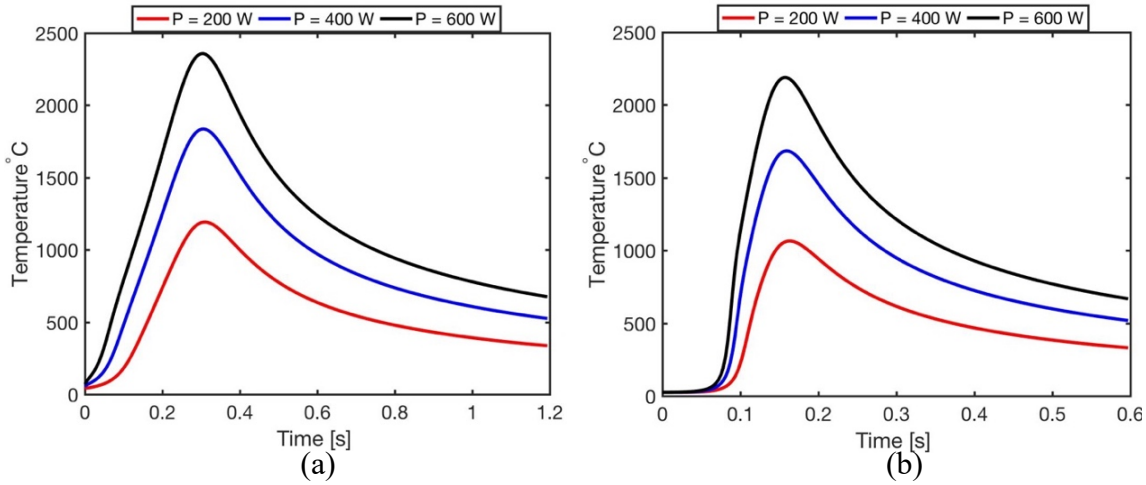

Figure 13. Comparison of evolution of surface temperature for (a) V = 0.3 m/min; (b) V = 0.6 m/min.

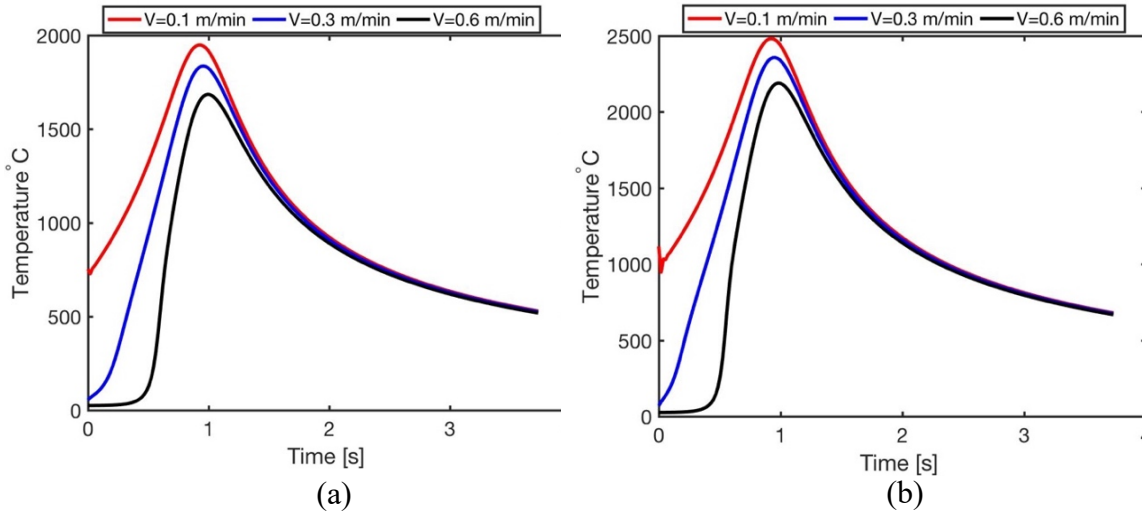

Figure 14. Comparison of evolution of surface temperature for (a) P = 400 W; and (b) P = 600 W.

As explained, the proposed model considers the multi-layer aspects of metal additive manufacturing. The effect of considering the layer addition on peak temperature is

compared to the obtained peak temperature without considering the layer addition, and also compared to the experimental results.

To further validate the proposed model, the peak temperature is plotted as a function of scanning speed for different laser powers. Two different values of laser power (400 W and 600 W) and scanning speed (0.2 m/min and 0.4 m/min) are chosen. The temperature considering the layer addition, the temperature not considering the layer addition, and also experimental values are compared. The values are listed in Table 5. The observations show that considering layer addition improves the prediction of temperature, as shown in Figure 15. For example, the predicted temperature for scanning velocity of 0.2 m/min and laser power of 400 W without considering the layer addition is 2042 °C, but when considering the layering aspect of AM, the predicted temperature reduces to 1802.8 °C which shows that it affects the heat transfer mechanisms.

Table 5. Comparison of temperature prediction among considering layer addition, not considering the layer addition, and experimental values.

Laser Power (W)	400	400	600	600
Scanning Speed (m/min)	0.2	0.4	0.2	0.4
Max Temperature w/o Layer	2043.7	1998.1	2603.7	2538.1
Max Temperature with Layer	1802.8	1733.6	2298.1	2222.7
Experimental Values	1730	1605	2100	1970

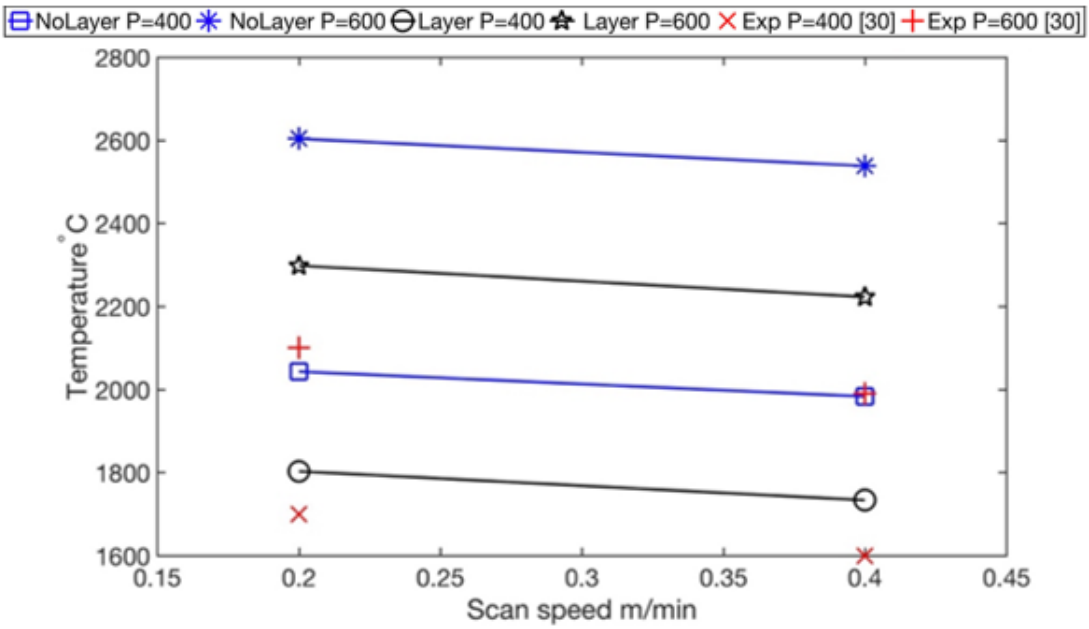

Figure 15. Comparison of prediction of temperature with and without considering the layers with experimental values.

A comparison is also conducted among the analytical model considering the layer addition and dwell time, numerical model and experimental values as shown in Figure 16. The main reason that the numerical solution has lower accuracy compare to that in analytical modeling is that the numerical modeling is iterative-based, and this would result in accumulation of the error over time, and also the computation starts from a random number to converge to a solution. However, this randomness would increase the obtained error since each starting point would result in different converged number.

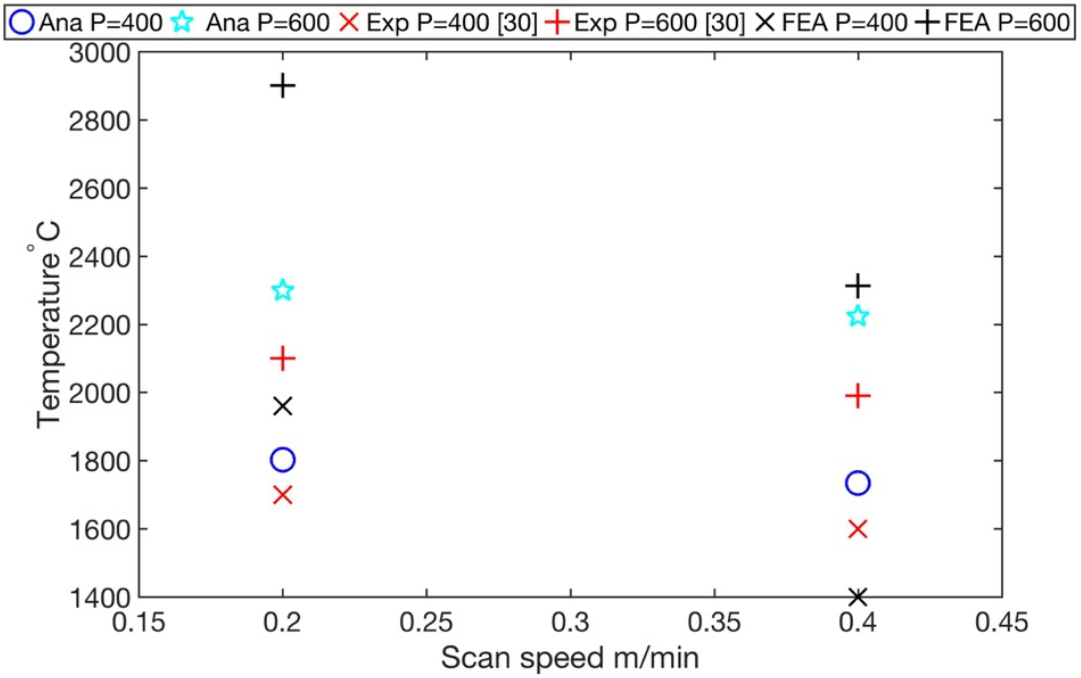

Figure 16. Comparison of predicted temperature among analytical model, experimental values, and FEA.

Overall, the temperature on the surface in terms of magnitude is well captured by both analytical and numerical approaches. The analytical model better approached the experimental measurements. This comparison shows the capability to accurately predict the temperature profile on the surface using the analytical modeling. The analytical approach also provides the power of a short computational time.

In order to illustrate the importance of considering the temperature dependent material properties, a sensitivity analysis is conducted to compare the predicted surface temperature with and without considering the property's temperature-sensitivity. The obtained results demonstrate a significant difference between them as shown in Figure 4.17. The thermal conductivity of the Ti-6Al-4V is 6.7 W/m·°C which results in a low rate of heat transfer in

the build part. However, the thermal conductivity of Ti-6Al-4V varies from 6 to 35 W/m·°C with respect to temperature. The increase in heat transfer rate induced by the increase in thermal conductivity, causes the predicted surface temperature decrease. In the cases that the temperature sensitivity of the material properties is considered, as the velocity increases from 0.2 m/min to 0.4 m/min, the variation of predicted surface temperature is less than 100 *°C.* However, when the temperature sensitivity of material properties is not considered, the variation of temperature is more than 1000 °C. As it is shown in Figure 17 the predicted temperature can be quite unrealistic without considering the material properties sensitivity to temperature.

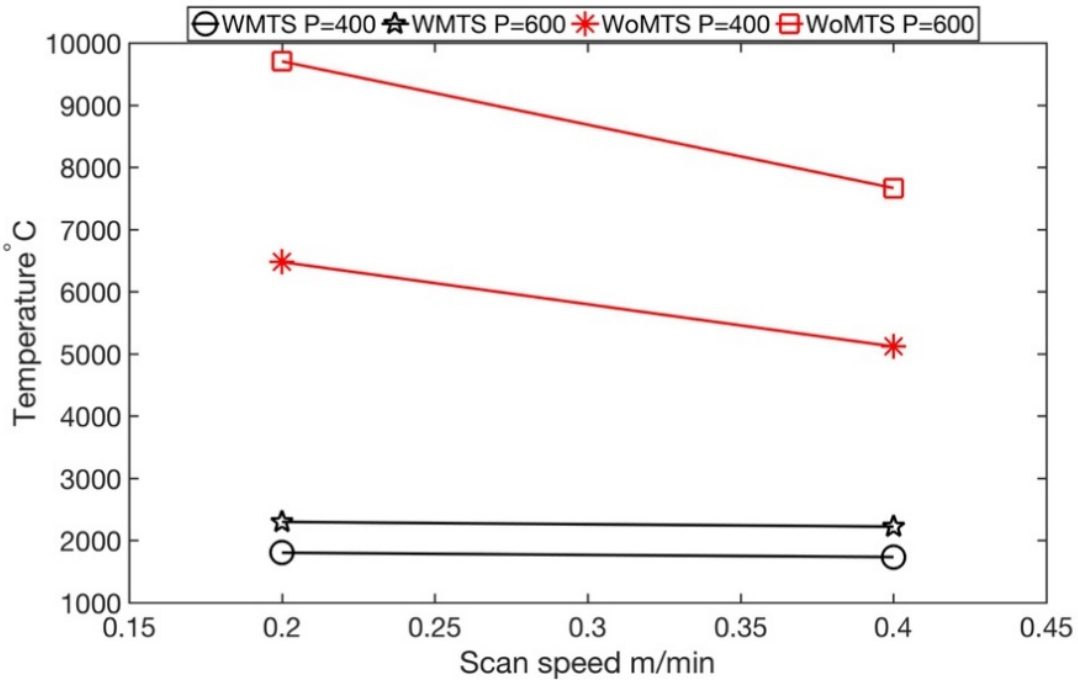

Figure 17. Comparison of predicted temperature considering the temperature sensitivity of material properties (WMTS), and without temperature sensitivity of material properties (WoMTS).

To further validated the proposed model, the predicted melt pool geometry is compared to the experimental measurements. The different process parameters such as laser power and scanning speed are used to predict the melt pool geometry. Figure 18 shows the experimental measurement of melt pool size from Peyre [81]. In this experiment, a high-speed C-Mos camera (Fastcam Photron) is used to measure the melt pool size which is generated by the DMD process.

Figure 19 demonstrates the predicted melt pool size and geometry for different process parameters in metal AM. The laser distance from powder is 1 μm.

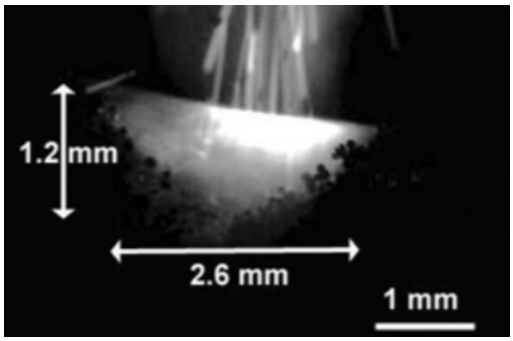

Figure 18. Experimental measurement of melt pool size for P = 600 W and V = 6 mm/s.

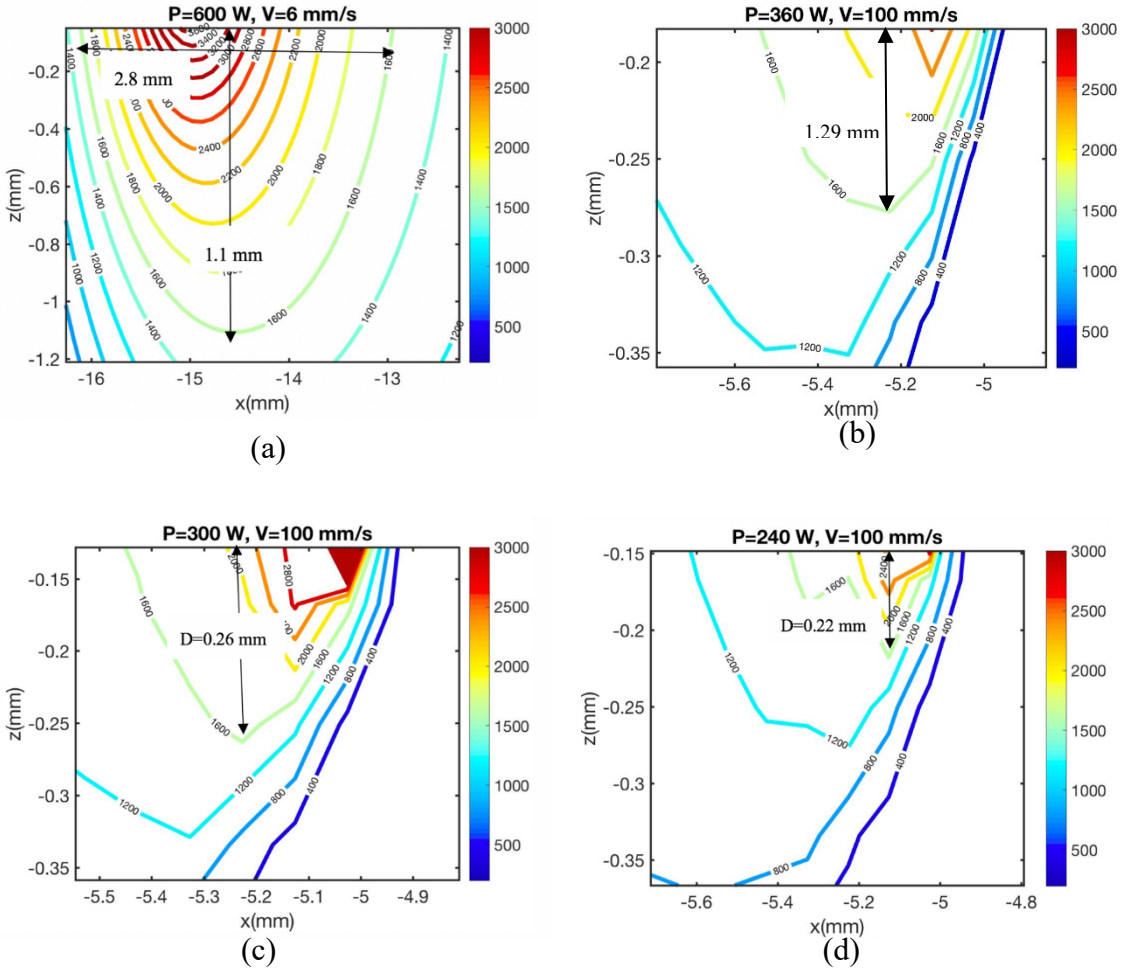

Figure 19. Predicted melt pool size in metal AM process for (a) P = 600W, V = 6mm/s; (b) P = 360W, V = 100mm/s; (c) P = 300W, V = 100mm/s; (d) P = 240W, V = 100mm/s

As shown in Figure 19, the melt pool depth and length are obtained using the analytical solution of temperature that is given in Section 3.1. The maximum error in length and depth is 7.6% and 3.7%, respectively. Table 6 listed the process parameters, predicted melt pool size, the experimental values, and also the corresponding error. Based on the calculated error, it is shown that the proposed 2D model can accurately capture the melt pool size. As a result, it eliminates the needs for doing costly experiments and also time-consuming FEM.

Table 6. Predicted and experimental measurements of melt pool size.

P (W)	V (mm/s)	Melt Pool Length (mm) Model	Melt Pool Length (mm) Exp/sim	Melt Pool Depth (mm) Model	Melt Pool Depth (mm) Exp/sim	Error in Length	Error in Depth
600 **[81]**	6	2.80	2.60	1.10	1.20	7.60%	2.00%
360 **[20]**	100	-	-	0.29	0.30	-	3.40%
300 **[20]**	100	-	-	0.26	0.27	-	3.70%
240 **[20]**	100	-	-	0.22	0.20	-	1.00%

4.1.2 Comparison of the Different Heat Source Models

In the section 3.1, five different 3D heat source models known as steady state moving point heat source, transient moving point heat source, transient semi-elliptical moving heat source, transient double elliptical moving heat source, and uniform moving point heat source are introduced. The accuracy and applicability of these models are investigated for the different range of process parameters such as scan speed and laser power. The predicted temperature field from each model is validated with experimental results of the melt pool geometry.

Eight different process parameters are selected from three different literatures to validate the introduced models as listed in Table 7. The material is Ti-6Al-4V. The laser power varies from 20-500 W, the scan speed varies from 6-1200 mm/s.

The first four data are selected from the work of Fu et al. [82]. In this work, a continuous laser of type Nd:YAG with the wavelength of 1.06 μm is used to melt the Ti-6Al-4V metallic powders with a layer thickness of 30 μm during the single track SLM process. The layer thickness is the deposited height of metallic powders in each layer. The wavelength of the laser and the material determine the absorption coefficient. Based on the reported wavelength and the material which is Ti-6Al-4V, the absorption coefficient would be 0.77. The laser power varies from 20 W to 80 W and the scan speed is fixed at 200 mm/s. The laser spot radius is 30 μm. The melt pool geometry is measured using optical microscopy based on the solidified microstructure.

The fifth experimental data in Table 7 is obtained from the work of Yiqun et al. [83] . In this work Ti-6Al-4V sample is built using laser melting deposition process. The laser power is 500 W and scan speed is 6 mm/s. Moreover, the layer thickness and laser spot radius are 45 μm and 26 μm, respectively. The melt pool is capture using thermal imager. More information about experimental data can be obtained in [83].

The last three experimental data are obtained from the work of Soylemez [84]. A continuous laser with a wavelength of 1.06 μm is used to build the Ti-6Al-4V parts with the fixed laser power of 300 W. The scan speed varies from 400 mm/s to 1200 mm/s. Furthermore, the layer thickness and laser spot radius are 30 μm and 50 μm, respectively. The samples are prepared using polishing and etching process to measure the melt pool geometry under an optical microscope, as reported in [84].

Table 7. List of process parameters used for model validation.

Sample	**1 [82]**	**2[82]**	**3[82]**	**4[82]**	**5[83]**	**6[84]**	**7[84]**	**8[84]**
Laser power(W)	20	40	60	80	500	300	300	300
Scan speed (mm/s)	200	200	200	200	6	400	800	1200
Laser spot radius (μm)	26	26	26	26	26	50	50	50
Layer thickness (μm)	30	30	30	30	45	30	30	30
Absorption ratio	0.77	0.77	0.77	0.77	0.77	0.77	0.77	0.77

The wide range of process parameters are selected to validated each of the analytical models.

The temperature field is predicted using five different heat source models. The predicted melt pool geometry such as melt pool depth, width and length is compared to experimental measurement. Different combinations of laser power and scan speed are used to cover all the ranges of process parameters ranging from low to high in order to investigate the applicability of each model at different process parameter ranges. Due to the high temperature gradient in SLM process, the thermal material properties such as thermal conductivity and specific heat vary significantly. Therefore, the thermal material properties of the Ti-6Al-4V are considered to be temperature dependent as listed in Table 1. Also, during the SLM process, the part undergoes cyclic melting and solidification process, this is considered in the modeling by modifying the heat capacity using latent heat of melting. Moreover, the deposition of the metallic powders layer by layer could change the thermodynamic and heat transfer mechanisms. Consequently, it is important to consider the layering addition in the modeling of the temperature field.

Figure 20 illustrates the predicted melt pool depth and width for the laser power of 20 W and the scan speed of 200mm/s. The laser spot radius is 26 μm and the layer thickness is 30 μm, same as the experimental procedure. Moreover, the absorption ratio is 0.77. The predicted melt pool depth and width with uniform moving heat source are overestimated when compared to experimental measurements. The main reason is that the geometry of the uniform heat source is more like a rectangle shape as shown in Figure 21. However,

the actual melt pool geometry from the experiment has a circular and elliptical shape in most of the cases. Figure 22 is the same plot as Figure 21, but the transient uniform heat source is omitted from the plot to better illustrate the comparison of the predicted and measured melt pool depth and width for steady state point heat source (HS), transient double elliptical HS, transient point HS, and transient semi-elliptical HS.

The predicted melt pool depth is accurately predicted with steady state point HS model and transient semi-elliptical heat source. Transient double elliptical heat source has predicted the melt pool depth with 12.5% error. Moreover, the transient point heat source model has predicted the melt pool depth with 50% error. The reason for a high amount of error in transient heat source model is that the predicted melt pool geometry is varying with time. Since this is a transient model, due to the passing of time more heat would be conducted through the solid which would result in lower melt pool geometry prediction. It should be noted that the point heat source approach is usually used for surface laser treatment processes such as laser hardening and laser conductive melting. Also, it is good to represent the absorption of laser radiation in metal surface. Consequently, at different time steps the melt pool geometry would vary slightly. In this paper, in order to be consistent in the modeling, the predicted melt pool geometry is obtained immediately after the radiation of the laser.

The melt pool width is also predicted for all five heat source models. The uniform heat source model is predicted for all the selected process parameters in Table 7. As explained before, the transient uniform HS could not predict the melt pool geometry with a reasonable range of error. Since the predicted melt pool geometry using this heat source geometry is way higher than the experimental measurements, the results are not shown in this paper.

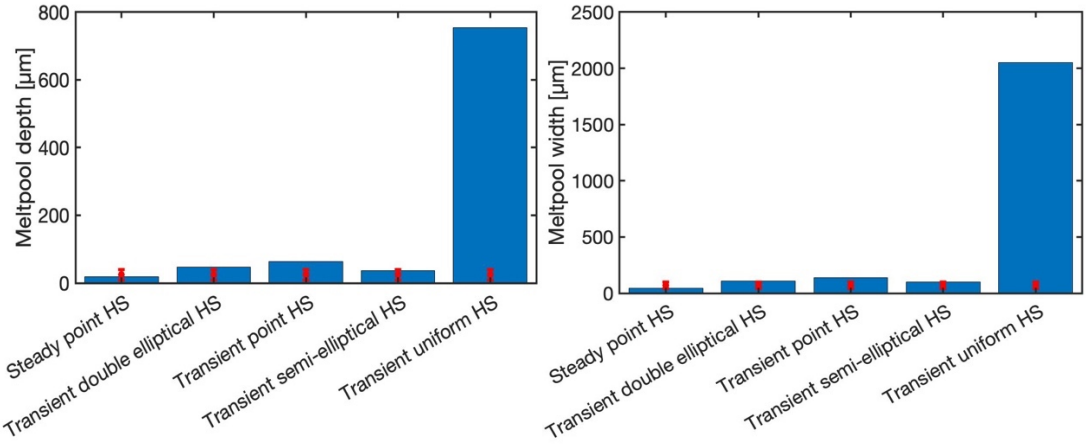

(a) (b)

Figure 20. Predicted melt pool geometry with the laser power of 20 W and scan speed of 200 mm/s (a) melt pool depth, (b) melt pool width (Sample 1 in Table 7)

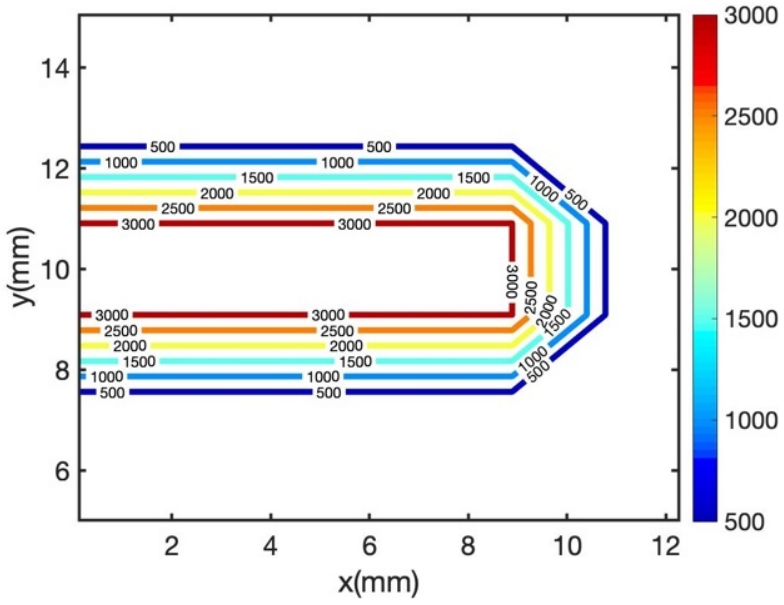

Figure 21. Illustration of the melt pool geometry using uniform moving heat source.

The melt pool width is captured by steady-state moving HS, transient double elliptical HS, transient point HS, and transient semi-elliptical HS with the maximum error of 0%, 10%, 37%, 0%, respectively.

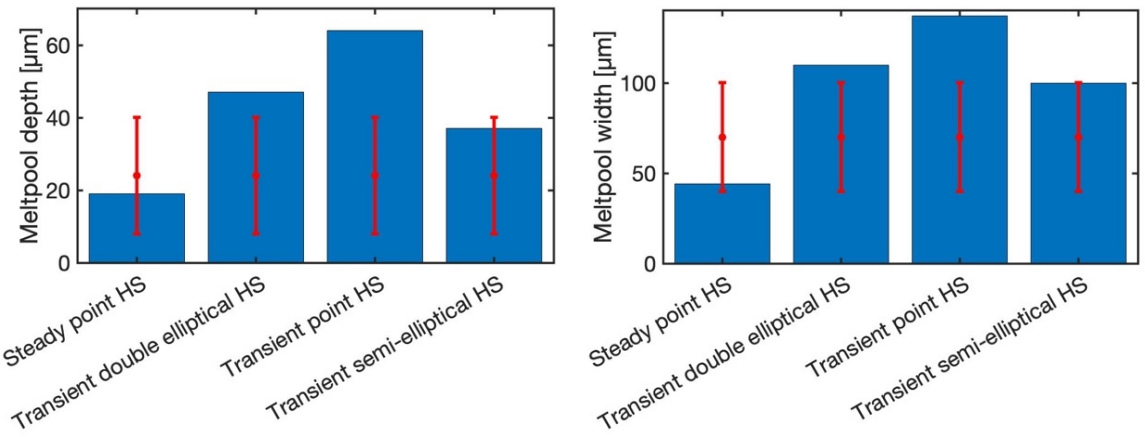

(a) (b)

Figure 22. Predicted melt pool geometry with the laser power of 20 W and scan speed of 200 mm/s (a) melt pool depth, (b) melt pool width (Sample 1 in Table 7)

Predicted melt pool geometry using steady state point HS, transient double elliptical HS, transient point HS, and transient semi-elliptical HS for all the 8 samples are listed in Table 8.

Table 8. Predicted melt pool geometry for 8 different samples.

Sample	Steady state moving point HS		Transient moving point HS		Semi-elliptical HS		Double-elliptical HS		Experiment	
	Depth (μm)	Width (μm)	Depth (μm)	Width (μm)	Depth (μm)	Width (μm)	Depth (μm)	Width (μm)	Depth (μm)	Width (μm)
1	19	44	64	137	37	100	47	110	24-40[82]	70-100[82]
2	33	90	89	187	46	130	68	127	37-50[82]	80-120[82]
3	71	105	95	193	68	150	78	145	50-80[82]	110-170[82]
4	72	145	100	150	94	160	111	155	85-110[82]	140-160[82]
5	727	--	786	--	1095	--	1252	--	700-1300[83]	--
6	67	162	241	340	156	310	227	290	190-280[84]	250-300[84]
7	67	162	222	340	156	310	168	245	150-250[84]	185-225[84]

Table 8 continued.

8	67	162	206	340	156	310	150	197	110-210[84]	150-200[84]

4.1.3 Region of Applicability of Each Model Based on Laser Power and Scan Speed

Figure 23 illustrates the predicted melt pool depth and width using steady-state moving point heat source approach for different laser power and scan speed as listed in Table.7. The material for all the samples is Ti-6Al-4V. Sample 1 through sample 4 are fabricated using the laser power of 20 W, 40 W, 60 W and 80 W with the fixed scan speed of 200 mm/s. As shown in this figure, the predicted melt pool depth and width using steady state moving point heat source approach are within the range of experimental measurements. Sample 5 is built using laser power of 500 W and the scan speed of 6 mm/s. The predicted melt pool depth is within the range of experimental measurement. The melt pool width for this sample is not reported in the literature. Sample 6 through sample 8 are built using a fixed laser power of 300 W with the scan speed of 400mm/s, 800mm/s, and 1200 mm/s, respectively. The predicted melt pool depth and width for these three samples are equal. The predicted melt pool depth is 67 μm, and predicted melt pool width is 162 μm. This shows that the steady state moving point heat source approach does not have the ability to predict the temperature field for high laser speeds. This is because of the behavior of the exponential term. As the power value (laser speed) of the exponential term increase, the output of the function will be less sensitive to the power value. Consequently, in these cases where the magnitude of the scan speed is high, the temperature field does not change.

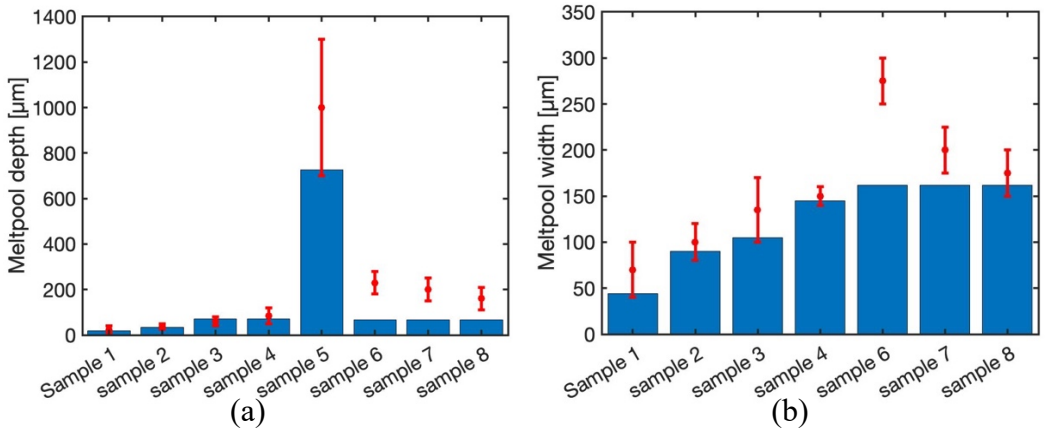

Figure 23. Predicted melt pool (a) depth and (b) width using steady state moving heat source.

Figure 24 demonstrates the predicted melt pool geometry using the semi-elliptical heat source model. Predicted melt pool width for the first four samples are within the range of experimental measurements. The melt pool width and depth do not change for the samples 6 through 8. The main reason could be the effect of heat source geometry. As explained by Goldak et al. [65] the heat source parameters should be calibrated using experimental data. Since the goal of this work is the comparison of the heat source models, the authors tried to be consistent in the modeling and comparison. So, the same calibration based on experimental data is used for all the samples and models.

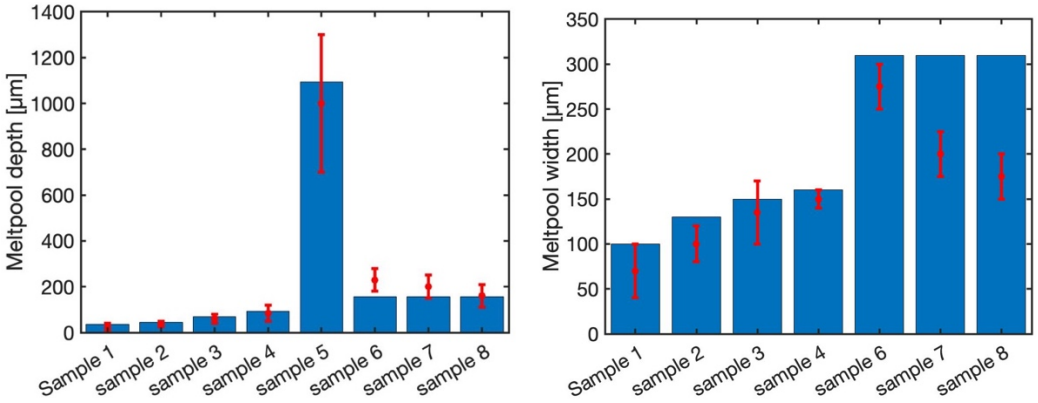

Figure 24. Predicted melt pool (a) depth and (b) width using semi-elliptical moving HS.

Figure 25 demonstrates the predicted melt pool depth and width for 8 samples using double elliptical moving heat source approach. The predicted melt pool depth and width for all the samples are within the range of experimental measurements. This shows that the double elliptical moving heat source could be used for all the range of laser powers and scan speeds. The main reason is that the actual melt pool geometry from the experimentation resembles the ellipsoidal shape. Consequently, the double elliptical moving heat source could simulate the melt pool geometry quite well.

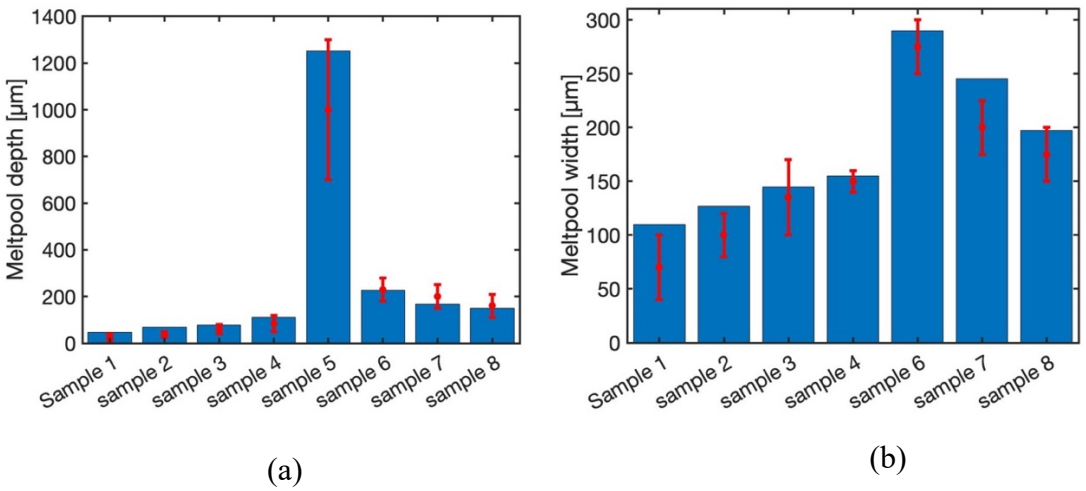

Figure 25. Predicted melt pool (a) depth and (b) width using double elliptical moving HS.

Figure 26 depicts the melt pool depth and width using transient moving point heat source approach. The melt pool depth is well captured using this approach for all the samples. Moreover, predicted melt pool width for the first four samples (sample 1 through 4) are predicted with the maximum error of 15%. The predicted melt pool width for sample 6 through 8 does not change. This is due to the existence of the exponential term in the modeling of the temperature field using transient moving heat source approach, as explained before. As a result, the transient moving point heat source approach could not be used for the prediction of the temperature field at high speeds.

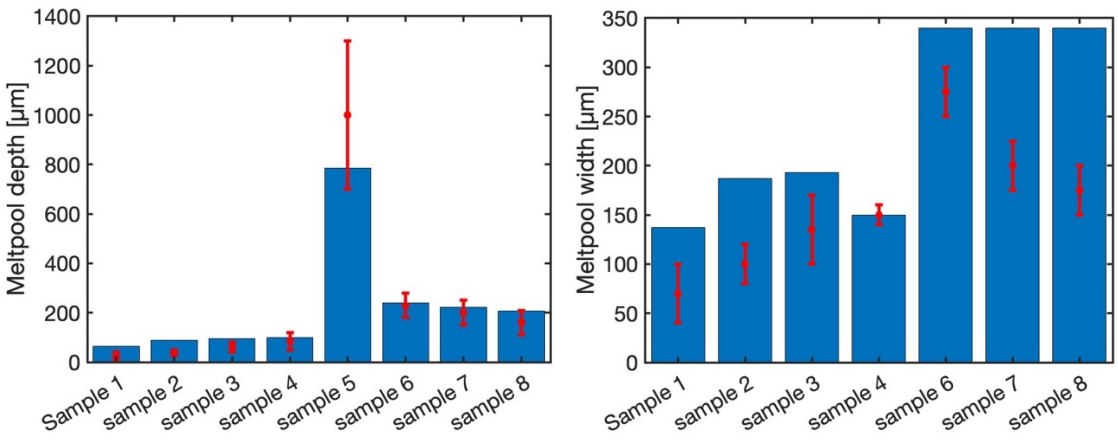

Figure 26. Predicted melt pool (a) depth and (b) width using transient moving point HS.

4.2 Thermal Stress Prediction and Validation

To evaluate the proposed elastoplastic analytical model, a comparison between the predicted and simulated von Misses stress and total strain is performed. For consistency with FEM, the same size part is modeled in the analytical model.

During the heating process, the heated material tends to expand, however, the thermal expansion is restrained by the surrounding materials with lower temperature. Thus, a compressive stress state is formed in the heated zone. During the cooling stage when the heat source passed the study point, the previously formed heated zone begins to cool down and shrinkage of material in this zone tend to occur. The generated bump in the FEM simulation at the location of the laser is an exaggeration of the expansion and shrinkage of the build part during the heating and cooling process.

In finite element modeling, a transient temperature model is used to simulate the temperature profile during AM process. The predicted temperature is then couple to the static structure to simulate the thermal stress. In most of the case studies, the obtained thermal stress is at almost end of the track, also in one of the cases, the thermal stress is obtained at the middle of the track. To be consistent, the analytical model predicts the thermal stress at the same location as FEM does. This has been done to show that the proposed analytical model can predict the thermal stress at every location in the medium.

Five different combinations of laser power and scan speed are selected as listed in Table 9. As explained in the previous chapters, not all the laser powers and scan speeds result in melting of the metallic powders in FEM. Different combinations of process parameters are tried to fully melt the metallic powders. For example, the powders were melted with the laser power of 220 W, and a scan speed of 30 mm/s. However, with the laser power of 220

W and a scan speed of 50 mm/s the powders were not melted. The reason is that for given laser power, the increase in scan speed causes the material to have less time to absorb the energy. Consequently, for this case, the combination of the process parameters was not enough to melt the powders.

Table 9. List of selected process parameters.

Case studies	Laser Power (W)	Scan speed (mm/s)
1	220	30
2	440	50
3	440	30
4	660	50
5	660	30

A comparison of the results between the predicted and simulated von Misses stress and total strain are shown in Figures 27 through 31 and Figures 32 through 4.37 respectively.

Figures 27(a), 28(a), 29(a), 30(a), and 31(a) are the plots of the von Mises stress from the proposed analytical elastoplastic thermal stress analysis, and figures 27(b), 28(b), 29(b), 30(b), 31(b) are the plots of the von Mises stress from the elastoplastic FEM. Since the build part goes through phase transformation twice, the yield stress near the melt temperature is influential.

Prediction of the maximum and also the distribution of the von Mises stress is important for the determination of the yielding and fracture of the material, and then can be used as a process mechanic attribute to optimize the process parameters to increase the life of the components. For Ti-6Al-4V, the yield stress near the melting temperature is almost zero which causes severe plastic deformation and relatively low final strength. In the elastoplastic hardening model, when the stress exceeds the yield strength, the build part deforms plastically. After the yield point, the strain would increase with faster rate compare to the stress.

Figures 27(a and b) show the predicted von Mises stress from analytical modeling and FEM. As it is illustrated in figure 27(a), the maximum von Mises stress occurs at the location of the laser. The maximum predicted stress for the first case study with the laser power of 220 W and a scan speed of 30 mm/s is around 200 MPa. The maximum obtained von Mises stress from FEM is 208.97. The obtained error between predicted von Mises stress from the proposed model and FE simulation is less than +4.3%.

Figure 28(a and b) illustrates the predicted and simulated on von Mises stress for the laser power of 440 W and 50 mm/s. The maximum predicted stress from analytical modeling is

around 300 MPa and the obtained stress from the FEM is 332 MPa. The obtained error, in this case, is less than +9.6%.

The maximum predicted stress from elastoplastic analytical modeling for the laser power of 440 W and a scan speed of 30mm/s is 350 MPa, and the predicted stress from FEM is 340.96 MPa, as illustrated in Figure 29(a and b). The obtained error between predicted stress from analytical modeling and simulated stress from FE modeling is less than −2.7%.

For the fourth case study with the laser power of 660 W and 50 mm/s the predicted stress is around 450 MPa, and the simulated stress is 405.95 MPa, as depicted in Figure 30(a and b). The obtained error between predicted and simulated stress is −9.7%.

For the last case study with the laser power of 660 W and a scan speed of 30 mm/s, as shown in Figure 31(a and b), the predicted stress is 500 MPa, and the simulated stress is 460.18. The obtained error for this case is −8.6%. Good agreement has been achieved between the proposed elastoplastic thermal stress analysis and the simulated thermomechanical model.

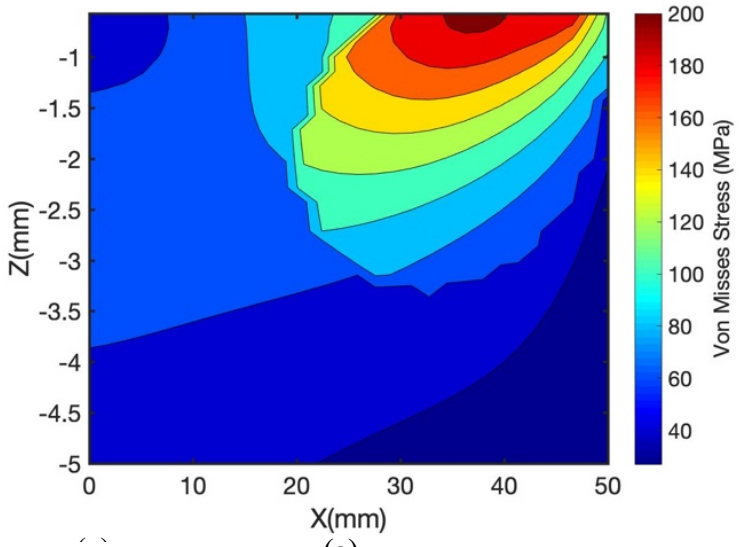

(a)

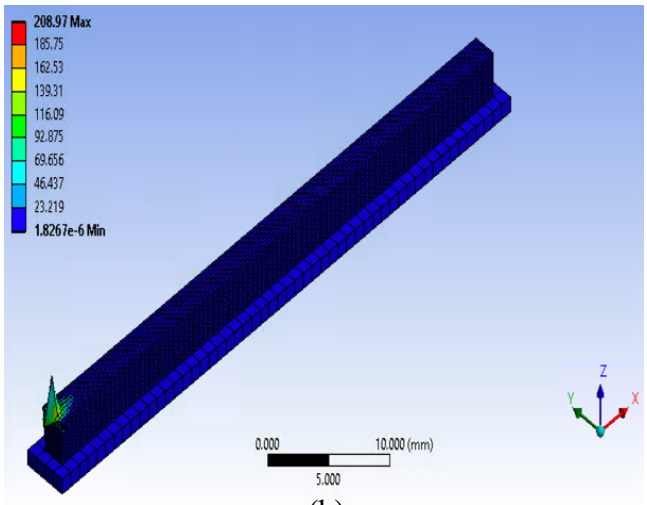

(b)

Figure 27. Predicted and simulated stress using (a) analytical modeling and (b) FEM for the laser power of 220 W, scan speed of 30 mm/s, and absorptivity of 80%.

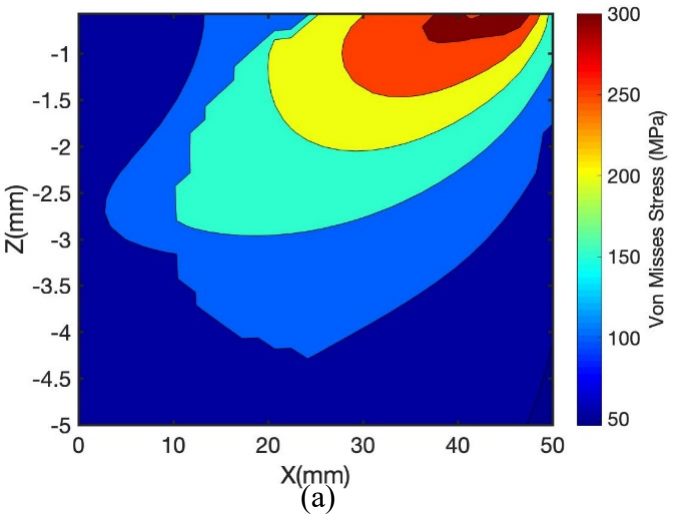

(a)

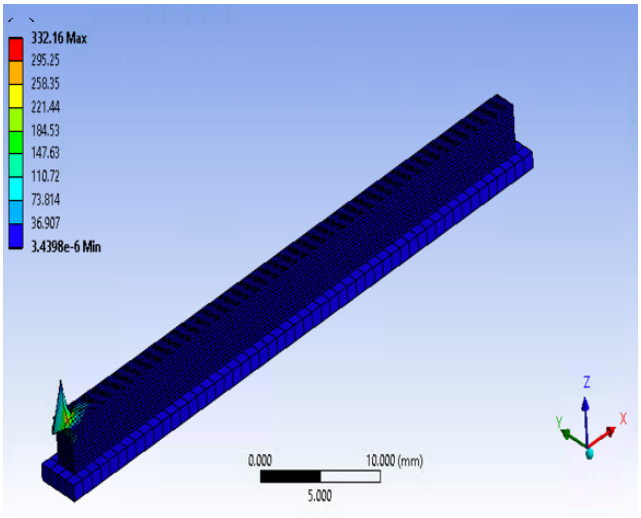

(b)

Figure 28. Predicted and simulated stress using (a) analytical modeling and (b) FEM for the laser power of 440 W, scan speed of 50 mm/s, and absorptivity of 80%.

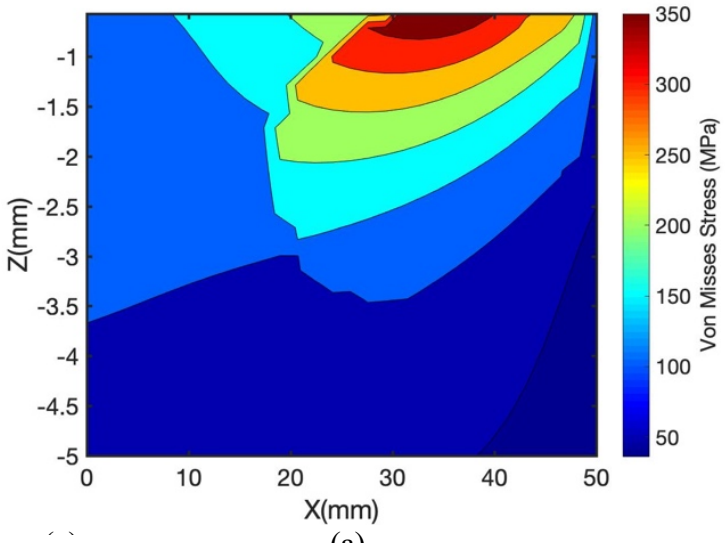

(a)

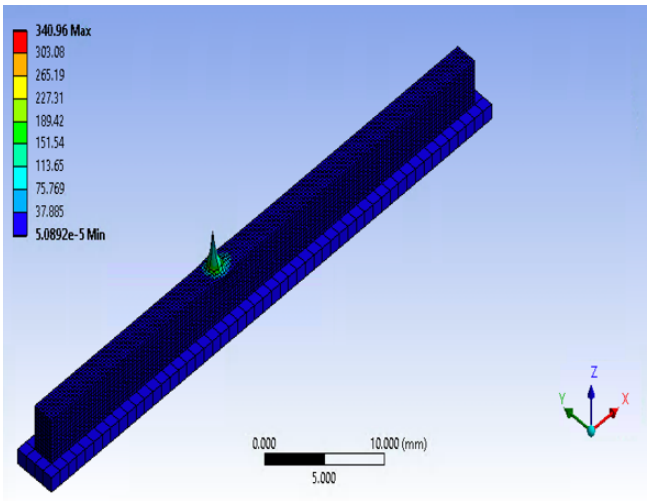

(b)

Figure 29. Predicted and simulated stress using (a) analytical modeling and (b) FEM for the laser power of 440 W, scan speed of 30 mm/s, and absorptivity of 80%.

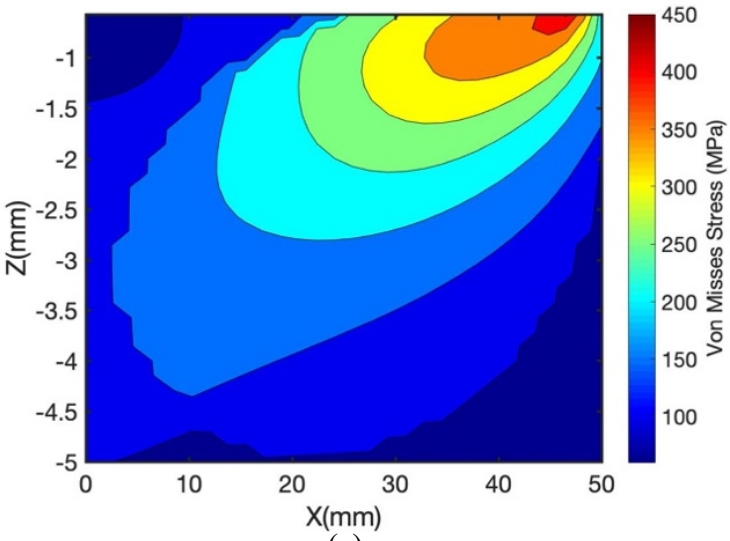

(a)

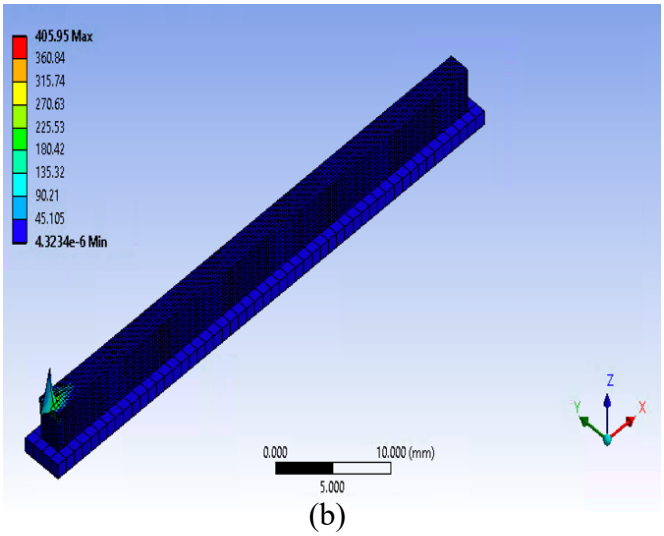

(b)

Figure 30. Predicted and simulated stress using (a) analytical modeling and (b) FEM for the laser power of 660 W, scan speed of 50 mm/s, and absorptivity of 80%.

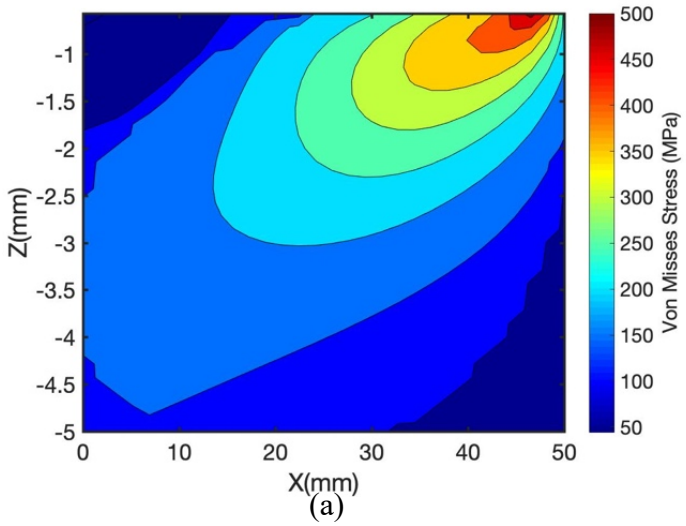

(a)

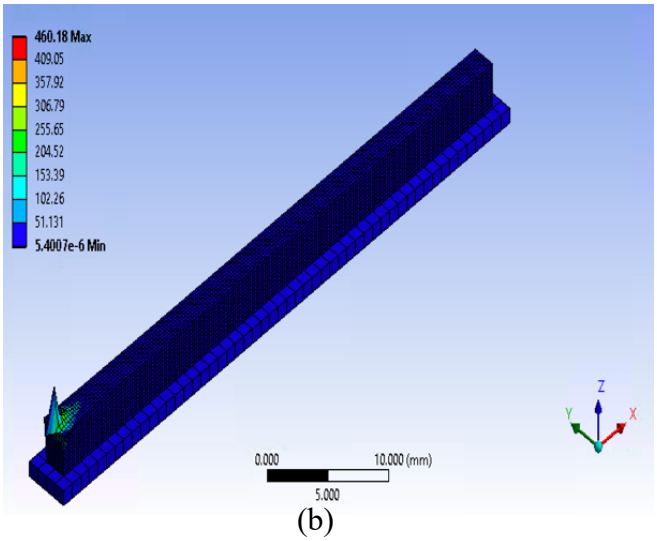

(b)

Figure 31. Predicted and simulated stress using (a) analytical modeling and (b) FEM for the laser power of 660 W, scan speed of 30 mm/s, and absorptivity of 80%.

Figures 32(a and b) illustrate the obtained total strain from elastoplastic analytical model and FEM for the laser power of 220 W and a scan speed of 30 mm/s. The predicted total strain from the analytical model is 0.018 mm/mm and the obtained strain from FEM is 0.018 mm/mm. The accuracy of the proposed elastoplastic analytical model is verified through obtaining same performance as FEM.

For the laser power of 440 W and a scan speed of 50 mm/s, as illustrated in Figure 33(a and b), the predicted total strain from analytical and FEM is 0.020 mm/mm and 0.021 mm/mm, respectively. The error between predicted and simulated total strain is less than +4.8%.

Figures 34(a and b) is an illustration of the total strain for the laser power of 440W and a scan speed of 30 mm/s. The predicted total strain from the analytical model is 0.035 mm/mm and the obtained total strain from the FEM is 0.033 mm/mm. The error between the proposed analytical model and FEM is around −6%.

For the laser power of 660 W and a scan speed of 50 mm/s, as depicted in Figures 35(a and b), the predicted total strain from analytical and simulated is 0.05 mm/mm and 0.048 mm/mm, respectively. The obtained error for this case study is less than −4.2%.

For the last case study with the laser power of 660 W and scan speed of 30 mm/s the obtained total strain from analytical and FEM is 0.06 and 0.056, as shown in Figures 36(a and b). The obtained error, in this case, is −7.1%.

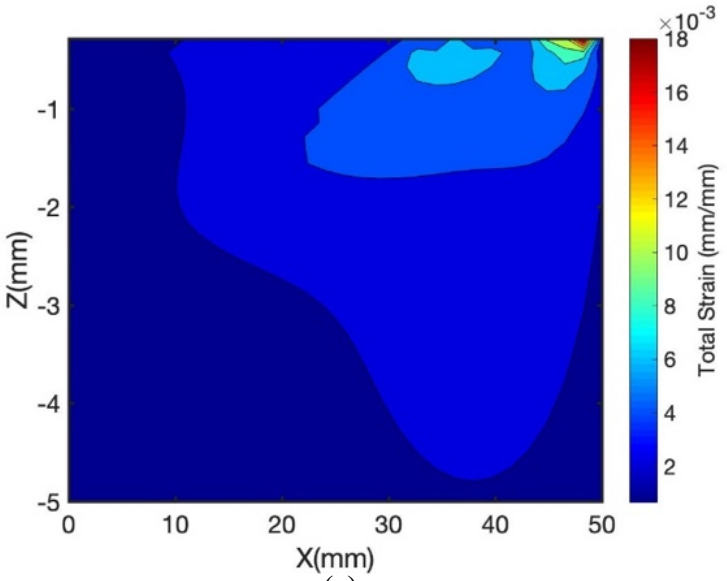

(a)

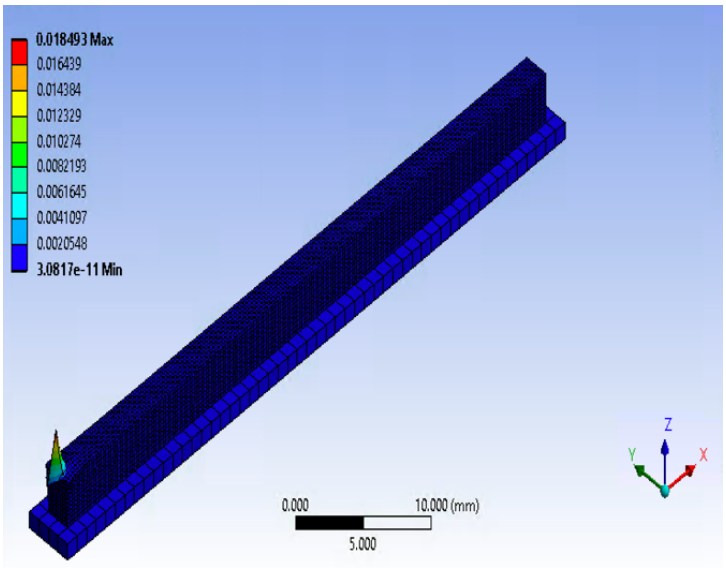

(b)

Figure 32. Predicted and simulated total strain using (a) analytical modeling and (b) FEM for the laser power of 220 W, scan speed of 30 mm/s, and absorptivity of 80%.

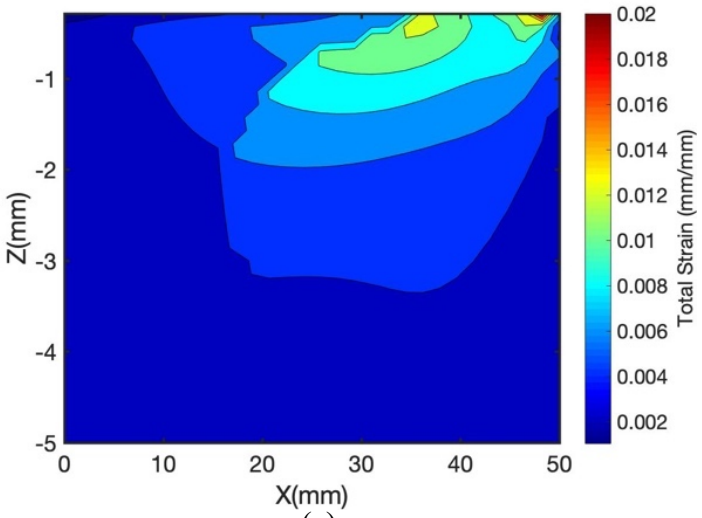

(a)

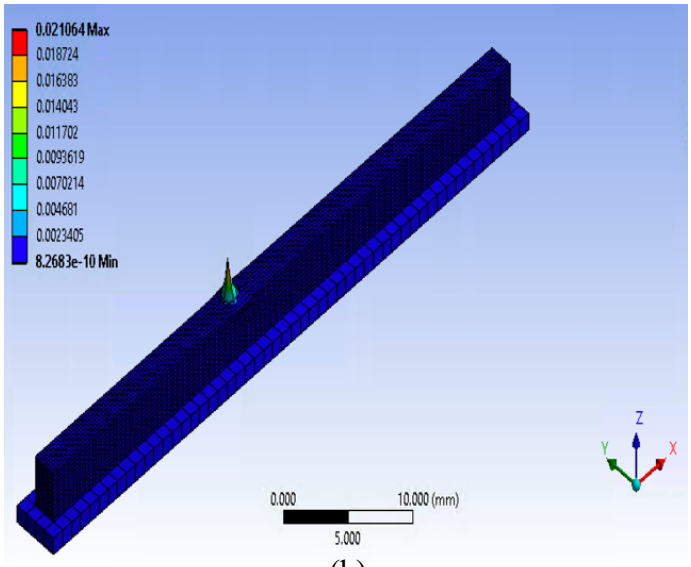

(b)

Figure 33. Predicted and simulated total strain using (a) analytical modeling and (b) FEM for the laser power of 440 W, scan speed of 50 mm/s, and absorptivity of 80%.

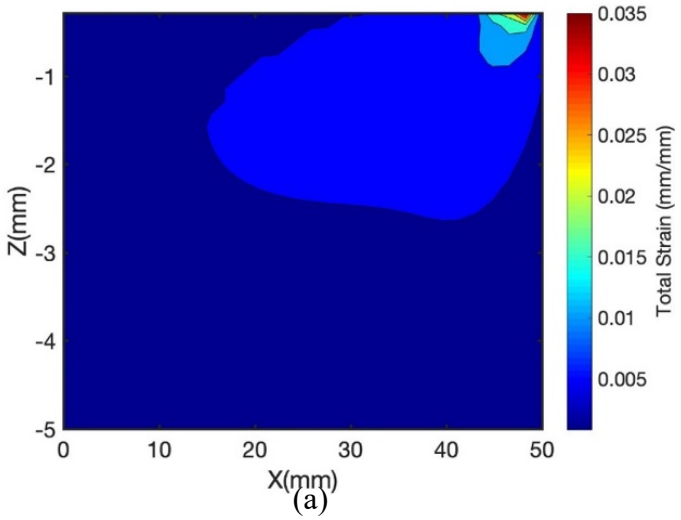

(a)

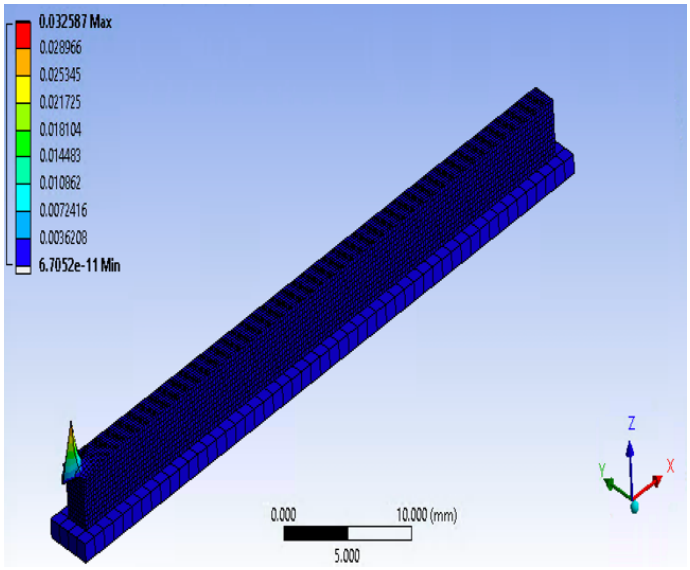

(b)

Figure 34. Predicted and simulated total strain using (a) analytical modeling and (b) FEM for the laser power of 440 W, scan speed of 30 mm/s, and absorptivity of 80%.

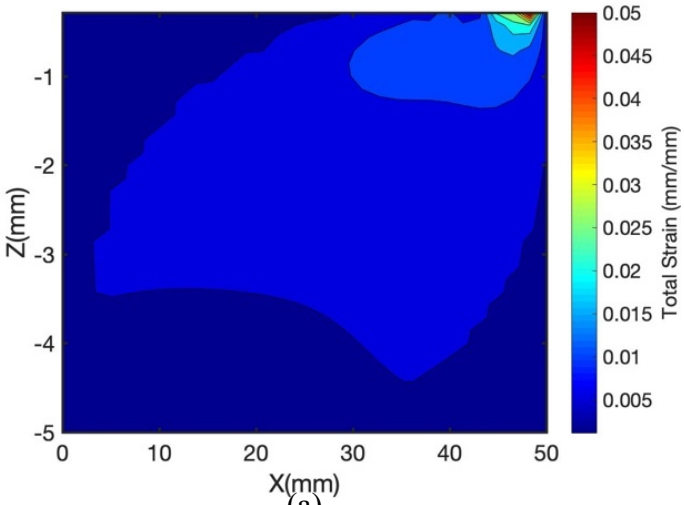

(a)

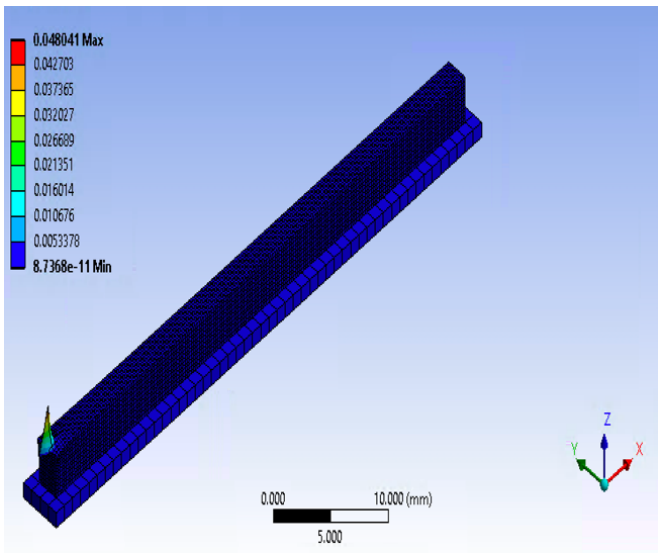

(b)

Figure 35. Predicted and simulated total strain using (a) analytical modeling and (b) FEM for the laser power of 660 W, scan speed of 50 mm/s, and absorptivity of 80%.

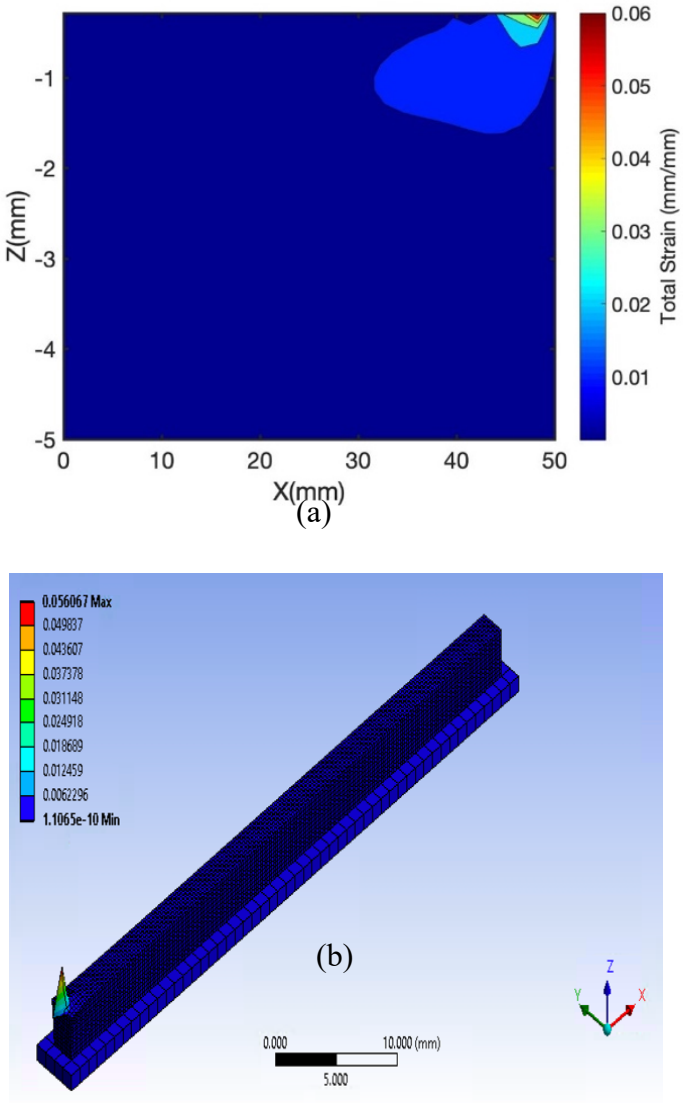

Figure 36. Predicted and simulated total strain using (a) analytical modeling and (b) FEM for the laser power of 660 W, scan speed of 30 mm/s, and absorptivity of 80%.

As shown in Figures 37 and 38, for given scan speed, the increased in power would increase the stress and strain. The reason is that higher laser power would increase the maximum temperature absorbed by the metallic powders, resulting in a higher temperature gradient.

Consequently, the higher stress and strain would build-up in the part during the AM process.

Also, for given laser power, the decrease in scan speed would increase the stress and strain. This is due to the fact that the build part has more time to absorb the energy induced by the laser. As a result of the higher temperature gradient, the stress and strain increase in the build part.

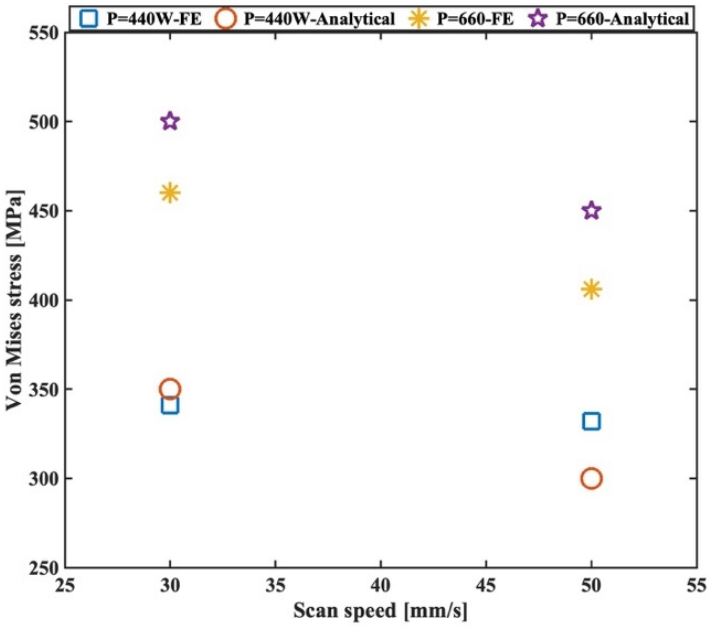

Figure 37. Comparison of the von Mises stress between proposed analytical model and FEM.

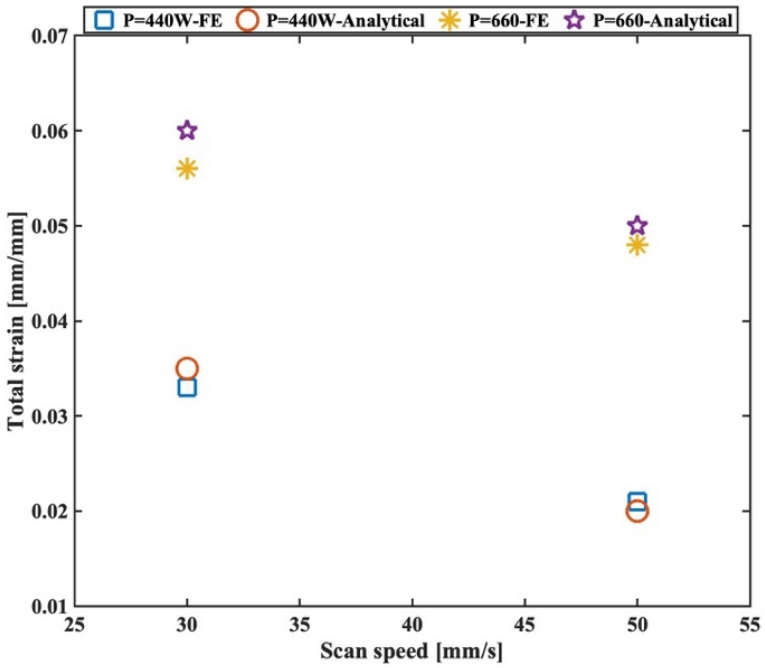

Figure 38. Comparison of the total strain between proposed analytical model and FEM.

4.2.1 Impact of AM Variables on Stress/Strain

To investigate the effects of laser power, scan speed, and absorptivity on elastoplastic thermal stress and strain analysis, a few parameter studies are performed using the proposed analytical model. The first study looked at the effect of laser power and scan speed. Five different laser powers and five different scan speeds are selected. The selected laser powers are 300 W, 440W,500 W, 660 W and 800 W. Also, the selected scan speeds are 30 mm/s, 50 mm/s, 70 mm/s, 90 mm/s and 110 mm/s. The absorptivity is 0.8. As shown in Figure 39 and Figure 40, for given scan speed, the increase in laser power would increase the stress and strain. The main reason is that the increase in laser power would increase the temperature gradient. Consequently, the stress and strain would increase. Moreover, for

given laser power, the decrease in scan speed would increase the temperature and temperature gradient since the build has more time to absorb the energy. This would increase the stress build- in the additively manufactured part.

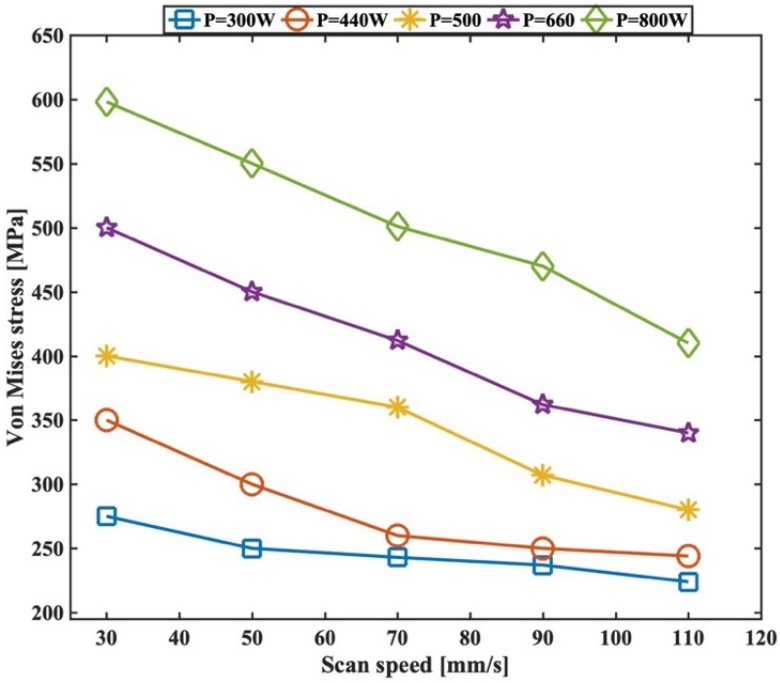

Figure 39. Effect of laser power and scan speed on stress.

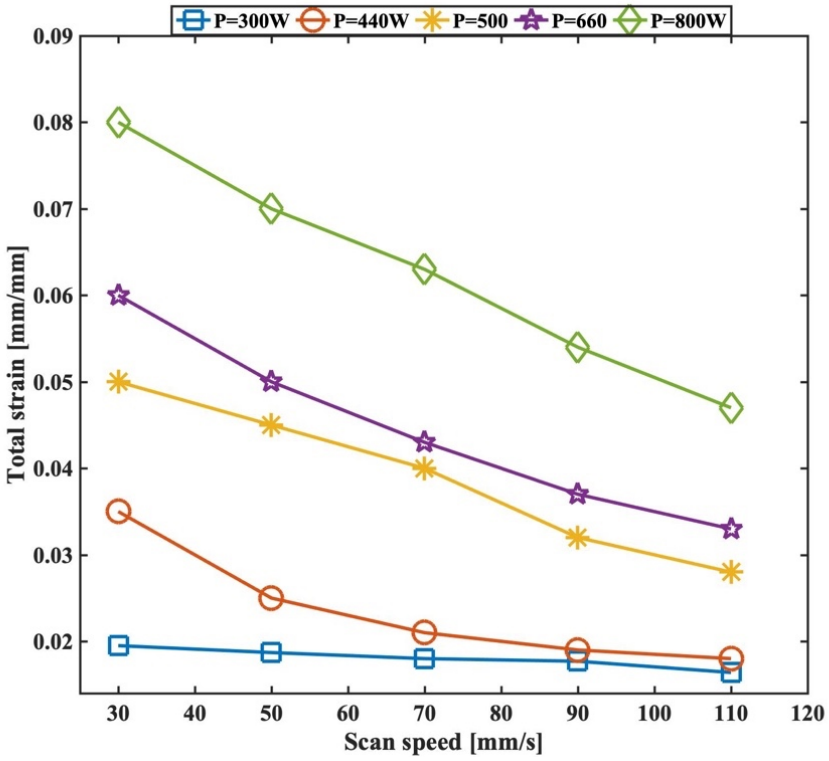

Figure 40. Effect of laser power and scan speed on total strain.

Effect of absorptivity is also studied in this work as shown in Figure 41 and Figure 42. The absorption ratio determines the amount of energy that the part can absorb. The absorptivity is a function of material, laser power, and scan speed. For the laser power of 800 W and a scan speed of 30 mm/s, the increase in absorption ratio would increase the surface temperature and as a result, it increases the temperature gradient. Thus, the stress and strain in the build part would increase as a result of an increase in absorption ratio as depicted in Figure 41 and Figure 42. Moreover, as the absorptivity increases the stress increases slowly at the lower absorptivity ranges (below 40% absorptivity) and rapidly at the higher absorptivity ranges. The same trend is observed for total strain, however, the rapid change in total strain is observed at 80% absorptivity.

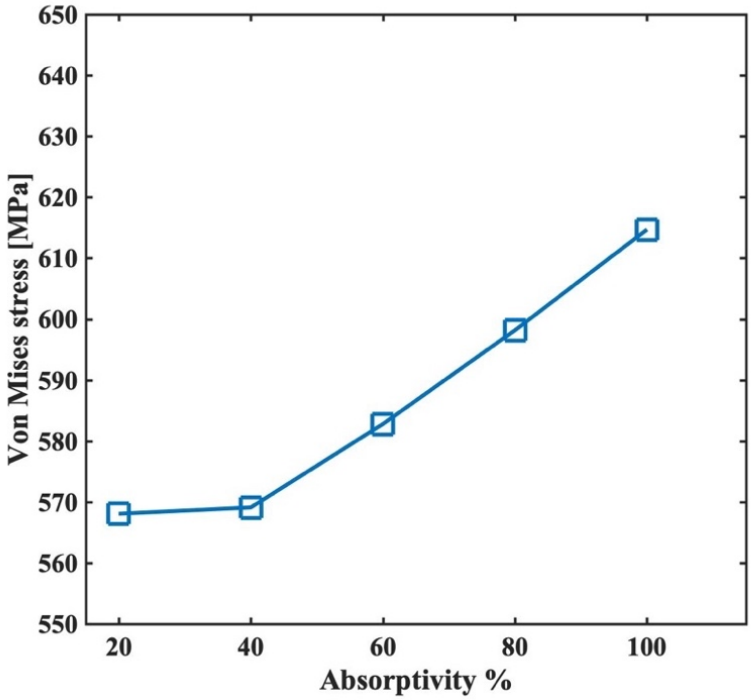

Figure 41. Effect of absorptivity on stress for the laser power of 800 W and scan speed of 30 mm/s.

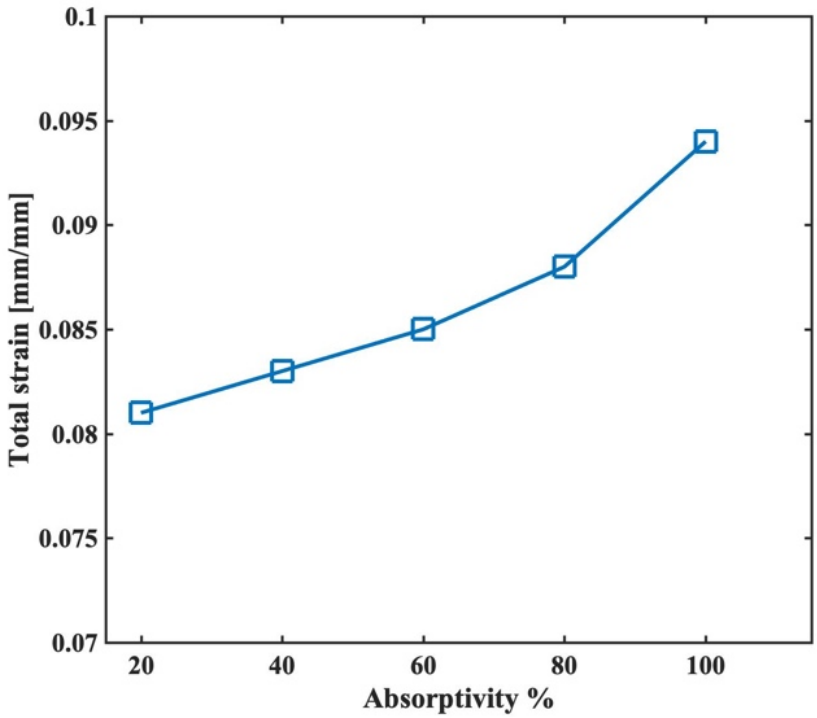

Figure 42. Effect of absorptivity on total strain for the laser power of 800 W and scan speed of 30 mm/s.

4.3 Residual Stress Prediction and Validation

Metal additive manufacturing (AM) process induces residual stress which can hinder the applicability of AM. Residual stress build-up causes part failure due to the crack initiation and growth, and also distortion during or after fabrication. Consequently, it is of great importance to accurately and rapidly predict the residual stress within the AM parts.

Due to the high-temperature gradient innate in this process, material may experience high thermal stress which often exceeds the yield strength of the material. The thermal stress is obtained from Green's functions of stresses due to the point body load as explained in chapter 3. Then, as a result of the cyclic heating and cooling and the fact that the material

is yielded, the residual stress build-up is precited from incremental plasticity and kinematic hardening behavior of the metal according to the property of volume invariance in plastic deformation in coupling with the equilibrium and compatibility conditions. Results from the analytical residual stress model are compared to the experimental measurement of residual stress conducted via X-ray diffraction. The components are built via laser powder bed fusion and powder bed system for various material systems of Ti-6Al-4V, IN718, and Maraging Steel 350 under different process conditions.

In the next sections, first the procedure of the residual stress measurements for each type of material is explained and then compared to analytical predictions.

4.3.1 Residual Stress Measurement of IN718 Built via DMD Process

Three blocks of IN718 specimens with the size of 20 x 10 x 3mm are manufactured via DMD process using LENS CS 1500 SYSTEMS with the laser wavelength of 1070 nm, under different process conditions as listed in Table 10. Density of the additively manufactured part has a substantial influence on mechanical properties of the fabricated part. Based on the given machine and powder size parameters, an approach to identify processing parameters for producing high-density parts is employed to select the processing conditions as described in the previous studies [85-88]. The processing conditions used to fabricate high-density samples for measuring the residual stress are listed in Table 10. The selected laser powers are 920 W, 743 W, 485 W, and the scan speeds are 25 mm/s, 40 mm/s, 40 mm/s, respectively. The laser power has three levels, and the scan speed has two levels. The main reason for the selection of these process parameters is to investigate the effect of process parameters such as scan speed and laser power on

residual stress while other parameters such as layer height, hatching space, and scan path are kept the same. The deposited layer thickness for all the samples is 250 μm, and hatch spacing is 105 μm. A bi-directional continuous scan path is used.

Table 10. Process parameters for DMD of IN718 specimens.

laser power(W)	**Powder feed (*gram/s*)**	**Scan speed (*mm/s*)**	**layer height (μm)**	**Hatch spacing (μm)**	**Scan Pattern**	**VED J/mm^3**
485	1	40	250	105	Bi-directional	9.7
743	0.5	40	250	105	Bi-directional	14.86
920	1	25	250	105	Bi-directional	29.44

X-ray diffraction (XRD) technique (PANalytical Empyrean multipurpose X-ray diffractometer equipped with $Cu - K\alpha$ radiation) is used to measure the residual stress of the specimens using the $sin^2\Psi$ method [89, 90]. For each point through thickness the through thickness residual stress is measured two times and the results were averaged. The parameters for XRD measurement are specified in Table 11.

Table 11. XRD parameters used for residual stress measurements.

Focus	1.0 mm
Radiation	Cu Kα
Lattice plane (hkl) [90]	{420}
2Ɵ [90]	145 º
Ψ-tilting	0º to 45º in 6 steps each
Young modulus [91]	199,955 MPa
Poisson ration [91]	0.29

The residual strains are determined as;

$$\varepsilon = \frac{d-d_0}{d_0} \tag{4.1}$$

where, d and d_0 are the stressed and unstressed lattice parameter, respectively.

The generalized Hook's law for isotropic material is used to calculate stress as

$$\sigma_i = \frac{E}{(1+\upsilon)(1-2\upsilon)}((1-\upsilon)\varepsilon_i + \upsilon(\varepsilon_j + \varepsilon_k) \text{ where } i,j,k \in x,y,z. \tag{4.2}$$

In Equation (4.2), an elastic modulus (E), and Poisson's ratio of 199,955 MPa and 0.29 are used, respectively. Samples are polished using liquid abrasive of 1 μm and 0.05 μm at a very slow speed to eliminate macroscopic residual stresses. Measurements are collected every 0.5 mm along the build direction (z-axis) of the samples.

4.3.2 Residual Stress Measurement of Ti-6Al-4V Built via DMD Process

Two blocks of Ti-6Al-4V specimens with the size of 20×10×3 mm is produced via DMD process using LENS CS 1500 SYSTEMS under different process conditions as shown in Table 12. The selected laser powers are 206 W, and 385 W, and the scan speeds are 25 mm/s, 40 mm/s, respectively. The deposited layer thickness for both samples is 250 μm, and hatch spacing is 105 μm. A bi-directional continuous scan strategy is used to build the parts.

Table 12. Process parameters for DMD of Ti-6Al-4V specimens.

laser power (W)	**Scan speed (*mm/s*)**	**Feed rate (gram/s)**	**layer height (μm)**	**Hatch spacing (μm)**
206	25	1	250	105
385	40	0.5	250	105

Same procedure as previous section is used to measure the residual stress using the $sin^2\Psi$ method.

In Equation (4.2), an elastic modulus (E), and Poisson's ratio of 114 GPa and 0.33 are used, respectively. Samples are polished using liquid abrasive of 1 μm and 0.05 μm at a very slow speed to eliminate macroscopic residual stresses. Measurements are collected every 0.5 mm along the build direction (z-axis) of the samples.

4.3.3 Residual Stress Measurement of IN718 Built via L-PBF Process

Density of the additively manufactured component is the fundamental property that has a profound impact on mechanical properties of the fabricated component [92]. Based on the given machine and powder size parameters as listed in Table 13, the approach to identify processing parameters for producing high-density parts was employed to select the processing conditions as described in our previous studies [85-88]. The processing conditions used to fabricate high-density samples for measuring the residual stress are listed in Table 14. In these fabricated samples, the scan strategy of hatching space, layer thickness, number of scans, and scan pattern are the same. For each set of parameters specified in Table 14, there were three samples fabricated by a commercial Tong Tai AM250 SLM machine. The manufacturing process was carried out in the chamber filled with nitrogen gas and the oxygen concentration was controlled under 2000 ppm for preventing the oxidation of metal powder. Figure 43 shows the as-build samples and were then removed from the base plate using the electrical discharge machining (EDM).

Table 13. Powder and machine parameters.

Powder material	Inconel 718 (IN 718)
Powder size distribution	d_{10} = 17.51 µm ; d_{50}= 31.44 µm; d_{90}= 52.21 µm
Range of laser power (P)	50 ~ 400 W
Range of scanning speed (v)	100 ~ 2000 mm/s
Laser spot size	D4sigma = 54 µm
Laser type	Nd: YAG laser

Table 14. Process parameters used to fabricate IN718 specimens via L-PBF

No.	Laser power (W)	Scanning speed (mm/s)	Powder layer thickness (µm)	Hatching space (µm)	Number of scans	Scan pattern	Pre-heating (˚C)	Rotation angle of scan vector between layers (˚)
1	150	600	30	100	50	Zigzig	No	67
2	250	600	30	100	50	Zigzig	No	67
3	150	1000	30	100	50	Zigzig	No	67

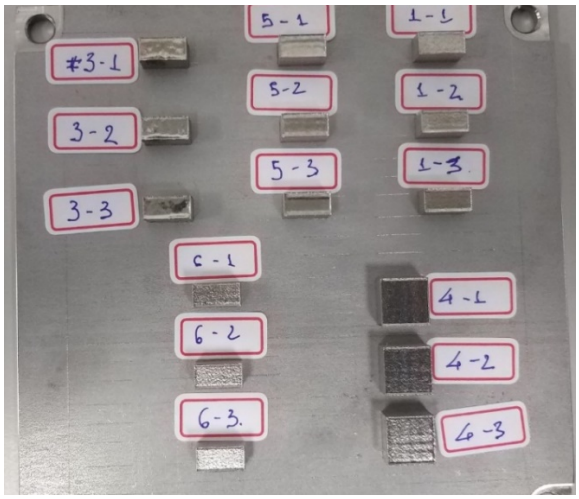

Figure 43. Illustration of the as-build IN718 parts manufactured via L-PBF.

The residual stress on the side walls of the samples, as illustrated in Figure 4.37, was measured by a commercial X-ray Diffraction machine (D8 Discover Bruker) using the $sin^2\Psi$ method [89, 90]. The coordinate and location of measured points are shown in Table 15. For each point shown in Figure 44, the through-thickness residual stresses along the build direction (z direction), and along the scan direction (x direction) were measured. The parameters for XRD measurement are specified in Table 16. It is noted that for each set of parameters and each point shown in Figure 44, the XRD measurements were performed on three fabricated samples and the results were averaged.

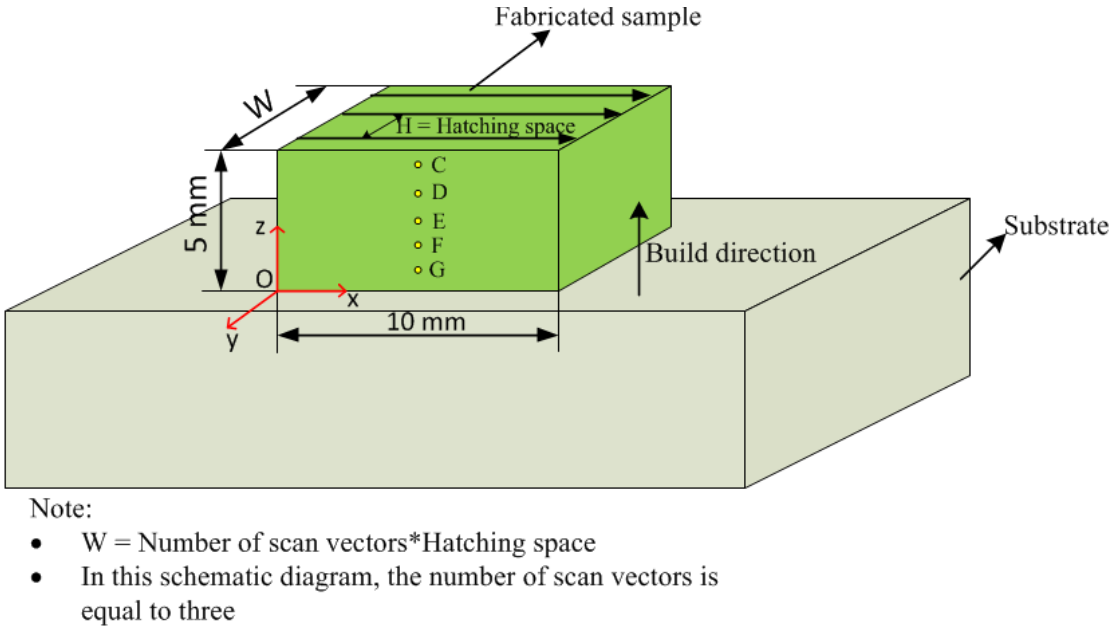

Note:

- W = Number of scan vectors*Hatching space
- In this schematic diagram, the number of scan vectors is equal to three

Figure 44. Schematic diagram illustrating the definition of processing parameters

Table 15.Coordinates of the measured points using XRD.

C	**x = 5 mm; y = 0; z = 4.5 mm**
D	x = 5 mm; y = 0; z = 3.5 mm
E	x = 5 mm; y = 0; z = 2.5 mm
F	x = 5 mm; y = 0; z = 1.5 mm
G	x = 5 mm; y = 0; z = 0.5 mm

Table 16.Parameters for XRD measurements

Focus	**1.0 mm**
Radiation	Cu Kα
Lattice plane (hkl) [90]	{420}
2Θ [90]	145 º
Ψ-tilting	0º to 45º in 6 steps each
Young modulus [91]	199,955 MPa
Poisson ration [91]	0.29

4.4 Effect of Laser Power and Scan Speed on Residual Stress

In this section, the effect of laser power and scan speed on residual stress build-up is studied for different material systems of Ti-6Al-4V fabricated via DMD process, IN718 fabricated via DMD process, and IN718 fabricated via L-PBF.

4.4.1 Effect of Laser Power and Scan Speed on Residual Stress of IN718 Built via DMD

Residual stress could be classified into three main categories based on the length scale; type I residual stress is on macroscale; type II residual stress is on microscale which always exists due to the anisotropic material properties on grain-scale; type III residual stress

which is on nanoscale and it is due to the coherency and dislocation. Type II and III residual stress has very limited effect on mechanical properties of the material and are beyond the scope of this work. Herein, our main focus is on type I residual stress. The residual stress can be beneficial by the proper selection of process parameters such as laser power, scan speed, layer thickness, and hatching space. For instance, changing the stress state from tensile to compressive could be more beneficial for the fatigue life of the component. Consequently, having a validated model to predict the residual stress state of the component within a few seconds rather than hours or days using FEM and/or experimentation is extremely valuable.

Rapid heating and cooling thermal cycles of AM leads to residual stress formation in an additively manufactured part. During the heating cycle, the laser deposited its energy to heat up the metallic powders rapidly over the melting temperature. This would create a melt pool area and a heat affected zone (HAZ) as shown in Figure 45. The heated material tends to expand but the thermal expansion is restrained by surrounding powders at a lower temperature. Therefore, a compressive stress state is formed in the heated zone. During the cooling cycle, when the heat source is gone, the heated zone begins to cool down and the shrinkage of material in this zone tend to occur, but the shrinkage is restrained by the plastic strain formed during the heating stage. Finally, tensile residual stress builds up in the heated zone. Moreover, during the DMD process, the previously melted powders experience re-melting and re-solidification cycles. This repeated melting and solidification could result in shrinkage of the material which is restrained by the previously deposited material. Consequently, a tensile stress state is formed in the newly deposited material.

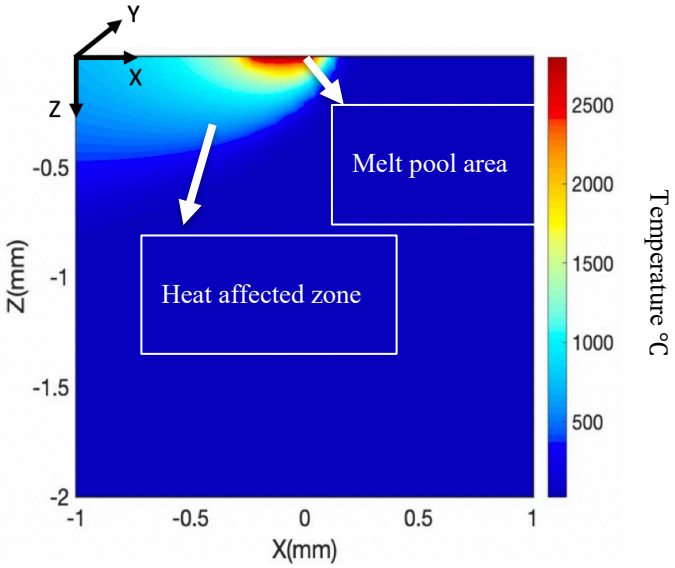

Figure 45. An illustration of melt pool area and heat affected zone.

The proposed analytical model enables the prediction of the residual stress throughout the part rapidly and accurately. The moving point heat source approach is used to predict the temperature field and temperature gradient during the DMD process. In the present work, the medium is semi-infinite, and the heat loss due to convection and radiation is ignored. Powders are considered to be stable and the effect of powder feed velocity is not considered. As shown in our previous works, the moving point heat source model can be used for both powder bed fusion systems and direct metal deposition systems [26, 27]. Thermal stresses induced by high-temperature gradient may exceed the yield strength of material. Therefore, material experience plastic deformation. By employing incremental plasticity and kinematic hardening behavior of metal, residual stress is obtained. The model presented in this work is based upon the premises of plane strain condition in the build of isotropic and homogeneous properties.

For the validation of the proposed analytical model, X-ray diffraction is used to measure the in-depth residual stress at the middle of the samples (X=10 mm, Y=1.5 mm) at every 0.5 mm along the build direction as listed in Table 10. The scan strategy in both experimentation and analytical modeling is bi-directional. Moreover, the hatching space and layer thickness are 105 μm, 250 μm. Good qualitative and quantitative agreements are observed between predicted residual stress from the analytical model and those obtained via X-ray diffraction.

Figure 46 illustrates predicted temperature field for three specimens in Table 10. Since the evaporation of the metallic powders is not considered in the modeling, the maximum temperature does not go beyond the evaporation temperature point which is 2800℃ [93]. As the laser deposited its energy into the medium, a melt pool geometry and a heat affected zone will be created. Figure 46(a) shows the temperature field for the laser power of 485 W and scan speed of 40 mm/s. Melt pool area is the region where the temperature is above the melting temperature. In this figure, the melt pool depth is around 0.75 mm based on the melting point of 1260℃. Also, the heat affected zone is the region where the temperature is above the initial temperature and below the melting temperature. In this figure, the heat affected zone is up to 1.1 mm in depth and below this depth, the rapid change in temperature is observed which shows the material below the depth of 1.1 mm is not affected by the laser as marked with a red mark. This rapid change in temperature at the border of heat affected zone would cause a change in stress state which will be explained further in the following parts of this section.

Figure 46(b) illustrates the temperature field developed within the medium with the laser power of 743 W and scan speed of 40 mm/s. The melt pool depth is 0.9 mm and the heat

affected zone continued up to 1.3 mm in depth. Figure 46(c) depicts the temperature field within the additively manufactured part with the scan speed of 920 W and scan speed of 25 mm/s. The obtained melt pool depth is 1.25 mm and the depth of heat affected zone is 1.7 mm. The border of maximum heat affected zone is shown with a red mark in all three plots. This border is of great importance since the temperature drop in this region would change the stress state from tensile to compressive which will be explained later on in this section.

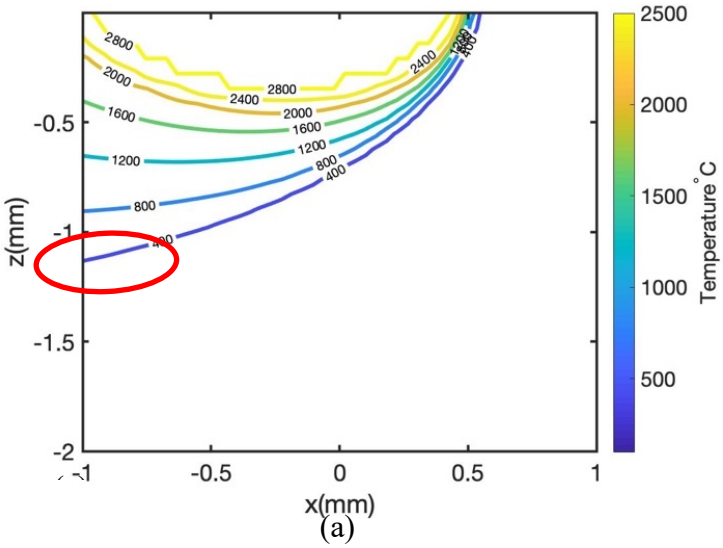

(a)

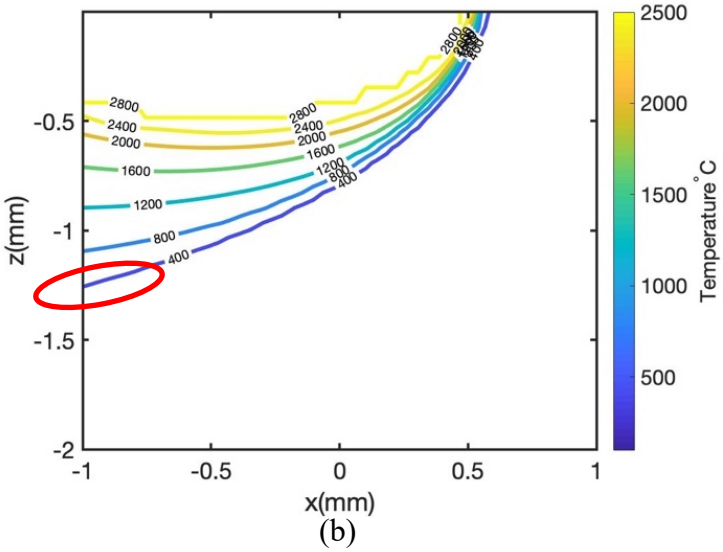

(b)

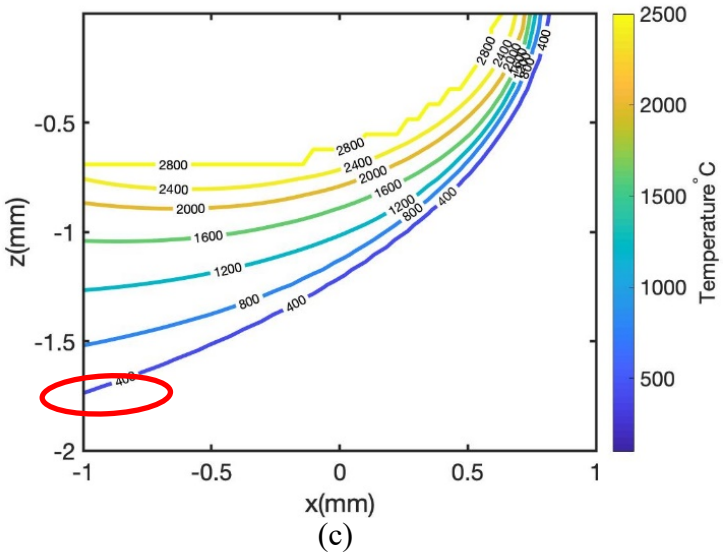

Figure 46. Predicted temperature field for DMD of IN718 for (a) P=485 W, V=40 mm/s; (b) P=743 W, V=40 mm/s; (c) P=920, V=25 mm/s.

Figures 47(a, b, and c) illustrate evolution of temperature as a function of time in different depth. Figure 4.7 (a and b) illustrate that for the same scan speed (40 mm/s), the increase in laser power leads the material to spend more time at a higher temperature, consequently bigger melt pool geometry and heat affected zone will build up. Figures 47(a, b, and c) also show the evolution of temperature as a function of time in three different depth of 1.1 mm, 1.3 mm and 1.7 mm where the residual stress state alters from tensile to compressive state in three samples with the laser power of 485 W, 743 W, and 920 W, respectively. In these plots, the rapid drop in temperature is more obvious. As explained before, since the

evaporation of material is not considered in this modeling the temperature does not go beyond evaporation temperature of IN718 which is around 2800°C [93].

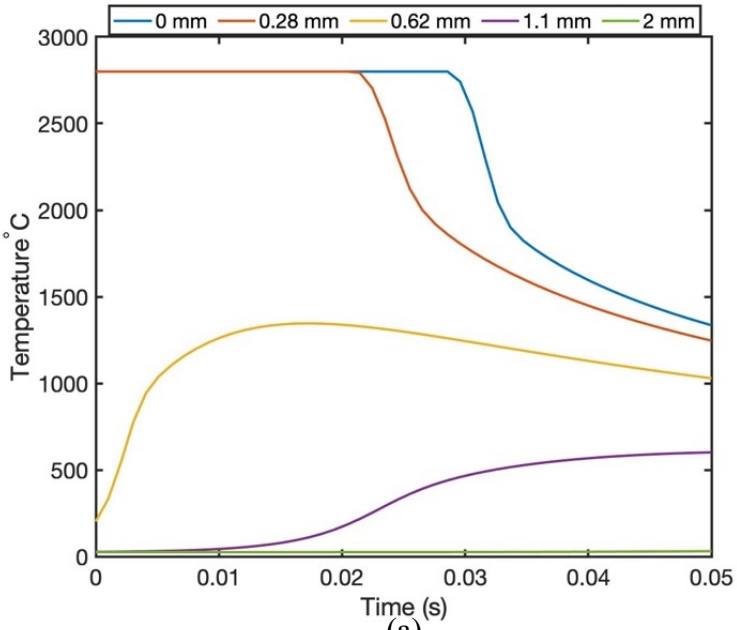

(a)

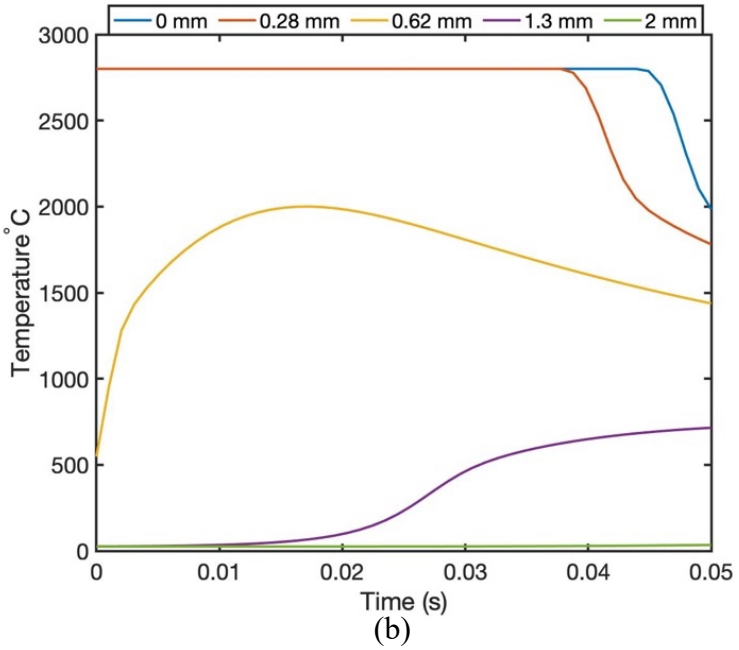

(b)

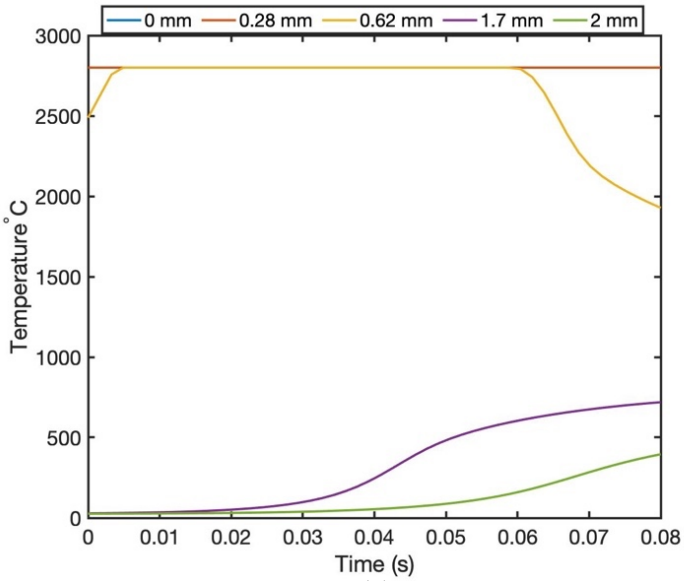

(c)

Figure 47. Predicted temperature evolution at different depth along the build direction for (a) P=485 W, V=40 mm/s; (b) P=743 W, V=40 mm/s; (c) P=920, V=25 mm/s.

Figures 48 to 50 illustrate the predicted residual stress for three different samples as listed in Table 10. Residual stress along the scan direction and transverse direction are obtained using the proposed model. Figures 48(a & b) show the residual stress along the scan direction and transverse direction for the first sample in Table 10 which has the laser power of 485 W, the scan speed of 40mm/s, the layer thickness of 250 μm, and the hatch spacing of 105 μm. It should be noted that the absorption coefficient for IN718 is 0.3 [94-96]. Residual stresses in both scan and transverse directions are highly tensile in coherence with most of the reported results in literature as explained in introduction section. The change of residual stress from tensile to compressive in both directions are observed around the

depth of 1.1 mm. This is due to the rapid change of temperature at the border of HAZ. As discussed previously, the laser heats up the metallic powders and creates a melt pool and a HAZ. The melt pool area and HAZ are under tension upon cooling. Since the material below the HAZ is at a lower temperature, this leads to the compressive stress state in the build part. Figure 45(a) illustrates the predicted temperature field for the first sample with a laser power of 485 W and scan speed of 40 mm/s. As it is shown in this figure, the melt pool geometry and heat affected zone are extended up to 1.1 mm in depth. Below this area, the temperature of the material rapidly decreases and causes the compressive state of stress to occur at this border. The experimental measurement of residual stress shows good agreement with predicted results.

Figures 49(a & b) illustrate predicted residual stress along the scan direction and transverse direction for the laser power of 743 W and scan speed of 40 mm/s, respectively. Good agreement is achieved between predicted and measure residual stresses. As shown in these figures, the tensile state of stress changes to compressive at the depth around 1.3 mm. This change corresponds to the rapid change of temperature below the HAZ as shown with a red mark in Figure 49(b).

Figures 50 (a & b) demonstrate predicted and measured residual stress for the laser power of 920 mm/s and a scan speed of 25 mm/s. Good agreement is achieved between predicted and measured residual stress. Predicted and measured residual stress show that the residual stress for the additively manufactured IN718 parts is highly tensile. However, the change in stress state is observed at the depth of 1.7 mm which corresponds to the dramatic change of temperature below the HAZ as explained before. Good agreement is achieved between predicted and measured residual stress in all three cases. The residual stress experimental

measurements are measured at every 0.5 mm in-depth as explained in previous section. While, the change in stress state in experimental measurements are captured in most of the cases, this change of stress state is not captured in some cases since the measurements' intervals were not around the HAZ (since the authors want the intervals to be the same for all the measurements).

In summary, the predicted and measured residual stress for IN718 parts built via DMD process depict that the residual stress is highly tensile and the change in stress state is related to the melt pool geometry and heat affected zone. Consequently, proper control and optimization of process are needed to reduce or eliminate the tensile residual stress which has a substantial impact on fatigue life, corrosion resistance, crack initiation and propagation, dimensional accuracy, and microstructure evolution of the AM part.

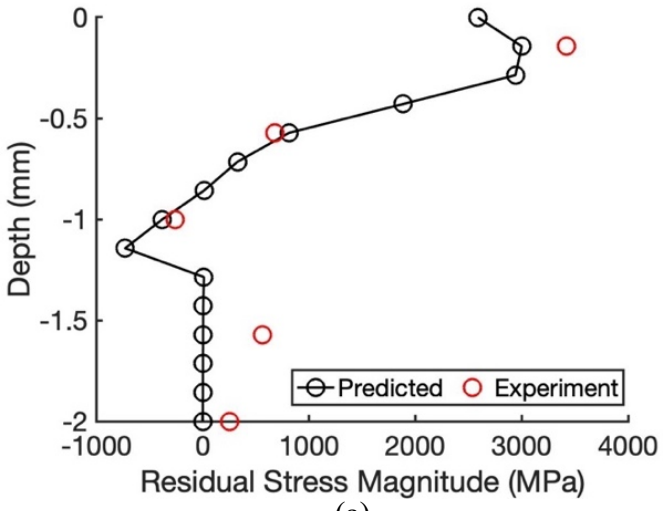

(a)

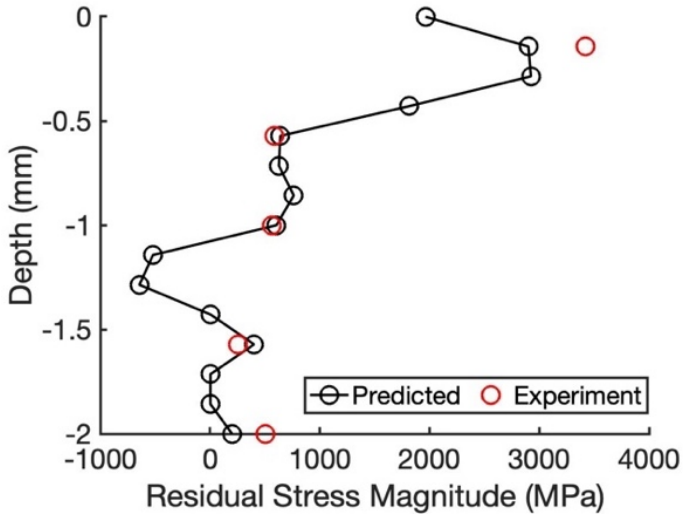

(b)

Figure 48. Predicted residual stress along (a) scan direction and (b) transverse direction for the laser power of 485 W and scan speed of 40 mm/s in the DMD build of IN718 specimens.

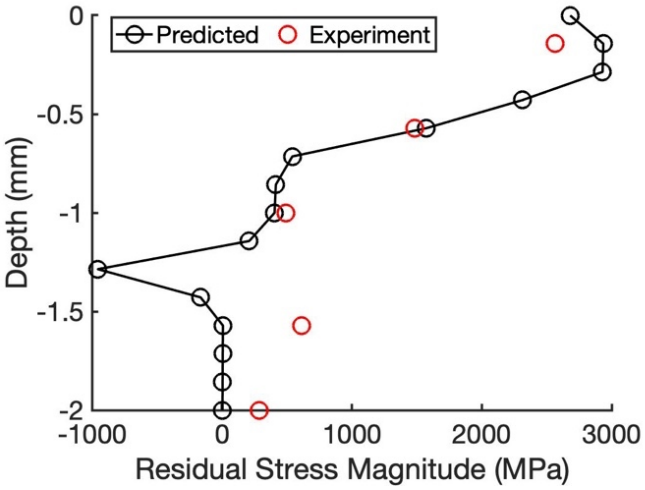

(a)

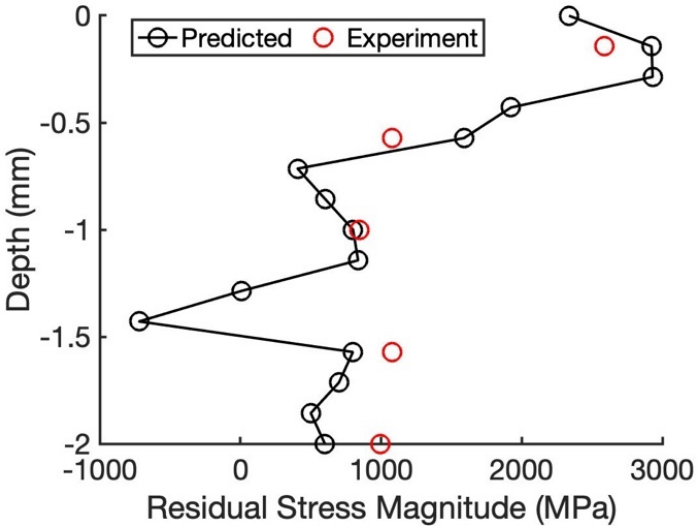

(b)

Figure 49. Predicted residual stress along (a) scan direction and (b) transverse direction for the laser power of 743 W and scan speed of 40 mm/s in the DMD build of IN718 specimens.

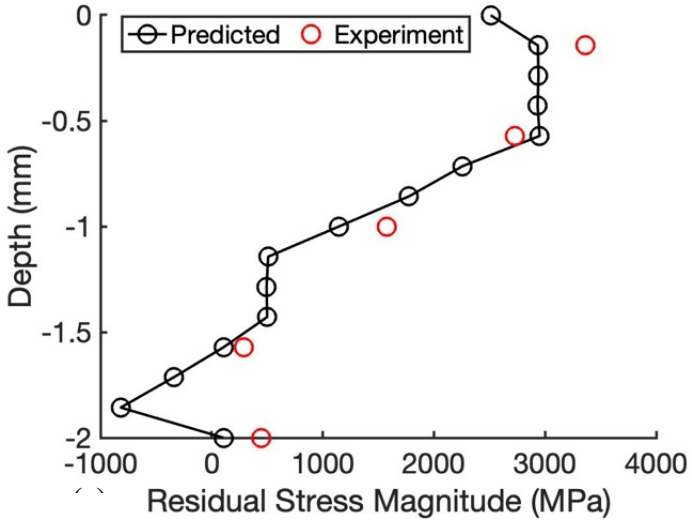

(a)

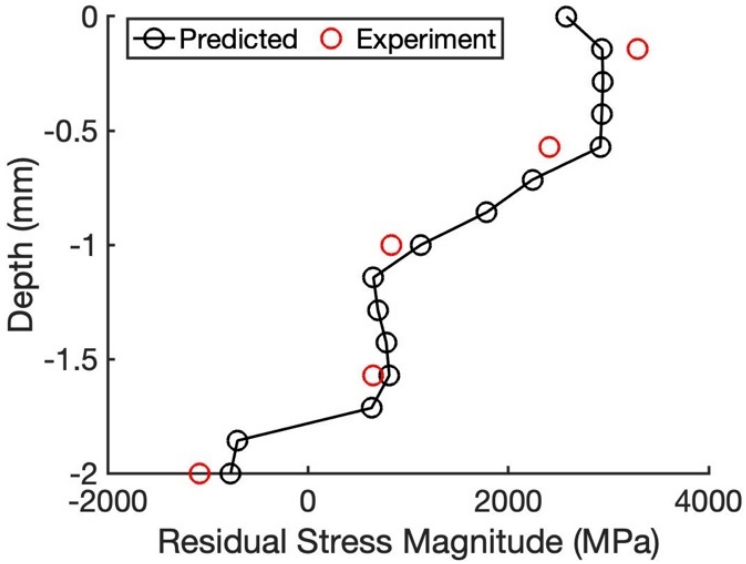

(b)

Figure 50. Predicted residual stress along (a) scan direction and (b) transverse direction for the laser power of 920 W and scan speed of 25 mm/s in the DMD build of IN718 specimens.

The proposed analytical model is used to conduct parametric study to investigate effects of laser power and scan speed on residual stress. This study looked at changing the laser power and scan speed while the layer thickness and hatching space are kept constant at 250μm and

105 μm, respectively. The average residual stress up to 1 mm below the surface is calculated (the residual stress is predicted at every 250 μm through thickness, and the average of four predicted residual stress is calculated). Three different laser powers of 100 W, 300 W and 500 W are selected with the scan speed of 20 mm/s, 40 mm/s and 60 mm/s (melting of metallic powders are obtained based on these parameters). As shown in Figure 51(a and b), for given laser power, the increase in scan speed would reduce the residual stress both along the scan direction and transverse direction. This is due to the fact that the increase in scan speed would result in a lower temperature gradient since the material has less time to absorb the energy. Consequently, reduction in temperature gradient leads to lower residual stress. Furthermore, an increase in laser power for a given scan speed leads to higher residual stress in both scan direction and transverse direction since the material absorbs more energy which would result in a higher temperature gradient. Moreover, the residual stress along the scan direction has a higher magnitude compared to the residual stress in the transverse direction. The main reason is that the thermal gradient is higher in scan direction compared to transverse direction.

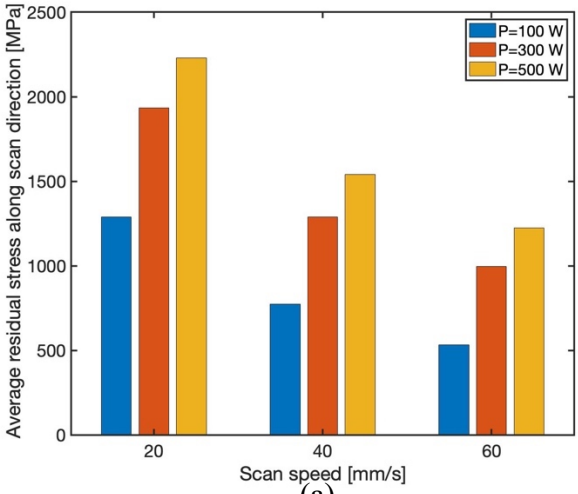

(a)

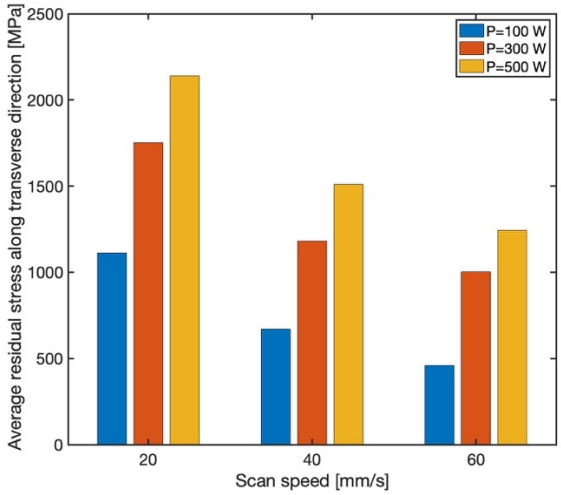

(b)

Figure 51. Predicted residual stress along (a) scan direction; (b) transverse direction

4.4.2 Effect of Laser Power and Scan Speed on Residual Stress of Ti-6Al-4V Built via DMD

Figure 52 illustrates the melt pool area and heat affected zone induced by highly localized heat input and low thermal conductivity. Non-uniform heating induces non-uniform thermal expansion. During heating cycle, the melt pool area and the heat affected zone are trying to expand; however, they are surrounded by solidified metal. This would generate

the compressive stress state within the melt pool and heat-affected zones as shown in Figure 53(a). During the cooling cycle, the shrinkage of the material would develop tensile stress state as illustrated in Figure 53(b).

The proposed analytical model is extremely valuable since it provides fast (less than 45 seconds with 4-processor laptop) and accurate prediction of stress state within the build. In this modeling, first, a transient moving heat source approach is used to predict the temperature field in AM. Second, the thermal stress induced is calculated by combining three stresses known as stresses due to body forces, normal tension, and hydrostatic stress. Last, the stresses may exceed the yield point and material would experience plastic deformation. As a consequence of repeated loading and unloading (heating and cooling), material experiences high residual stress. Therefore, both the in plane and out of plane residual stress distributions are calculated from incremental plasticity and kinematic hardening behavior of the metal based upon the premises of plane strain condition in the build of isotropic and homogeneous properties, in coupling with the equilibrium and compatibility conditions.

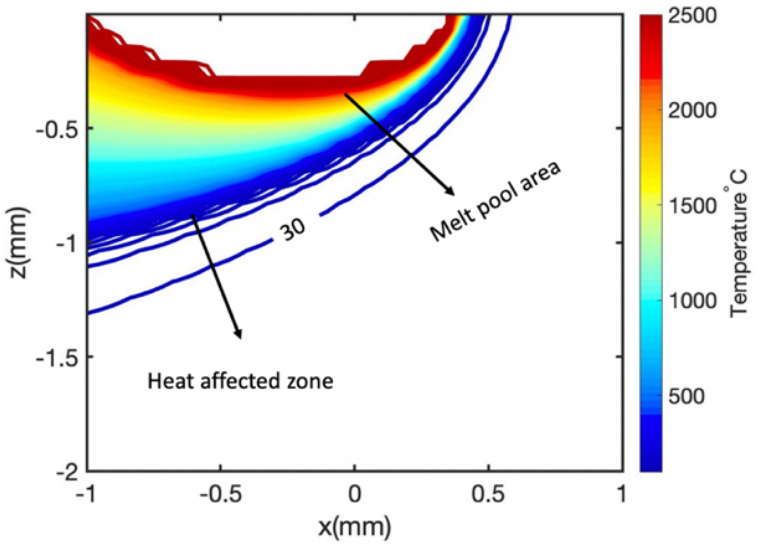

Figure 52. Illustration of melt pool and heat-affected zone.

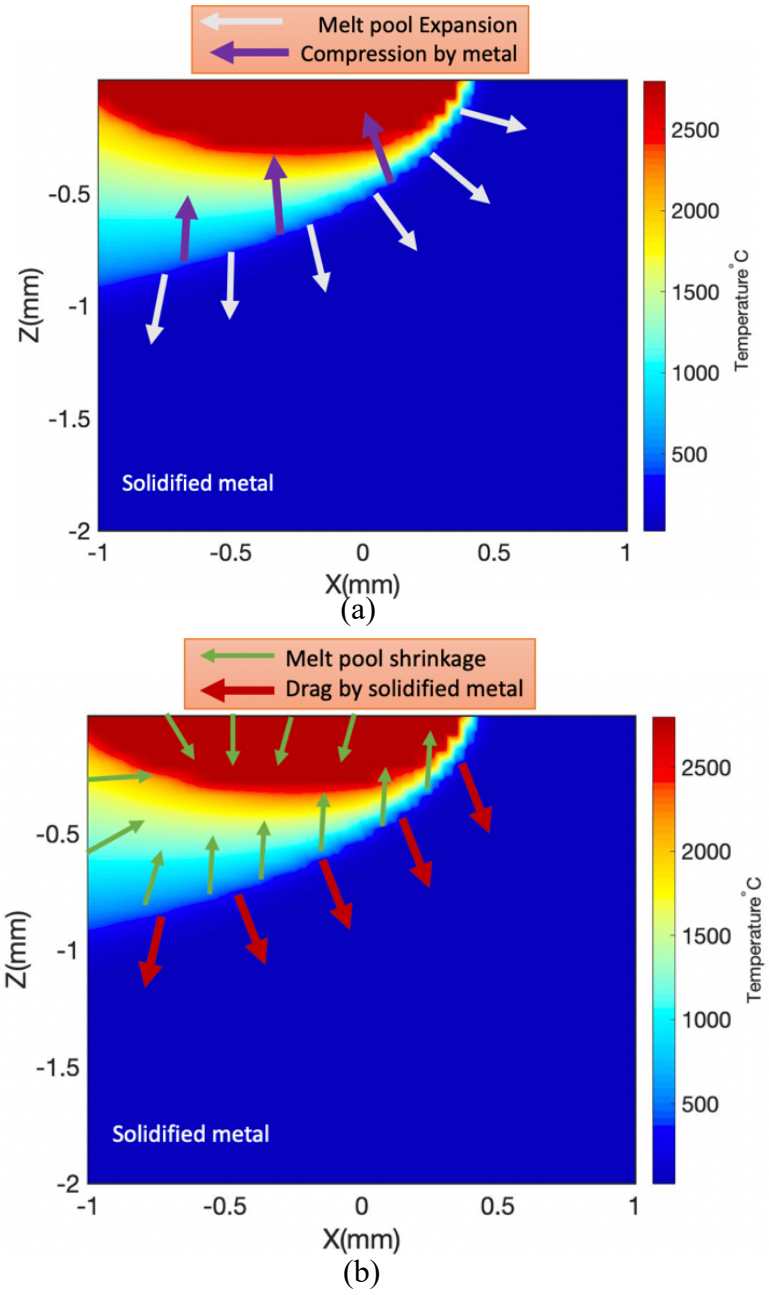

Figure 53. Illustration of accumulation of stress during (a) heating cycle; (b) cooling cycle

Material properties could vary significantly from point to point due to the steep temperature gradient. Consequently, it is not a fair assumption to consider the material properties

constant. Herein, the thermal and mechanical material properties are temperature sensitive. Moreover, in this process, material experience cyclic melting and solidification. The energy needed for the phase change is taken into account by incorporating the latent heat of fusion into specific heat. Furthermore, the multi-layer and multi-scan aspect of metal AM are considered by including the temperature histories from the previous layers and scans.

Experimental measurements are conducted via X-ray diffraction to measure the residual stress in Ti-6Al-4V specimens built via DMD process at the middle of the specimens (*X=10 mm, Y=1.5 mm*) along the build direction (*z-axis*) at every *0.5 mm* as explained in section 4.3.2. The scan strategy in both experimentation and analytical modeling is bi-directional. Moreover, the hatching space and layer thickness are 105 μm, 250 μm, respectively. Comparison of the results from the proposed analytical model and experimentation of Ti-6Al-4V specimens built via DMD process showed good qualitative and quantitative agreement.

Figure 54 illustrates the predicted temperature field for Ti-6Al-4V specimens. Figure 54(a) demonstrates the predicted melt pool area and heat-affected zone (HAZ) for the first specimen in Table 12, which has a laser power of 206 *W*, the scan speed of 25 *mm/s*, with the layer height and hatch spacing of 250 μm and 105 μm, respectively. It should be noted that the absorption ratio is 30% for Ti-6Al-4V samples as explained in the work of Selvan *et al.* [97]. Since the evaporation of the metallic powders is not considered in the modeling, the maximum temperature does not go beyond the evaporation temperature which is around 3000℃ for Ti-6Al-4V as reported by Selvan *et al.* [97]. In this figure, the melt pool depth is around 0.1 *mm* based on the melting point of 1600℃, and the depth of heat affected zone

is around 0.15 *mm*. Below this depth, the material is not affected by laser. The rapid temperature change at the border of HAZ and complete solid material- which is not affected by the laser- is the region where the stress state within the build part changes from tensile to compressive. This phenomenon will be explained in detail in the following sections of this manuscript. Figure 54(b) illustrates the predicted temperature field for the second specimen with the laser power of 385 W, scan speed of 40 *mm/s*, layer height of 250 μm and hatch spacing of 105 μm. Based on the melting point of Ti-6Al-4V (1600℃), the melt pool depth is 0.14 *mm* and the HAZ depth is around 0.21 *mm*.

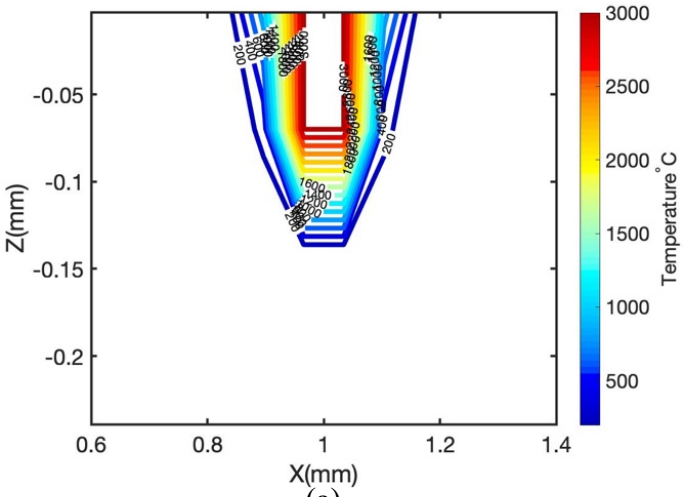

(a)

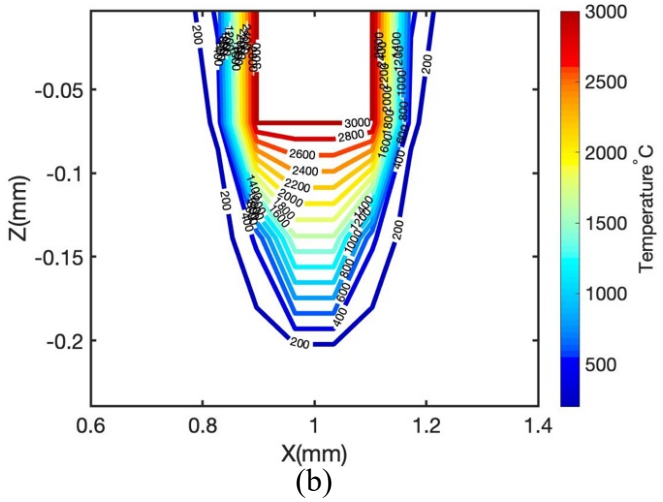

(b)

Figure 54. Predicted temperature field for Ti-6Al-4V with (a) laser power= 206 W and scan speed= 25 mm/s; (b) laser power=385 W and scan speed =40 mm/s.

As explained before material properties vary significantly since the temperature gradient is quite high in AM. The variation of thermal and mechanical material properties for the second specimen with the laser power of 385 W, and scan speed of 40 mm/s illustrated in Figure 55. Density of the solid material is around 4400 kg/m^3. As the temperature increase the density decreases to 4050 kg/m^3 in the liquid zone; in the melt pool zone, thermal conductivity reaches its maximum value due to the high magnitude of temperatures, and decreases to around 5 W/m℃ in the solid zone; specific heat has the highest magnitude of 530 J/Kg℃ at the melt pool area and drops to 480 J/Kg℃ when the material is solidified; thermal expansion is more expanded in the liquid zone compare to other properties which shows the thermal expansion is more sensitive to temperature, and has the highest magnitude in the liquid zone; elastic modulus in the liquid zone is almost zero, in the HAZ reaches to 60 GPa, and in the solid zone reaches the maximum value of 120 GPa; Poisson's ratio in the liquid zone has the magnitude of 0.38, and in the solid zone has the value of 0.29; yield strength reaches to almost zero at liquid zone and has the maximum value of 1200 MPa in solid zone.

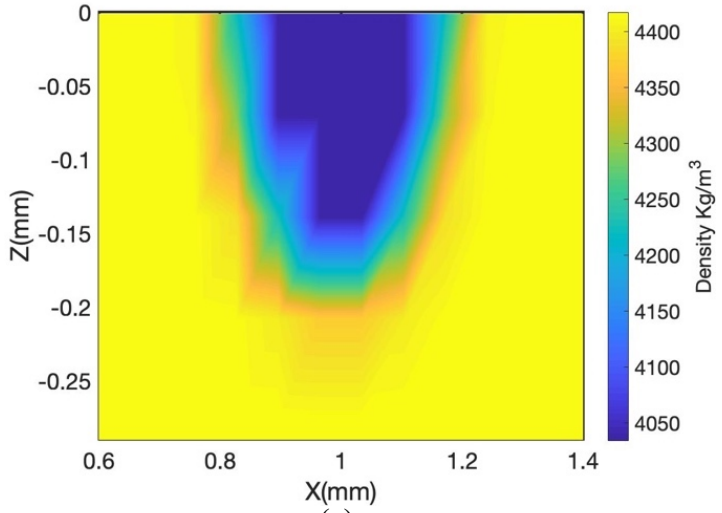
0
-0.05
-0.1
-0.15
-0.2
-0.25
Z(mm)
0.6
0.8
1
1.2
1.4
X(mm)
4400
4350
4300
4250
4200
4150
4100
4050
Density Kg/m3

(a)

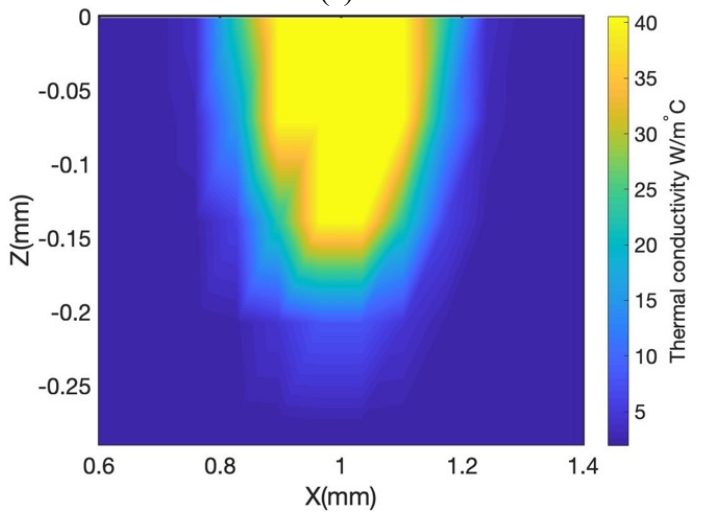
0
-0.05
-0.1
-0.15
-0.2
-0.25
Z(mm)
0.6
0.8
1
1.2
1.4
X(mm)
40
35
30
25
20
15
10
5
Thermal conductivity W/m °C

(b)

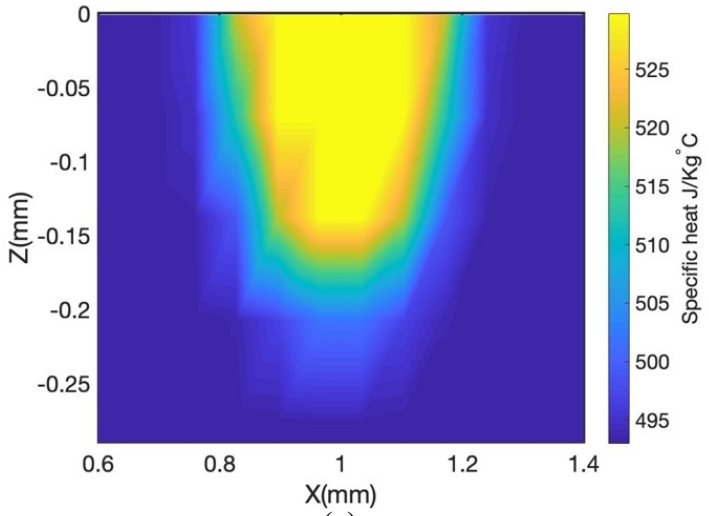
0
-0.05
-0.1
-0.15
-0.2
-0.25
Z(mm)
0.6
0.8
1
1.2
1.4
X(mm)
525
520
515
510
505
500
495
Specific heat J/Kg °C

(c)

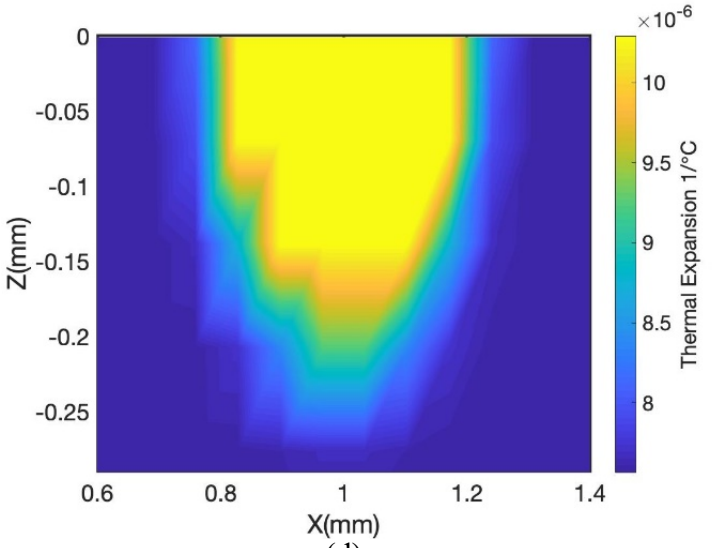
0
-0.05
-0.1
-0.15
-0.2
-0.25
Z(mm)
0.6
0.8
1
1.2
1.4
X(mm)
×10-6
10
9.5
9
8.5
8
Thermal Expansion 1/°C

(d)

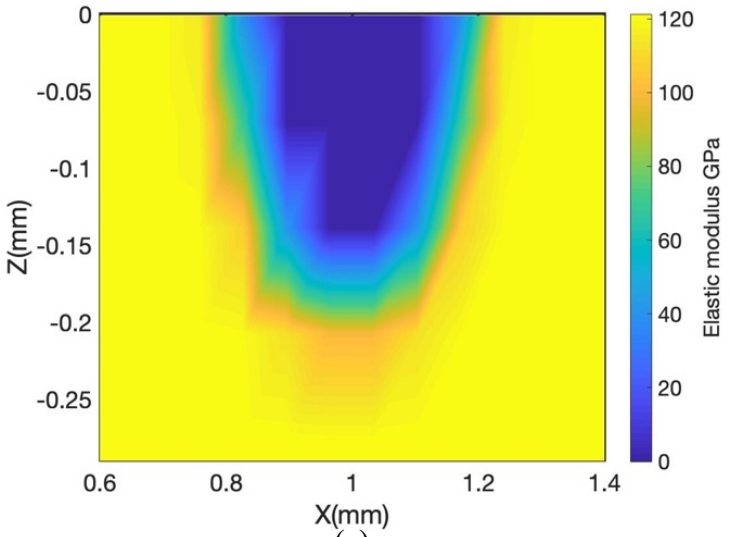
0
-0.05
-0.1
-0.15
-0.2
-0.25
Z(mm)
0.6
0.8
1
1.2
1.4
X(mm)
120
100
80
60
40
20
0
Elastic modulus GPa

(e)

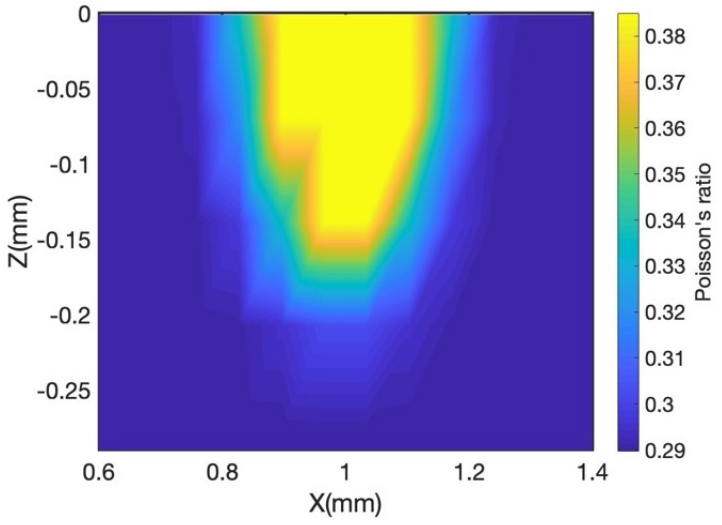
0
-0.05
-0.1
-0.15
-0.2
-0.25
Z(mm)
0.6
0.8
1
1.2
1.4
X(mm)
0.38
0.37
0.36
0.35
0.34
0.33
0.32
0.31
0.3
0.29
Poisson's ratio

(f)

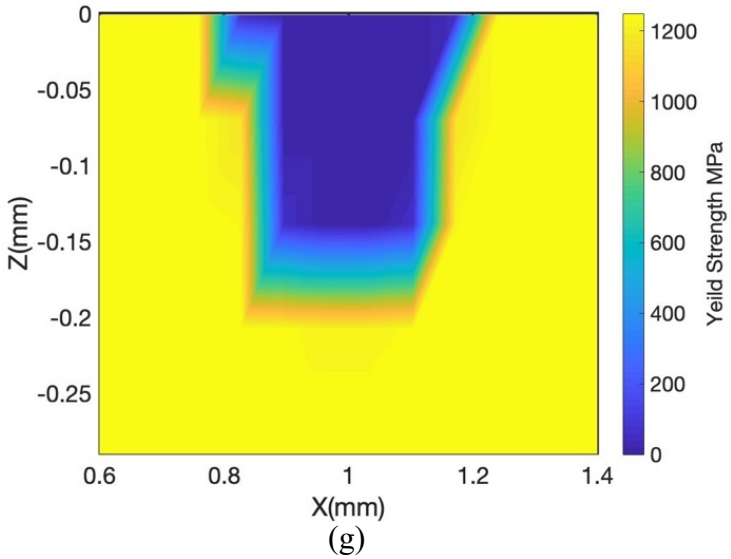

(g)

Figure 55. Predicted material properties distribution for Ti-6Al-4V with the laser power of 385 W, and scan speed of 40 mm/s. (a) density;(b) conductivity;(c) specific heat; (d) thermal expansion; (e) elastic modulus; (f) Poisson's ratio; (g) Yield strength

Residual stress along the scan direction and transverse direction is predicted using the proposed model and validated experimentally. Figure 56 illustrates predicted residual stress along the scan direction and transverse direction as a function of depth into the build part for the first sample with the laser power of 206 W, scan speed of 25 mm/s, layer height of 250 μm, and hatch spacing of and 105 μm. Since the samples have the rough surface, the top surface of the samples is polished up to 100 μm with the electromechanical polishing to be able to accurately measure the residual stress on the surface.

Both the in plane and out of plane residual stresses are highly tensile in the melt pool zone and heat affected zone in coherence with most of reported results in literature as explained in introduction section. As shown in Figures 56 and 57, in both scan direction and

transverse direction, there is a gradual change in stress state from tensile to compressive. This change occurs at around the depth where the medium is solidified and is not affected by the laser. The results confirm that upon cooling the melt pool and heat affected zones are under tension due to the shrinkage of the material, and when the below material is completely solidified and is not affected by the laser anymore, material experience compression stress state. The oscillations in the melt pool and heat affected zone is due to the fact that the thermal and mechanical material properties vary significantly in these regions. Therefore, an abrupt change in one of the material properties would results in oscillations. This could be better improved by having more material properties data points at different temperatures.

Figure 57 shows the predicted residual stress in the scan and transverse directions for the second sample in Table 12 with the laser power of 385 W, scan speed of 25 mm/s, and layer height and hatch spacing of 250 μm and 105 μm, respectively. The stress state is tensile in both the scan and transverse directions and changes to compressive at the depth around 0.9 mm. Around this region the material is completely solidified and is not affected by the laser. Comparison of predicted and measured residual stress follows each other closely.

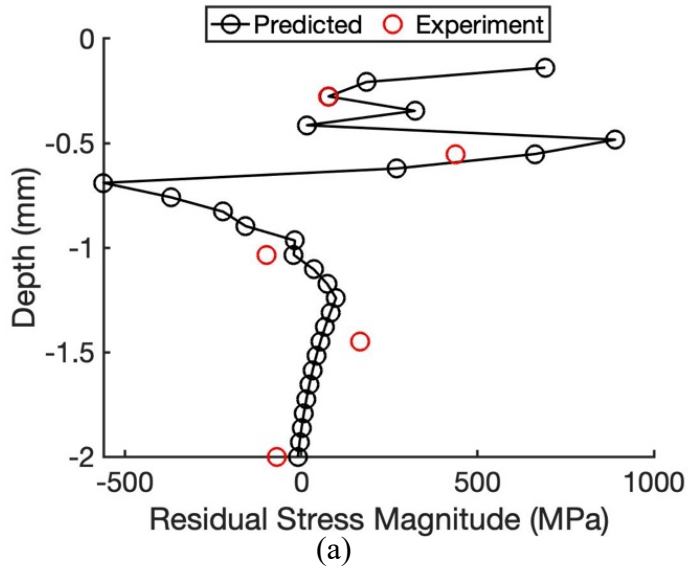

(a)

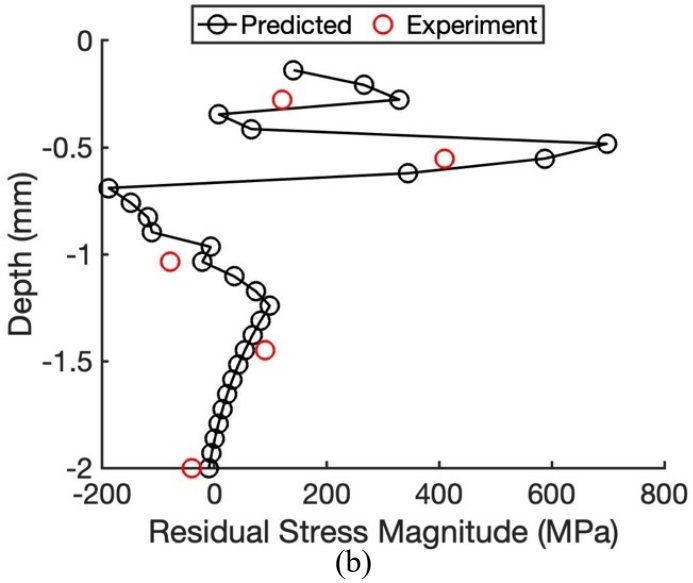

(b)

Figure 56. Predicted residual stress for Ti-6Al-4V with laser power of 206 W, and scan speed of 25 mm/s along (a) scan direction; (b) transverse direction.

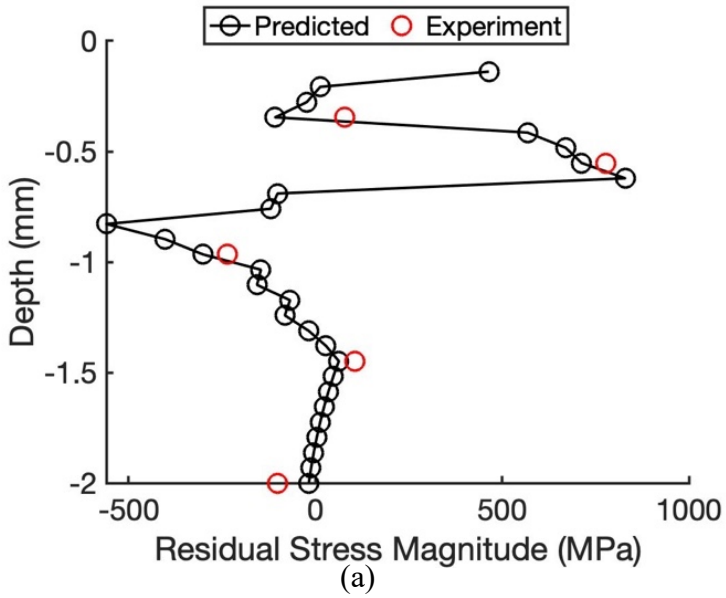

(a)

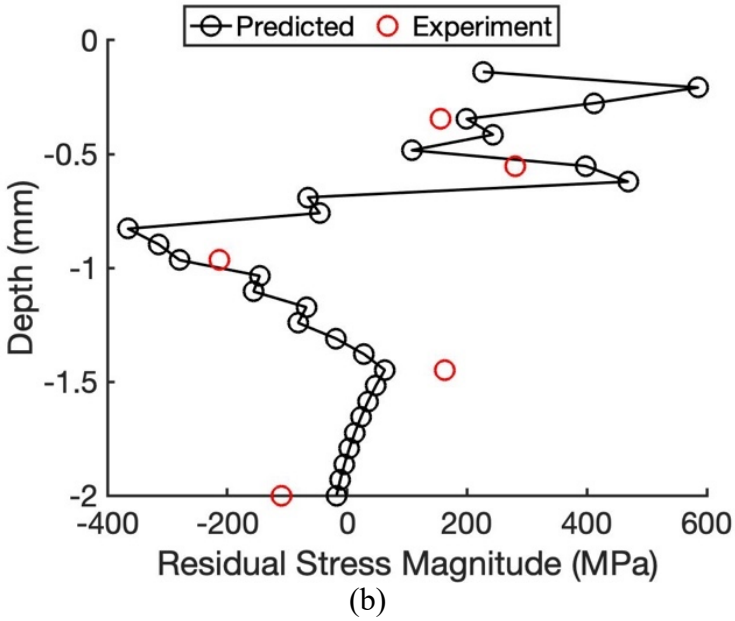

(b)

Figure 57. Predicted residual stress for Ti-6Al-4V with laser power of 385 W, and scan speed of 40 mm/s along (a) scan direction; (b) transverse direction.

4.4.3 Effect of Laser Power and Scan Speed on Residual Stress of IN718 Built via L-PBF

At a specific temperature during L-PBF process, the strain hardening dominates which increases the flow stress. Work hardening and thermally activated softening mechanisms take place due to the combined effects of repeated heating and cooling cycles in L-PBF. Figure 58 illustrates the stress-strain curve of IN718 for various temperatures. As illustrated in this figure, the flow stress is very sensitive to the temperature, and it decreases with an increase in temperature. The stress-strain curve of IN718 can be divided into four main stages of work hardening, transitioning, softening, and steady stage. Due to the accumulation of dislocations, the strain hardening dominants over the softening rate induced by dynamic recovery, thus the stress rises sharply. Hardening stage is followed by the transitioning stage, where hardening and softening phenomenon induced by dynamic recovery and recrystallization compete. Due to the dominance of dynamic recovery and dynamic recrystallization the flow stress drops which indicates the softening stage of the stress-strain curve. Finally, the stress stabilizes due to the balance between hardening and softening [98].

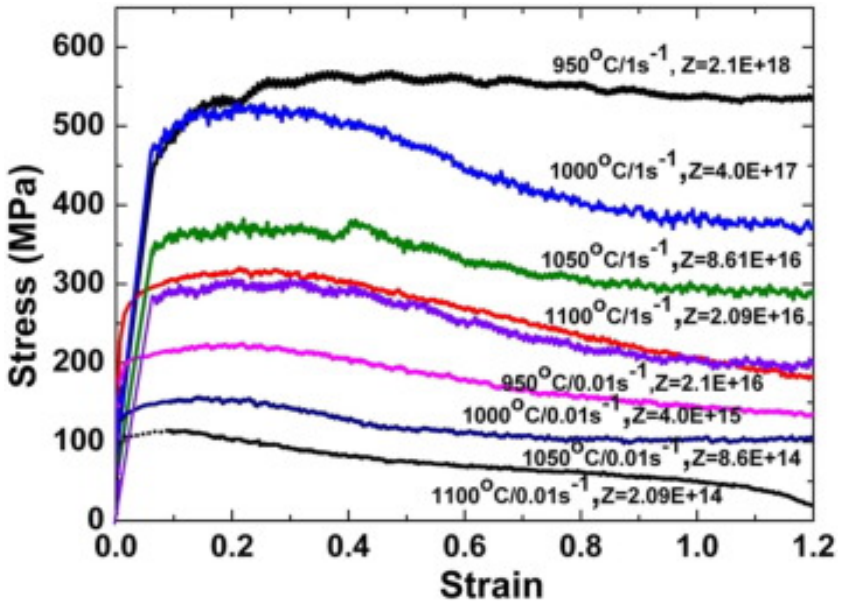

Figure 58. Stress-strain curve of the IN718 at different temperatures and strain rates [98].

Tancret *et al.* studied the dynamic material behavior of Ni-based superalloys, in which yield stress behavior of the material is given as a function of temperature. In this work, the dynamic strain aging phenomenon is observed, where a sudden increase in stress around 600℃ followed by a sharp decrease with increasing temperatures is revealed. It was also reported that the temperature-dependent flow softening phenomenon occurs after a critical strain at high strains. It was claimed that flow softening with increasing strain at high strain rates, but low temperatures is a result of athermal micro-mechanical phenomenon, such as rearranging dislocations, and at high temperatures thermally activated micro-mechanical phenomenon, such as increasing number of slip planes with phase change and dynamic recrystallization, etc. This softening behavior has an impact on material flow stress which has an influence on the yield surface [99].

Modifications to the Johnson-Cook materials' model have been offered to include the temperature dependent flow softening and the effect of grain growth on yeild strength using Hall-patch equation. The Hall-Patch equation is introduced as;

$$A = A_{hp} + K_{hp} d^{-0.5} \tag{4.3}$$

Where A is the yield strength parameter, d is the average grain size obtained from dynamic recrystallization and grain refinement models, A_{hp}, and K_{hp} are material constants. Then the modified J-C flow stress model could be written as [100]

$$\sigma = (A_{hp} + K_{hp} d^{-0.5} + B{\varepsilon_{eff}^{p}}^{n})(1 + Cln\left(\frac{\dot{\varepsilon}_{eff}^{p}}{\dot{\varepsilon}_0}\right))(1 - \left[\frac{T-T_0}{T_m-T_0}\right]^m)(D + (1 - D)[\tanh(\frac{1}{(\varepsilon+S)^r})]^s \tag{4.4}$$

where ε_{eff}^{p} is the effective plastic strain, $\dot{\varepsilon}_{eff}^{p}$ is the effective plastic strain rate, T is the temperature of material, T_m is the melting point of material, and T_0 is the initial temperature. The terms A_{hp}, K_{hp}, B, C, n, m, D, S, r, s and $\dot{\varepsilon}_0$ are the material constant which is listed in Table 17 for IN718 material.

Table 17. Modified Johnson-Cook parameters for IN718 [79].

A_{hp}(MPa)	K_{hp}	B(MPa)	C	n	m	D	S	s	r	$\dot{\varepsilon}_0$
378	298.4	1370	0.02	0.164	1.03	0.6	0	5	1	1

The same procedure as explained in chapter 3 is used to predict the residual stress. The proposed thermo-mechanical analytical model predicts the residual stress under strain hardening, flow softening, and microstructural evolution effects during L-PBF process. Under repeated heating and cooling cycles, DRx takes place which results in newly formed grains around the grain boundaries. During the heating cycle, the dynamic recrystallization affected grain size is obtained by calculating the recrystallized volume fraction, and the average grain size is obtained from the nucleation and grain growth using mixture rule. Moreover, in metal AM, the rapid solidification could result in grain refinement, which then alters the grain size. The final grain size is obtained through DRx and grain refinement models introduced in the previous chapter. The dynamic recrystallization and grain refinement play an important role in hardening and flow softening behavior of the material, thus, alter the flow stress and yield surface which then impacts the residual stress build-up during L-PBF process. The grain size determines the yield strength of the material; thus, the Hall-Patch equation is used to draw a relationship between yield strength parameter and grain size. Consequently, the flow softening, and microstructure affected flow stress is calculated using the modified Johnson-Cook model to determine the yield threshold.

The residual stress affected by strain hardening, flow softening, and microstructural evolution effects predicted through the prediction of temperature field, thermal stress, flow stress, dynamic recrystallization, and grain refinement. The transient moving point heat source approach is used to predict the temperature field considering the temperature-dependent material properties, scan strategies of hatching space, layer thickness, and scan path, energy needed for solid-state phase change, and edge effects. Figure 59 illustrates the predicted temperature field for three IN718 samples built via L-PBF. Figure 59(a)

illustrates the predicted temperature field for the laser power of 150 W, scan speed of 600 mm/s, powder layer thickness of 30 μm, hatching space of 100 μm, and number of scans of 50. The melt pool depth for this sample is around 190 μm based on the melting point of 1260℃. Figure 59(b) illustrates the predicted temperature field for the laser power of 250 W, scan speed of 600 mm/s, powder layer thickness of 30 μm, hatching space of 100 μm, and number of scans of 50. The predicted melt pool depth is around 265 μm. And, Figure 59(c) shows the predicted temperature field for the laser power of 150 W, scan speed of 1000 mm/s, powder layer thickness of 30 μm, hatching space of 100 μm, and number of scans of 50. The melt pool depth for this sample is around 127 μm.

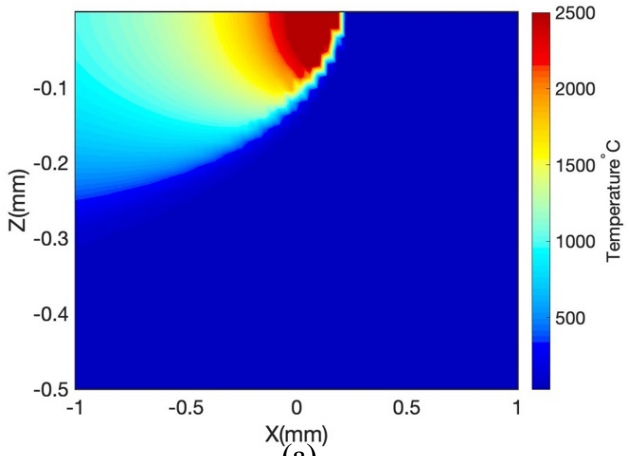

(a)

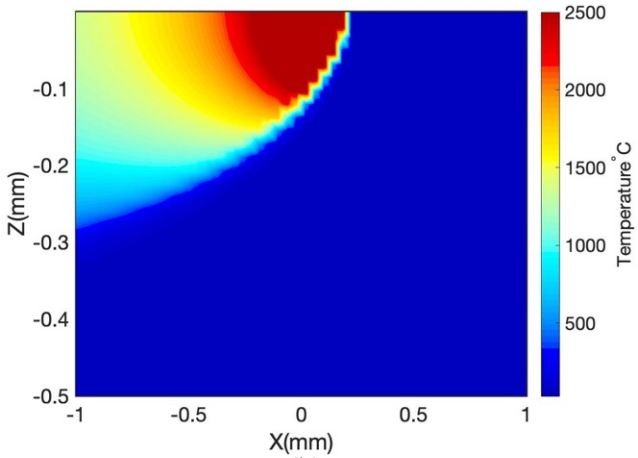

(b)

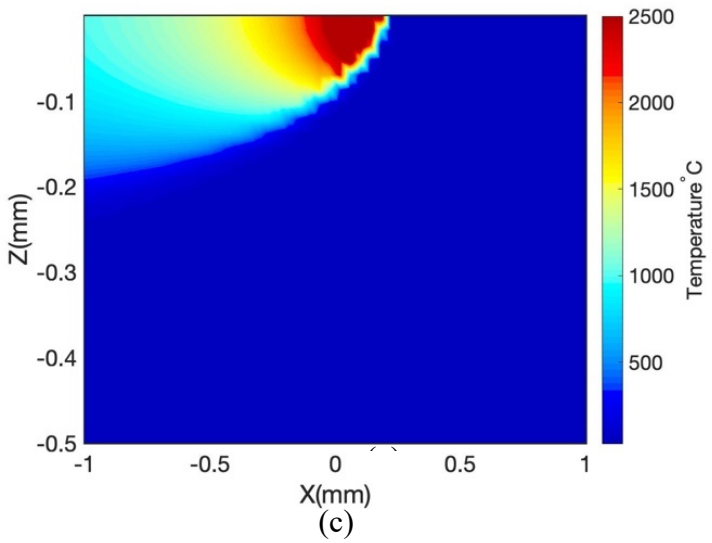

Figure 59. Predicted temperature field for IN718 specimens built via L-PBF for (a) laser power of 150 W and scan speed of 600 mm/s, (b)laser power of 250 and scan speed of 600 mm/s, and (c) scan speed of 150 W and laser power of 1000 mm/s.

Figures 60 to 62 illustrate the predicted residual stress affected by strain hardening, flow softening and microstructural evolution for the three IN718 specimens built via L-PBF as listed in Table 14. Figure 60(a) illustrates the through-thickness predicted residual stress along the scan direction for the laser power of 150 W and scan speed of 600 mm/s (First sample in Table 14). Part experiences high tensile residual stress due to the rapid cooling which induces shrinkage of the material restrained by the high plastic strain formed during the heating cycle. The predicted residual stress follows the measured residual stress. Figure 60(b) demonstrates the predicted residual stress along the build direction. As shown in this figure, the predicted residual stress is highly tensile, and also the magnitude of the residual

stress along the build direction is higher than that along scan direction in agreement with the reported results in the literature. Different heat transfer mechanisms, and material properties distribution have a crucial impact on the magnitude of residual stress along different directions as mentioned by Ganeriwala *et al.* [40]. A comparison is also conducted to illustrate the effects of considering the flow softening and DRx [35] on residual stress prediction. The results are compared to the predicted residual stress without considering the effects of flow softening and DRx on the flow stress model. As shown in Figure 60, the predicted residual stress considering the effects of flow softening and microstructural evolution shows better agreement with residual stress measurements. In this case, the predicted residual stress without considering the effects of flow softening and microstructural evolution along the scan and build directions is underestimated which is due to the underestimation of flow stress.

Figures 61(a & b) illustrate the predicted residual stress along the scan direction and build direction, respectively for the laser power of 250 W and scan speed of 600 mm/s (sample 5 in Table 14). The predicted residual stress is tensile and increases as it gets closer to the surface. In most of the points through thickness, the predicted and measured residual stress follows each other closely. However, at the depth of *4.5 mm* from the base, the experimental residual stress measurement along the build direction drops out of expectation. The surface oxidation could be a very important reason that contributes to this error between predicted and measured residual stress. Furthermore, the predicted residual stress considering the effects of flow softening and microstructural evolution is compared to the predicted residual stress when these factors are ignored. The results showed that the predicted residual stress considering the effects of flow softening and microstructural

evolution more accurately follows the experimentations, while the predicted residual stress without considering these effects is overestimated due to the underestimation in yield surface, which then impacts the plastic deformation and residual stress build-up predictions.

Figures 62(a & b) illustrate the predicted residual stress along the scan direction and build direction, respectively, for the laser power of 150 W and scan speed of 1000 mm/s (sample 6 in Table 14). The predicted residual stresses along the scan and build directions are tensile, and also the magnitude of the residual stress along the build direction is higher than that along scan direction due to the heat transfer and material properties distributions. Moreover, a comparison is conducted to illustrate the importance of considering the flow softening and microstructural evolution effects on residual stress prediction. The results indicate that the predicted residual stresses along the scan and build directions ignoring these factors are overestimated due to the underestimation in yield surface, which then impacts the plastic deformation and residual stress build-up predictions.

Thus, as shown in these figures the predicted residual stress along the scan direction and build direction follows the residual stress experimentations closely when the effects of flow softening and grain size on dynamic material behavior are considered. The predicted residual stress without considering these effects in most of the cases is overestimated. Thus, considering the microstructural evolution, and flow softening could help to more accurately predicted the residual stress within the additively manufactured parts.

Moreover, the comparison of the results in Figures 60 and 61 showed that for a given scan speed, the increase in laser power would increase the tensile residual stress build-up within

the IN718 parts due to the increase in plastic deformation. Also, for a given laser power (Figures 4 and 4.57), the increase in scan speed would increase the residual stress due to the increase in cooling rate.

In all three cases, good agreement is obtained between predicted residual stress and X-ray measurements used to determine the residual stress of IN718 parts build via L-PBF when the flow softening, and microstructure evolution affected flow stress are considered in the modeling of residual stress. Therefore, the proposed model is a valuable, reliable, and rapid tool for the prediction of stress state within the part which then can be used for the optimization of process parameters and control of the build process.

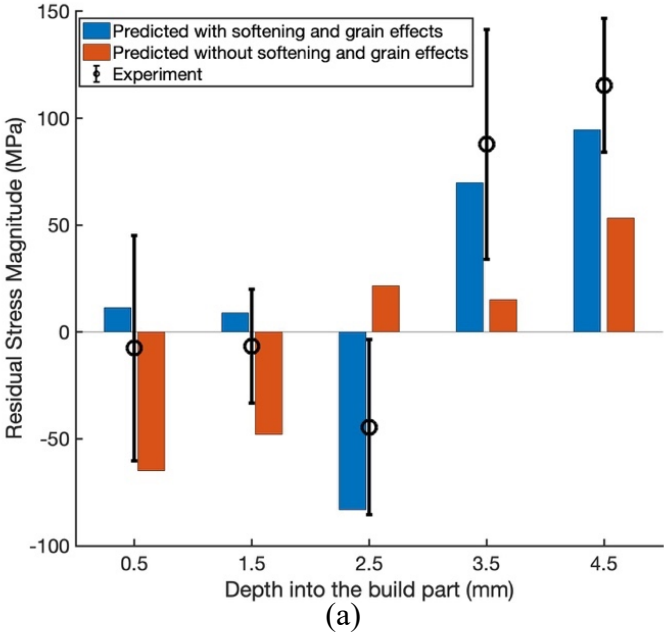

(a)

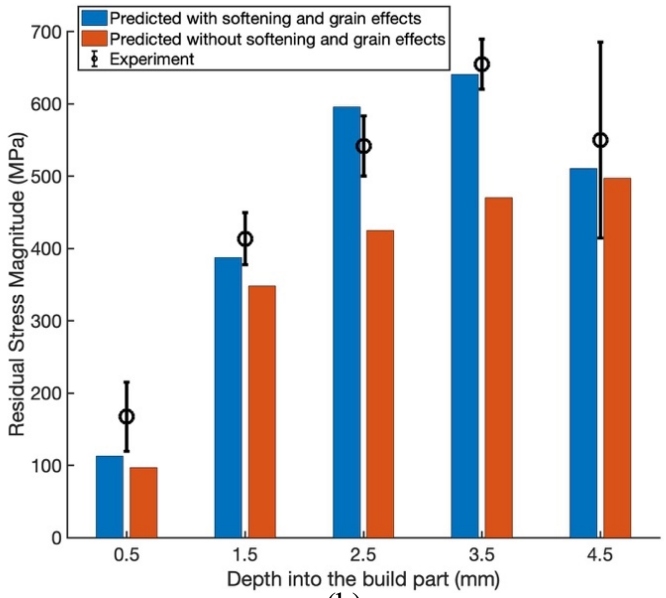

(b)

Figure 60. Comparison of the predicted residual stress considering the effects of flow softening and microstructure to the residual stress predicted without considering the effects of flow softening and microstructure during L-PBF of IN718 with laser power of 150 W and scan speed of 600 mm/s (a) along the scan direction; (b) along the build direction.

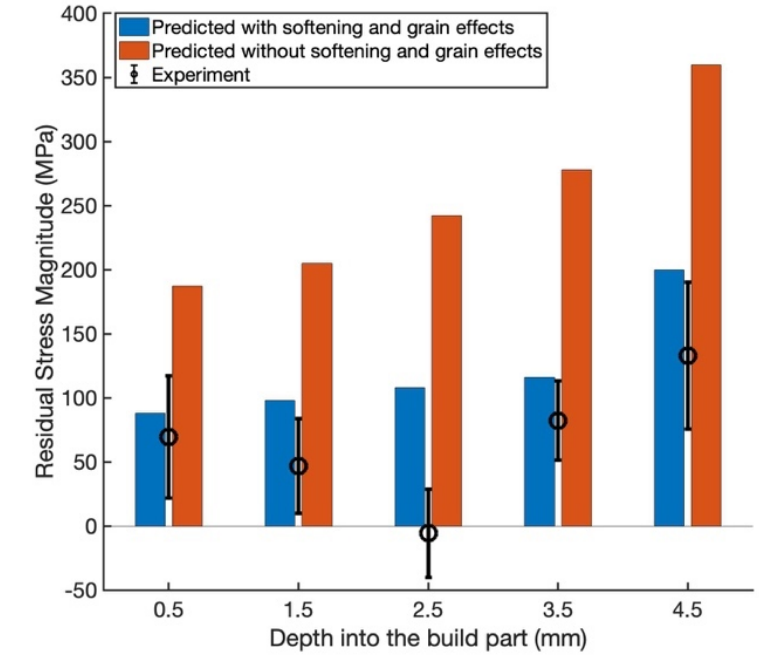

(a)

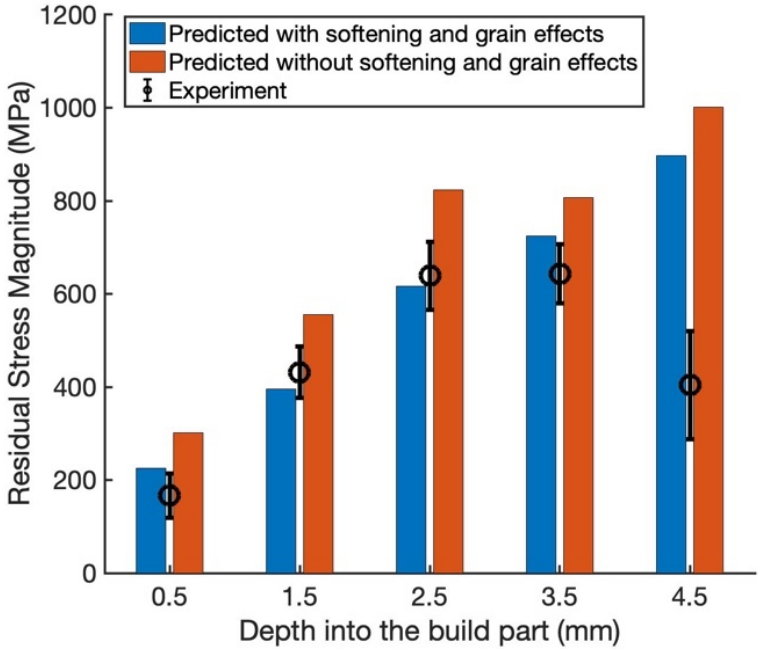

(b)

Figure 61. Comparison of the predicted residual stress considering the effects of flow softening and microstructure to the residual stress predicted without considering the effects of flow softening and microstructure during L-PBF of IN718 with laser power of 250 W and scan speed of 600 mm/s (a) along the scan direction; (b) along the build direction.

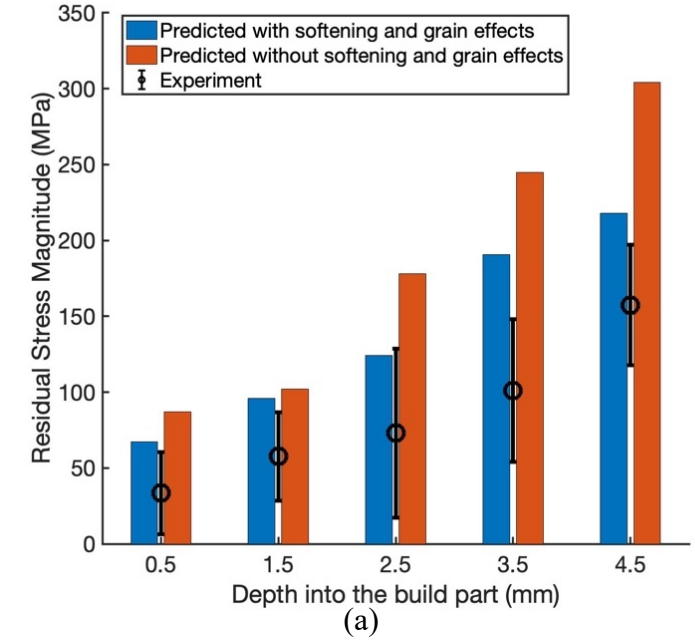

(a)

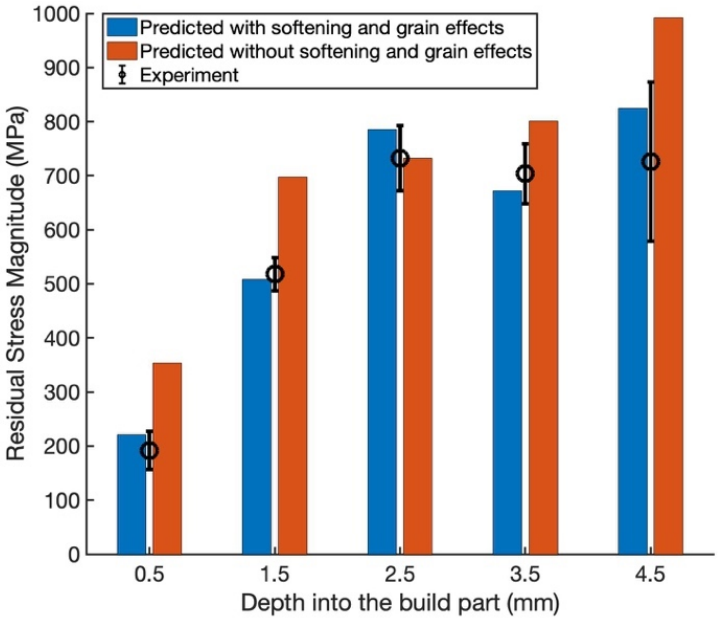

(b)

Figure 62. Comparison of the predicted residual stress considering the effects of flow softening and microstructure to the residual stress predicted without considering the effects of flow softening and microstructure during L-PBF of IN718 with laser power of 150 W and scan speed of 1000 mm/s (a) along the scan direction; (b) along the build direction.

CHAPTER 5. **CONCLUSION**

5.1 Summary

This dissertation presents a method of predicting the residual stress build-up generated as a result of additive manufacturing processes. In chapter 3, the step by step detailed explanation of analytical modeling of residual stress in metal additive manufacturing processes was presented. The modeling approaches covered including temperature field for various heat source models, thermal stress, residual stress, grain size, and also microstructure affected residual stress.

In chapter 4, the model predictions were compared to experimental measurements and finite element model results. Temperature field model was compared to experimental measurement of melt pool geometry and also FEM results. Various temperature model based on heat source geometry proposed including steady state moving point heat source, transient moving point heat source, transient semi-elliptical heat source, transient double elliptical heat source, and transient uniform heat source. The accuracy of each model is investigated under different process conditions. Moreover, the thermal stress model was compared to FEM results under different process condition. Furthermore, the experimental measurement procedures of residual stress conducted using X-ray diffraction were explained in detail for IN718 samples built via laser powder bed fusion and direct metal deposition, and Ti-6Al-4V built via direct metal deposition. The residual stress was predicted using incremental plasticity and kinematic hardening behavior of the metal

considering the effects of microstructure and flow softening of the materials. The predicted residual stresses under different process conditions for various material systems were compared to experimental measurements. Good qualitative and quantitative agreement were obtained between predicted and measured residuals stress.

5.2 Conclusions

The research presented in this dissertation was driven by the need for an analytical model for predictive modeling of additive manufacturing-induced residual stress. The research has shown that it is possible to model metal additive manufacturing induced residual stress in an analytical fashion. The impact of temperature field and thermal effects coupled with the knowledge of the material behavior under the influence of additive manufacturing process parameters were coupled to the incremental plasticity model to predict the residual stress. The modeling techniques presented are well suited for rapid and accurate analysis of metal additive manufacturing processes output including temperature field, thermal stress, and resulting residual stress. The temperature field was well predicted for various process conditions. Moreover, the thermal stress results were also comparable to finite element results of the same problem. Last, the residual stress predictions well captured the experimental measurements conducted via X-ray diffraction.

5.3 Contributions

The modeling techniques presented in this dissertation provide a means of both effectively understanding and analyzing the metal additive manufacturing processes. The intellectual contributions of the research presented are as follows;

- Developed analytical models to predict the temperature field for various heat source models.
- Validated the predicted temperature field using independent experimental work, and also by conducting FEM.
- Investigated the accuracy of each temperature model under different range of process parameters.
- Developed an analytical thermal stress model.
- Validated the thermal stress model by conducting FEM.
- Developed an analytical predictive residual stress model for metal additive manufacturing based on temperature field, thermal stress, microstructure, and flow behavior of the material.
- Developed an analytical grain size model.
- Developed an analytical residual stress model to incorporate the effect of microstructure.
- Performed residual stress experimental measurements via X-ray diffraction for various material systems including IN718, and Ti-6Al-4V.
- Performed residual stress measurements via X-ray diffraction for parts built via both powder bed and powder feed systems.
- Validated the residual stress model for both powder bed and powder feed systems.
- Performed sensitivity analysis of each model to characterize how model inputs affect the model results

5.4 Future Work

The current model provides a solid foundation for prediction of temperature field, thermal stress distribution, and also residual stress formed during metal additive manufacturing processes of powder bed and powder feed. It offers a rapid and effective method of modeling of the mechanical attributes of the additively manufactured part. However, there are opportunities to further improve the predictive capability of the model. The following areas for the future research will help to address limitations in the current modeling capabilities and improve the state of residual stress modeling.

Although model presented performs well in terms of capturing trends and magnitude of residual stress produced for various material systems, and a variety of processing condition, there are still areas of improvement.

- For the modeling used in this research, a semi-infinite medium is considered. As a result of this assumption, the model does not consider the effect of geometry which would then impact the residual stress generation.
- The effects of heat transfer boundary conditions were ignored which could impact the residual stress measurements.
- The effect of phase transformation is apparent in the metal additive manufacturing experimental data. The current modeling approach does not account for this effect in residual stress formation. A method to incorporate phase transformation and its impact on residual stress needs to be developed.
- The impact of porosity and density of additively manufactured part is not considered in this modeling approach. A model to incorporate the effect of porosity on residual stress is required.

- The effect of texture is not considered in this modeling. The texture evolution would affect the residual stress formation. A model to make a bridge between microstructural evolution and its impact on residual stress build-up is required.

With the above enhancements to the current modeling approach and general residual stress research, the techniques presented can progress towards becoming a more valuable tool for the prediction, control, and optimization of build process in metal additive manufacturing in order to achieve a desired part performance.

APPENDIX A. DESCRIPTION OF GREEN'S FUNCTIONS USED IN THERMAL STRESS MODELING

Elements of G matrix

Let the $X_m = x - x', Z_P = z + z', Z_m = z - z',$

The Green functions $G_{xh}(x, z, x', z')$ and $G_{xv}(x, z, x', z')$ are the normal stress due to a unit point body load acting at (x', z') along the *x* and *z* directions, respectively.

$$G_{xh} = \frac{1}{4\pi}\frac{1-2\nu'}{1-\nu'}\left[\frac{3-2\nu'}{1-2\nu'}\left(\frac{X_m}{X_m^2+Z_p^2}-\frac{X_m}{X_m^2+Z_m^2}\right)\right.$$

$$\left.+\frac{2}{1-2\nu'}\left(\frac{X_m Z_m^2}{(X_m^2+Z_m^2)^2}-\frac{X_m Z_p^2}{(X_m^2+Z_p^2)^2}\right)\right]$$

$$-\frac{1}{\pi}\frac{1}{1-\nu'}$$

$$\times\left((3-2\nu')\frac{X_m(z'Z_p+X_m^2)}{(X_m^2+Z_p^2)^2}\right.$$

$$\left.-\frac{3z'^2X_mZ_p^2+X_m{}^3(4z'^2+6zz'+z^2+X_m^2)}{(X_m^2+Z_p^2)^3}\right)$$

$$G_{zh} = -\frac{1}{4\pi}\frac{1-2\nu'}{1-\nu'}\left[\left(\frac{X_m}{X_m^2+Z_p^2}-\frac{X_m}{X_m^2+Z_m^2}\right)+\frac{2}{1-2\nu'}\left(\frac{X_m Z_m^2}{(X_m^2+Z_m^2)^2}-\frac{X_m Z_p^2}{(X_m^2+Z_p^2)^2}\right)\right]$$

$$-\frac{1}{\pi}\frac{y}{1-\nu'}$$

$$\times\left((3-2\nu')\frac{X_m Z_p}{(X_m^2+Z_p^2)^2}-\frac{X_m(4z'^3+9zz'^2+6z^2z'+z^3+zX_m^2}{(X_m^2+Z_p^2)^3}\right)$$

G_{xzh}

$$=\frac{1}{4\pi}\frac{1-2\nu'}{1-\nu'}\left[\left(\frac{Z_P}{X_m^2+Z_p^2}-\frac{Z_m}{X_m^2+Z_m^2}\right)+\frac{2}{1-2\nu'}\left(\frac{Z_p X_m^2}{(X_m^2+Z_p^2)^2}-\frac{Z_m X_m^2}{(X_m^2+Z_m^2)^2}\right)\right]$$

$$-\frac{1}{\pi}\frac{1}{1-\nu'}$$

$$\times\left((3-2\nu')\frac{z'Z_p^2+X_m^2(2z+z')}{2(X_m^2+Z_p^2)^2}\right.$$

$$\left.-\frac{z'^3\left(z'^2+3zz'+3z^2\right)+z^3z'^2+X_m^2\left(z'^3+6zz'^2+6z^2z'+z^3\right)+zX_m^4}{(X_m^2+Z_p^2)^3}\right)$$

$$G_{xv} = -\frac{1}{4\pi}\frac{1-2\nu'}{1-\nu'}\left[\left(\frac{Z_P}{X_m^2+Z_p^2}-\frac{Z_m}{X_m^2+Z_m^2}\right)+\frac{2}{1-2\nu'}\left(\frac{Z_m X_m^2}{(X_m^2+Z_m^2)^2}-\frac{Z_p X_m^2}{(X_m^2+Z_p^2)^2}\right)\right]$$

$$-\frac{1}{2\pi}\frac{1}{1-\nu'}$$

$$\times\left(2(1-\nu')\frac{Z_p}{(X_m^2+Z_p^2)}-\frac{[2(1-\nu')z-z']\left(Z_p^2-X_m^2\right)}{(X_m^2+Z_p^2)^2}\right.$$

$$\left.+\frac{2zz'Z_p\left(3X_m^2-Z_p^2\right)}{(X_m^2+Z_p^2)^3}\right)$$

$$G_{zv} = \frac{1}{4\pi}\frac{1}{1-\nu'}\left[(3-2\nu')\left(\frac{Z_P}{X_m^2+Z_p^2}-\frac{Z_m}{X_m^2+Z_m^2}\right)+2\left(\frac{Z_m X_m^2}{(X_m^2+Z_m^2)^2}-\frac{Z_p X_m^2}{(X_m^2+Z_p^2)^2}\right)\right]$$

$$-\frac{1}{2\pi}\frac{1}{1-\nu'}$$

$$\times\left(2(1-\nu')\frac{Z_p}{(X_m^2+Z_p^2)}+\frac{[2(1-\nu')z+z']\left(Z_p^2-X_m^2\right)}{(X_m^2+Z_p^2)^2}\right.$$

$$\left.-\frac{2zz'Z_p\left(3X_m^2-Z_p^2\right)}{(X_m^2+Z_p^2)^3}\right)$$

$$G_{xzv} = \frac{X_m}{4\pi}\frac{1-2\nu'}{1-\nu'}\left[\left(\frac{1}{X_m^2+Z_p^2}-\frac{1}{X_m^2+Z_m^2}\right)+\frac{2}{1-2\nu'}\left(\frac{Z_p^2}{(X_m^2+Z_P^2)^2}-\frac{Z_m^2}{(X_m^2+Z_m^2)^2}\right)\right]$$

$$-\frac{X_m}{2\pi}\frac{1}{1-\nu'}\times\left(4(1-\nu')\frac{zZ_p}{(X_m^2+Z_p^2)^2}+\frac{2zz'Z_p\left(3Z_p^2-X_m^2\right)}{(X_m^2+Z_p^2)^3}\right)$$

REFERENCES

1. Lewandowski, J.J. and M. Seifi, *Metal additive manufacturing: a review of mechanical properties.* Annual Review of Materials Research, 2016. **46**: p. 151-186.
2. King, W.E., et al., *Observation of keyhole-mode laser melting in laser powder-bed fusion additive manufacturing.* Journal of Materials Processing Technology, 2014. **214**(12): p. 2915-2925.
3. Denlinger, E.R., et al., *Effect of inter-layer dwell time on distortion and residual stress in additive manufacturing of titanium and nickel alloys.* Journal of Materials Processing Technology, 2015. **215**: p. 123-131.
4. Aggarangsi, P. and J.L. Beuth. *Localized preheating approaches for reducing residual stress in additive manufacturing*. in *Proc. SFF Symp., Austin*. 2006.
5. de La Batut, B., et al., *Analytical and Numerical Temperature Prediction in Direct Metal Deposition of Ti6Al4V.* Journal of Manufacturing and Materials Processing, 2017. **1**(1): p. 3.
6. Yap, C.Y., et al., *Selective laser melting of nickel powder.* Rapid Prototyping Journal, 2017. **23**(4): p. 750-757.
7. Galarraga, H., et al., *Effects of heat treatments on microstructure and properties of Ti-6Al-4V ELI alloy fabricated by electron beam melting (EBM).* Materials Science and Engineering: A, 2017. **685**: p. 417-428.
8. Kelly, S. and S. Kampe, *Microstructural evolution in laser-deposited multilayer Ti-6Al-4V builds: Part II. Thermal modeling.* Metallurgical and Materials Transactions A, 2004. **35**(6): p. 1869-1879.
9. Hoadley, A. and M. Rappaz, *A thermal model of laser cladding by powder injection.* Metallurgical Transactions B, 1992. **23**(5): p. 631-642.
10. Toyserkani, E., A. Khajepour, and S. Corbin, *3-D finite element modeling of laser cladding by powder injection: effects of laser pulse shaping on the process.* Optics and lasers in engineering, 2004. **41**(6): p. 849-867.
11. Cao, X. and B. Ayalew. *Control-oriented MIMO modeling of laser-aided powder deposition processes*. in *American Control Conference (ACC), 2015*. 2015. IEEE.
12. Hitzler, L., et al., *On the anisotropic mechanical properties of selective laser-melted stainless steel.* Materials, 2017. **10**(10): p. 1136.
13. Hitzler, L., et al., *A Review of Metal Fabricated with Laser-and Powder-Bed Based Additive Manufacturing Techniques: Process, Nomenclature, Materials, Achievable Properties, and its Utilization in the Medical Sector.* Advanced Engineering Materials, 2018. **20**(5): p. 1700658.
14. Rashid, R., et al., *Effect of scan strategy on density and metallurgical properties of 17-4PH parts printed by Selective Laser Melting (SLM).* Journal of Materials Processing Technology, 2017. **249**: p. 502-511.
15. Roberts, I.A., et al., *A three-dimensional finite element analysis of the temperature field during laser melting of metal powders in additive layer manufacturing.* International Journal of Machine Tools and Manufacture, 2009. **49**(12-13): p. 916-923.

16. Qi, H., J. Mazumder, and H. Ki, *Numerical simulation of heat transfer and fluid flow in coaxial laser cladding process for direct metal deposition.* Journal of applied physics, 2006. **100**(2): p. 024903.
17. Lee, Y. and D.F. Farson, *Simulation of transport phenomena and melt pool shape for multiple layer additive manufacturing.* Journal of Laser Applications, 2016. **28**(1): p. 012006.
18. Kumar, A. and S. Roy, *Effect of three-dimensional melt pool convection on process characteristics during laser cladding.* Computational Materials Science, 2009. **46**(2): p. 495-506.
19. Manvatkar, V., A. De, and T. DebRoy, *Spatial variation of melt pool geometry, peak temperature and solidification parameters during laser assisted additive manufacturing process.* Materials Science and Technology, 2015. **31**(8): p. 924-930.
20. Cheng, B. and K. Chou. *Melt pool geometry simulations for powder-based electron beam additive manufacturing*. in *24th Annual International Solid Freeform Fabrication Symposium-An Additive Manufacturing Conference, Austin, TX, USA*. 2013.
21. Pinkerton, A.J. and L. Li, *Modelling the geometry of a moving laser melt pool and deposition track via energy and mass balances.* Journal of Physics D: Applied Physics, 2004. **37**(14): p. 1885.
22. Mukherjee, T., W. Zhang, and T. DebRoy, *An improved prediction of residual stresses and distortion in additive manufacturing.* Computational Materials Science, 2017. **126**: p. 360-372.
23. Cheng, B., et al., *On process temperature in powder-bed electron beam additive manufacturing: model development and validation.* Journal of Manufacturing Science and Engineering, 2014. **136**(6): p. 061018.
24. Michaleris, P., *Modeling metal deposition in heat transfer analyses of additive manufacturing processes.* Finite Elements in Analysis and Design, 2014. **86**: p. 51-60.
25. Mirkoohi, E., et al., *Thermal modeling of temperature distribution in metal additive manufacturing considering effects of build layers, latent heat, and temperature-sensitivity of material properties.* Journal of Manufacturing and Materials Processing, 2018. **2**(3): p. 63.
26. Mirkoohi, E., et al., *Heat Source Modeling in Selective Laser Melting.* Materials, 2019. **12**(13): p. 2052.
27. Mirkoohi, E., et al., *Three-dimensional semi-elliptical modeling of melt pool geometry considering hatch spacing and time spacing in metal additive manufacturing.* Journal of Manufacturing Processes, 2019. **45**: p. 532-543.
28. Carcel, B., et al. *Improved laser metal deposition (lmd) of nickel base superalloys by pyrometry process control*. in *XVIII International Symposium On Gas Flow, Chemical Lasers, and High-power Lasers*. 2010. International Society for Optics and Photonics.
29. Cheng, B., et al., *Melt pool sensing and size analysis in laser powder-bed metal additive manufacturing.* Journal of Manufacturing Processes, 2018. **32**: p. 744-753.

30. Wang, L., et al., *An approach to predict the residual stress and distortion during the selective laser melting of AlSi10Mg parts.* The International Journal of Advanced Manufacturing Technology, 2018: p. 1-12.
31. Shiva, S., et al., *Laser annealing of laser additive–manufactured Ni-Ti structures: An experimental–numerical investigation.* Proceedings of the Institution of Mechanical Engineers, Part B: Journal of Engineering Manufacture, 2018. **232**(6): p. 1054-1067.
32. Mirkoohi, E., P. Bocchini, and S.Y. Liang, *An Analytical Modeling for Designing the Process Parameters for Temperature Specifications in Machining.* 2018.
33. Mirkoohi, E., P. Bocchini, and S.Y. Liang, *An analytical modeling for process parameter planning in the machining of Ti-6Al-4V for force specifications using an inverse analysis.* The International Journal of Advanced Manufacturing Technology, 2018: p. 1-9.
34. Yakout, M., M. Elbestawi, and S.C. Veldhuis, *On the characterization of stainless steel 316L parts produced by selective laser melting.* The International Journal of Advanced Manufacturing Technology, 2018. **95**(5-8): p. 1953-1974.
35. Mirkoohi, E., P. Bocchini, and S.Y. Liang, *Inverse analysis of residual stress in orthogonal cutting.* Journal of Manufacturing Processes, 2019. **38**: p. 462-471.
36. Ramirez-Cedillo, E., et al., *Process planning guidelines in selective laser melting for the manufacturing of stainless steel parts.* Procedia Manufacturing, 2018. **26**: p. 973-982.
37. Abdulateef, O.F., *Investigation of thermal stress distribution in laser spot welding process.* Al-Khwarizmi Engineering Journal, 2018. **5**(1): p. 33-41.
38. Shibib, K.S., M.A. Minshid, and N.E. Alattar, *Thermal and stress analysis in Nd: YAG laser rod with different double end pumping methods.* Thermal Science, 2011. **15**(suppl. 2): p. 399-407.
39. Yilbas, B.S., M. Sami, and S.Z. Shuja, *Laser-induced thermal stresses on steel surface.* optics and lasers in engineering, 1998. **30**(1): p. 25-37.
40. Ganeriwala, R., et al., *Evaluation of a thermomechanical model for prediction of residual stress during laser powder bed fusion of Ti-6Al-4V.* Additive Manufacturing, 2019. **27**: p. 489-502.
41. Noronha, P. and J. Wert, *An ultrasonic technique for the measurement of residual stress.* Journal of Testing and Evaluation, 1975. **3**(2): p. 147-152.
42. Chung, D., *Thermal analysis of carbon fiber polymer-matrix composites by electrical resistance measurement.* Thermochimica acta, 2000. **364**(1-2): p. 121-132.
43. Krause, T.W., et al., *Investigation of the stress-dependent magnetic easy axis in steel using magnetic Barkhausen noise.* Journal of Applied Physics, 1996. **79**(8): p. 4242-4252.
44. Ager III, J.W. and M.D. Drory, *Quantitative measurement of residual biaxial stress by Raman spectroscopy in diamond grown on a Ti alloy by chemical vapor deposition.* Physical Review B, 1993. **48**(4): p. 2601.
45. Prime, M.B., *Cross-sectional mapping of residual stresses by measuring the surface contour after a cut.* Journal of engineering materials and technology, 2001. **123**(2): p. 162-168.

46. Strantza, M., et al., *Coupled experimental and computational study of residual stresses in additively manufactured Ti-6Al-4V components.* Materials Letters, 2018. **231**: p. 221-224.
47. Wu, A.S., et al., *An experimental investigation into additive manufacturing-induced residual stresses in 316L stainless steel.* Metallurgical and Materials Transactions A, 2014. **45**(13): p. 6260-6270.
48. Staub, A., A.B. Spierings, and K. Wegener, *Correlation of meltpool characteristics and residual stresses at high laser intensity for metal lpbf process.* Advances in Materials and Processing Technologies, 2019. **5**(1): p. 153-161.
49. Wang, Z., et al., *Residual stress mapping in Inconel 625 fabricated through additive manufacturing: Method for neutron diffraction measurements to validate thermomechanical model predictions.* Materials & Design, 2017. **113**: p. 169-177.
50. Zhao, X., et al., *Numerical modeling of the thermal behavior and residual stress in the direct metal laser sintering process of titanium alloy products.* Additive Manufacturing, 2017. **14**: p. 126-136.
51. Hajializadeh, F. and A. Ince, *Finite element–based numerical modeling framework for additive manufacturing process.* Material Design & Processing Communications, 2019. **1**(1): p. e28.
52. Zekovic, S., R. Dwivedi, and R. Kovacevic. *Thermo-structural finite element analysis of direct laser metal deposited thin-walled structures*. in *Proceedings SFF Symposium,. Austin, TX*. 2005.
53. Panda, B.K. and S. Sahoo. *Numerical simulation of residual stress in laser based additive manufacturing process*. in *IOP Conference Series: Materials Science and Engineering*. 2018. IOP Publishing.
54. Chen, Q., et al., *An inherent strain based multiscale modeling framework for simulating part-scale residual deformation for direct metal laser sintering.* Additive Manufacturing, 2019. **28**: p. 406-418.
55. Ding, H. and Y.C. Shin, *A metallo-thermomechanically coupled analysis of orthogonal cutting of AISI 1045 steel.* Journal of Manufacturing Science and Engineering, 2012. **134**(5): p. 051014.
56. Ahmad, B., et al., *Residual stress evaluation in selective-laser-melting additively manufactured titanium (Ti-6Al-4V) and inconel 718 using the contour method and numerical simulation.* Additive Manufacturing, 2018. **22**: p. 571-582.
57. Li, C., et al., *Residual stress in metal additive manufacturing.* Procedia Cirp, 2018. **71**: p. 348-353.
58. Fergani, O., et al., *Analytical modelling of residual stress in additive manufacturing.* Fatigue & Fracture of Engineering Materials & Structures, 2017. **40**(6): p. 971-978.
59. Mirkoohi, E. and R. Malhotra. *Effect of particle shape on neck growth and shrinkage of nanoparticles*. in *ASME 2017 12th International Manufacturing Science and Engineering Conference collocated with the JSME/ASME 2017 6th International Conference on Materials and Processing*. 2017. American Society of Mechanical Engineers Digital Collection.
60. Mirkoohi, E., P. Bocchini, and S.Y. Liang, *An analytical modeling for process parameter planning in the machining of Ti-6Al-4V for force specifications using an*

inverse analysis. The International Journal of Advanced Manufacturing Technology, 2018. **98**(9-12): p. 2347-2355.
61. Mirkoohi, E., P. Bocchini, and S.Y. Liang, *Analytical temperature predictive modeling and non-linear optimization in machining.* The International Journal of Advanced Manufacturing Technology, 2019. **102**(5-8): p. 1557-1566.
62. Paul, R. and S. Anand, *Process energy analysis and optimization in selective laser sintering.* Journal of Manufacturing Systems, 2012. **31**(4): p. 429-437.
63. Carslaw, H. and J. Jaeger, *Conduction of heat in solids: Oxford Science Publications*. 1959: Oxford, England.
64. Carslaw, H.S. and J.C. Jaeger, *Conduction of heat in solids.* Oxford: Clarendon Press, 1959, 2nd ed., 1959.
65. Goldak, J., *A double ellipsoid finite element model for welding heat sources.* IIW Doc. No., 1985. **212**.
66. Nguyen, N., et al., *Analytical solutions for transient temperature of semi-infinite body subjected to 3-D moving heat sources.* WELDING JOURNAL-NEW YORK-, 1999. **78**: p. 265-s.
67. Lundbäck, A., H. Alberg, and P. Henrikson. *Simulation and validation of TIG-welding and post weld heat treatment of an Inconel 718 plate*. in *International Seminar on Numerical Analysis of Weldability: 29/09/2003-01/10/2003*. 2005. Techn. Univ. TYG.
68. Nguyen, N., et al., *Analytical Approximate Solution for Double Ellipsoidal Heat Source in Finite Thick Plate.* Welding Journal, 2004. **83**(3): p. 82.
69. Saif, M., C. Hui, and A. Zehnder, *Interface shear stresses induced by non-uniform heating of a film on a substrate.* Thin Solid Films, 1993. **224**(2): p. 159-167.
70. Cowper, G., *The shear coefficient in Timoshenko's beam theory.* Journal of applied mechanics, 1966. **33**(2): p. 335-340.
71. McDowell, D., *An approximate algorithm for elastic-plastic two-dimensional rolling/sliding contact.* Wear, 1997. **211**(2): p. 237-246.
72. Qi, Z., B. Li, and L. Xiong, *An improved algorithm for McDowell's analytical model of residual stress.* Frontiers of Mechanical Engineering, 2014. **9**(2): p. 150-155.
73. Khan, A.S. and S. Huang, *Continuum theory of plasticity*. 1995: John Wiley & Sons.
74. Group, A.M., J. Merwin, and K. Johnson, *An analysis of plastic deformation in rolling contact.* Proceedings of the Institution of Mechanical Engineers, 1963. **177**(1): p. 676-690.
75. Umemoto, M., H. Ohtsuka, and I. Tamura, *Grain size estimation from transformation kinetics.* Acta Metallurgica, 1986. **34**(7): p. 1377-1385.
76. Ji, X., et al., *Analytical modeling of post-printing grain size in metal additive manufacturing.* Optics and Lasers in Engineering, 2020. **124**: p. 105805.
77. Humphreys, F.J. and M. Hatherly, *Recrystallization and related annealing phenomena*. 2012: Elsevier.
78. Lesuer, D., *Experimental investigation of material models for Ti-6Al-4V and 2024-T3.* Avaliable online: https://e-reports-ext. llnl. gov/pdf/236167. pdf (accessed on 29 December 2015), 2000.

79. Kobayashi, T., et al., *Plastic flow behavior of Inconel 718 under dynamic shear loads.* International Journal of Impact Engineering, 2008. **35**(5): p. 389-396.
80. Pouzet, S.b., *Fabrication additive de composites à matrice titane par fusion laser de poudre projetée*. 2015, Paris, ENSAM.
81. Peyre, P., et al., *Analytical and numerical modelling of the direct metal deposition laser process.* Journal of Physics D: Applied Physics, 2008. **41**(2): p. 025403.
82. Fu, C. and Y. Guo, *Three-dimensional temperature gradient mechanism in selective laser melting of Ti-6Al-4V.* Journal of Manufacturing Science and Engineering, 2014. **136**(6): p. 061004.
83. 李俐群, et al., *Ti6Al4V 激光熔化沉积熔池温度场与微观组织特性.* 中国激光, 2017. **44**(3): p. 113-120.
84. Soylemez, E., *MODELING THE MELT POOL OF THE LASER SINTERED TI6AL4V LAYERS WITH GOLDAK'S DOUBLE-ELLIPSOIDAL HEAT SOURCE.*
85. Yu-Lung Lo, B.-Y.L., Hong-Chuong Tran *Optimized Hatch Space Selection in Double-Scanning Track Selective Laser Melting Process* The International Journal of Advanced Manufacturing Technology, 2019.
86. Hong-Chuong Tran, Y.-L.L., *Systematic Approach for Determining Optimal Processing Paramters to Produce Parts with High Density in Selective Laser Melting Process* The International Journal of Advanced Manufacturing Technology, 2019.
87. Tran, H.-C. and Y.-L. Lo, *Heat transfer simulations of selective laser melting process based on volumetric heat source with powder size consideration.* Journal of Materials Processing Technology, 2018. **255**: p. 411-425.
88. Tran, H.-C., Y.-L. Lo, and M.-H. Huang, *Analysis of Scattering and Absorption Characteristics of Metal Powder Layer for Selective Laser Sintering.* IEEE/ASME Transactions on Mechatronics, 2017. **22**(4): p. 1807-1817.
89. Nadammal, N., et al., *Influence of support configurations on the characteristics of selective laser-melted inconel 718.* JOM, 2018. **70**(3): p. 343-348.
90. Prevey, P.S., *X-ray diffraction residual stress techniques.* ASM International, ASM Handbook., 1986. **10**: p. 380-392.
91. Yang, Y., et al., *Prediction of microstructure, residual stress, and deformation in laser powder bed fusion process.* Computational Mechanics, 2018: p. 1-17.
92. Bartlett, J.L. and X. Li, *An overview of residual stresses in metal powder bed fusion.* Additive Manufacturing, 2019.
93. Lee, Y. and W. Zhang, *Modeling of heat transfer, fluid flow and solidification microstructure of nickel-base superalloy fabricated by laser powder bed fusion.* Additive Manufacturing, 2016. **12**: p. 178-188.
94. Li, S., et al., *Melt-pool motion, temperature variation and dendritic morphology of Inconel 718 during pulsed-and continuous-wave laser additive manufacturing: A comparative study.* Materials & Design, 2017. **119**: p. 351-360.
95. Nyon, K., et al., *Finite element analysis of laser inert gas cutting on Inconel 718.* The International Journal of Advanced Manufacturing Technology, 2012. **60**(9-12): p. 995-1007.
96. Liu, L., A. Hirose, and K.F. Kobayashi, *A numerical approach for predicting laser surface annealing process of Inconel 718.* Acta materialia, 2002. **50**(6): p. 1331-1347.

97. Selvan, J.S., et al., *Laser boronising of Ti–6Al–4V as a result of laser alloying with pre-placed BN.* Materials Science and Engineering: A, 1999. **260**(1-2): p. 178-187.
98. Nayan, N., et al., *Microstructure and micro-texture evolution during large strain deformation of Inconel alloy IN718.* Materials Characterization, 2015. **110**: p. 236-241.
99. Tancret, F., et al., *Design of a creep resistant nickel base superalloy for power plant applications: Part 3-Experimental results.* Materials Science and Technology, 2003. **19**(3): p. 296-302.
100. Ozel, T., et al., *3D finite element modelling of chip formation process for machining Inconel 718: comparison of FE software predictions.* Machining Science and Technology, 2011. **15**(1): p. 21-46.